LONG-RANGE ACOUSTIC PROPAGATION THROUGH INTERNAL WAVE FIELDS

Mark L. Grabb

COMMUNICATIONS & SIGNAL PROCESSING LABORATORY
Department of Electrical Engineering and Computer Science
The University of Michigan
Ann Arbor, Michigan 48109

April 1996

ACKNOWLEDGEMENTS

I am grateful to my wife Colleen for all the sacrifices she has made during my return to graduate school. She has put everything aside in her life for me and our son, Clark. Her perpetual positive attitude has made life more enjoyable than I ever thought possible. My mother and father have given me many things, but most importantly they gave me a fantastic childhood and never-ending encouragement and support. Thanks! I have one brother. We grew up together. I think more of him than he will ever know. To adequately state the love and admiration I have for my family would take more pages than this dissertation, so let me simply say, "I think they are the best."

The first day I met Professor Birdsall, I wanted to work for him. I was aware of many of his accomplishments, but I was not yet aware that this academic giant is packaged in a humble, unselfish, sincere, and humorous friend. Ted's door is always open. I often caught him working late into the evening on his own work, after spending the entire business day solving the problems of others (certainly including my problems too). The years that I have spent working with Ted have enriched my life in so many areas. I find my engineering approach to problems becoming similar to his, and this is the highest technical compliment I can pay myself.

Gary Bold is primarily responsible for getting me rolling in the field of computational acoustics. It was great to have him here from New Zealand as I began my research. Even better is Gary's love for life and his enthusiasm. He makes math and physics come to life. Murray Johns is another New Zealander I had the privilege of working with. He urged us to appreciate normal acoustic modes, and lived life with a smile on his face.

Kurt Metzger, thanks for everything! I <u>will</u> "pass it on."

I worked for over a year with Shuo Wang. I enjoyed it and learned a lot. I hope our paths cross again. Shuo, thanks for recommending a 3D model, and pounding through a lot of detail with me.

Jim Daws, mornings will never be the same once I leave Michigan. I have enjoyed our morning conversations to kick off the day.

James Poplawski: Good Luck with the DD Display. I bet it works with real data! Thanks for all your insights during our US meetings.

Carol Van Aken and Dawn Wacker were always helpful and cheerful. Their conversations made some long days fun. Thanks.

I want to thank a group of engineers and scientists that I had extended technical email conversations with: Paul Book (Duke University), John Colosi (Scripps Oceanographic Institute), Stan Flatté (University of California at Santa Barbara), Matt Dzieciuch (Scripps Oceanographic Institute), and Paul Casey (University of Auckland).

I would like to thank my dissertation committee for all of their time and technical contribution. The blood of 100 semicolons is on your hands.

TABLE OF CONTENTS

LIST OF TABLES

LIST OF FIGURES

LIST OF APPENDICES

GLOSSARY

acoustic path cycle length: range of one cycle of a ray path. this cycle perfectly repeats for range-invariant ocean models. typical ranges are 30 to 70 km.

axial source: source located on the sound channel axis (depth of minimum sound speed)

buoyancy frequency: the density gradient is described in terms of the buoyancy frequency, $N(z)$, the frequency at which an isodensity displaced from its equilibrium position will oscillate.

caustic: the point where a modeled infinite-frequency acoustic signal has infinite amplitude. the wavefront is folding onto itself at this point.

caustic phase: each time an acoustic ray travels through a caustic, the acoustic phase advances 90°. the summation of these 90° phase rotations is the caustic phase and is a contribution to the acoustic time-domain phase.

coherent integration loss: the loss incurred by coherently integrating a signal with unstable time-domain phase referenced to coherently integrating a signal with perfectly stable time-domain phase.

computational ocean model: the sound speed field that is directly used in the computer code to numerically simulate acoustic propagation.

crescendo: the terminal time segment of a deep ocean acoustic reception. these receptions typically increase in amplitude with time, ending with a sharp large amplitude segment.

differential equation method: a method for computing the amplitude of an acoustic ray based on solving additional differential equations along the ray path.

diffracted wavefronts: finite-frequency acoustic wavefronts spawned from diffraction.

dispersion: in the context of acoustic normal modes, when modes of different frequency travel at different horizontal speeds.

eigenrays: acoustic rays that connect the source and receiver.

focusing/defocusing: geometric gathering/spreading of acoustic rays which related to increased/decreased acoustic amplitude along the propagating wavefront.

Garret-Munk spectrum: community accepted analytic spectral description of deep ocean internal wave fields.

group velocity: in the context of acoustic normal modes, the "average" velocity of a spectral band of normal modes with identical mode number.

high-frequency approximation: approximation required to solve the wave equation in terms of acoustic rays

horizontal line array: an array of receiving hydrophones oriented horizontally.

hypo front: a hypothesized measurement front.

inertial frequency: is a function of the latitude and is introduced by including the Coriolis acceleration into the equations of motion.

internal waves: slowly moving density waves and are similar to the familiar ocean surface waves, except they occur internal to the ocean.

launch angle: the ray inclination α_o and ray azimuth ψ_o angles at the source. ray inclination angles are positive downward, consistent with the z-axis being positive downward.

long-range propagation: 150 km to 10 Mm and beyond.

low-angle approximation: approximation required to reduce the wave equation to the parabolic equation.

mainfront: the primary wavefront among many micromultipath wavefronts termed microfronts.

measurement front: impulse response defining the number of arrivals and traveltimes to any collection of reception points, typically restricted to a fixed range.

megameter: 1000 km.

mesoscale eddy: ocean eddies with diameters on the scale of 100 km.

micromultipath: multipath (multiple arrivals) typically within the acoustic pulse reciprocal bandwidth which have resulted from the breaking and bending of a single wavefront.

microfront: the many secondary fronts along with the primary front termed the mainfront.

micromultipath combing loss: the loss resulting from the destructive combining of micromultipath relative to all the micromultipaths being precisely in phase.

Munk profile: popular academic sound-speed profile for mid-latitude deep-ocean regions.

nominal acoustic direction: directly from transmitter to receiver.

nonensonified region: area where infinite-frequency acoustic analysis would not predict acoustic propagation (also called shadow zone).

normal modes: the horizontally propagating acoustic modes of the deep ocean waveguide.

ocean process: any physical process which perturb the sound speed field, that is moves the ocean waters. for example internal waves, tides, eddies.

operational bandwidth: the complete spectral coverage of a signal

parabolic equation: approximation to the wave equation (obtained by employing the low-angle approximation) that has a solution-form that is suitable for computer implementation.

path-integral technique: a method developed in the early 1970's to stochastically model acoustic propagation through a fluctuating ocean.

phone impulse response: the impulse response of set source-receiver geometry.

physical ocean model: a description of the sound speed field, modeling the ocean processes under study, that has not been compromised with issues of implementation, a pure physical description.

propagation method: numerical simulation of acoustic propagation given the computational ocean model. methods are based on solutions to the wave equation.

ray centered coordinate system: coordinate system centered at the current point on the ray path, since the ray path is locally normal to the wavefront these two axes create a convenient coordinate system.

ray endpoint density method: method to calculate the received acoustic amplitude based on the density of rays. many rays are propagated.

ray tracing: solution to the wave equation (obtained by making the high-frequency approximation) suitable for computer implementation.

ray tube: for illustrative purposes, acoustic rays are given dimension to model geometric spreading of the acoustic power.

Rayleigh fading: constructive and destructive interference of multiple arrivals within the pulses reciprocal bandwidth, under certain classical conditions will cause the received amplitude to fade with Rayleigh statistics and uniformly distributed phase.

reciprocity: as long as the motion of the water can be ignored (currents), the received signal from some source is identical to a received signal at the "source" transmitted from the receiver.

resolution: the relative delay of two like pulses required to observe two distinct pulses in a typical signal-to-noise ratio environment. likewise, the time-width of the main lobe of the pulse measured at half-height.

shadow zone: area where infinite-frequency acoustic analysis would not predict acoustic propagation (also called nonensonified region).

sheet: single section of a timefront of measurement front.

sound channel axis: depth of minimum sound speed. if the source and receiver are located on the sound channel axis, the terminal arrival is composed of sound that traveled in a straight line from transmitter to receiver.

sound speed profile: speed of sound as a function of depth.

spatially synchronized internal waves: internal waves having spatial wavelengths in the direction of acoustic propagation which are an integer fraction of the acoustic ray path cycle length. internal waves are spatially synchronized with respect to a given acoustic ray (acoustic arrival).

thermocline: the top 500 to 1000 meters in the ocean. this is where temperature changes dominate the shape of the sound speed profile. sometime the top 100 meters is referred to as the mixing layer and not considered part of the thermocline.

timefront: location of an acoustic impulse transmitted from the source after a set time.

transverse focusing: focusing of the acoustic rays along the transverse coordinate resulting from spatially synchronized internal waves.

vertical focusing: focusing of the acoustic rays along the vertical (depth) coordinate resulting from spatially synchronized internal waves.

vertical line array: an array of receiving hydrophones oriented vertically (depth).

wave equation: mathematical model (partial differential equation) of small amplitude wave propagation based on the equations of motion, continuity, an state.

LIST OF SYMBOLS

A	ray tracing auxiliary parameter
ΔA	cross sectional area of ray tube
B	ray tracing auxiliary parameter
b	Munk profile parameter
$c(z)$	sound speed profile
c_o	minimum sound speed
c_s	sound speed at source depth
δc	internal wave induced change in sound speed
D	ray tracing auxiliary parameter
f_c	acoustic center frequency
f	baseband frequency
F	Fourier transform operator
G	internal wave strength (complex: magnitude and phase)
h	ocean impulse response
I	intensity
i	$\sqrt{-1}$
j	internal wave mode number
k	internal wave wavenumber
k_x	internal wave wavenumber projected along range coordinate
k_y	internal wave wavenumber projected along transverse coordinate
L_{ray}	acoustic ray path cycle length
M	number of internal wave modes
m	internal wave mode index
$N(z)$	buoyancy frequency
N_o	extrapolated surface buoyancy frequency
$P(f)$	acoustic power spectrum
p	acoustic field
q	height of ray tube

Q	acoustic cycles per pulse
r	ray coordinate (ray coordinate system)
R	range - distance between transmitter and receiver
s	dynamic ray tracing auxiliary parameter
S	acoustic spectrum
$\tilde{S}$	baseband acoustic spectrum
t	time
T	ocean temperature
ΔT	change in average ocean temperature
u	dynamic ray tracing auxiliary parameter
U	normal acoustic mode function
v	width of ray tube
w	wavefront coordinate (ray coordinate system)
W	acoustic spectral resolution bandwidth
$W_j(k,z)$	internal wave mode function
x	range coordinate
y	transverse coordinate
z	depth coordinate
z_o	depth of minimum sound speed
z_b	ocean bottom depth
z_s	source depth
α	ray inclination angle (along ray path)
α_o	ray launch angle inclination
$\Delta\phi$	change in time-domain phase
ϵ	Munk profile parameter
η	Munk profile parameter
κ	normal mode wavenumber
Λ_x	internal wave wavelength projected along range coordinate
Λ_y	internal wave wavelength projected along transverse coordinate
ω	internal wave angular frequency

ω_i	global inertial angular frequency
Ω	acoustic angular frequency
ψ_o	ray launch angle azimuth
ψ	ray azimuth azimuth (along ray path)
$\wp$	power
$\Delta\tau$	change in traveltime
θ	internal wave propagation angle
Υ	envelope of normal mode function
ς	number of caustics crossed by a ray
ζ_m	displacement field of mth internal wave mode
ζ	internal wave displacement field

Preface

This was written to set the stage for the research in this dissertation.

"Acoustic monitoring of ocean processes" is how the U.S.Congress labeled research work that combines the science of oceanography and the engineering research and technology of underwater sound transmissions. The use of sound waves opened up the field of ocean acoustic *tomography* to study ocean mesoscale eddies of perhaps 100 km diameter, and acoustic *thermometry* to study warming and cooling on ocean basin scales of several megameters. (The meter was originally fixed so that the distance from pole to equator would be ten megameters, 10 Mm.)

This all is possible because sound travels faster in warmer water (near the surface) and in denser water (near the bottom). These balance, forming a minimum sound speed at roughly a kilometer depth. In the 3-5 km deep ocean the sound will *refract* toward this minimum, oscillating shallow and deep and avoiding scattering by the surface and bottom. The acoustic frequencies have to be quite low, 25-250 hertz, to escape catastrophic losses due to disassociation of various dissolved salts. In this way low frequencies and refraction combine to allow propagation for many megameters, with the sound weakening only due to spreading out thinner and thinner. Precisely timed point to point transmissions provide the sophisticated oceanographer with an average temperature meter.

After traveling for long distances the weak received signals must be very time stable in order for repeated signal processing to build them up out of the shipping noise; amplitude stability is not really necessary. Although long continuous measurements are few, they do indicate that the ocean propagation is indeed time-stable but amplitude-unstable. No current propagation theory or model matches this behavior, so new ideas must be incorporated in propagation models to match the measurements.

Internal waves, waves of density anomalies and associated temperatures, appear to be everywhere in all oceans. Direct measurements of internal waves are difficult, and there are very few. Development of internal wave understanding as a stochastic theory have spanned

the last twenty years. Recent research has progressed from classical mathematical analysis to computer simulations, with statistics derived from averages of many *random* realizations.

Internal waves are universally believed to be the ultimate limitation on acoustic propagation stability. We must understand the interaction of sound and internal waves if we depend on time-stability in long range propagation.

This dissertation will investigate internal waves as the cause of time-stable but unstable-amplitude propagation. In order to do this yet another obstacle had to be overcome, this being in matching computational modeling to physical modeling. When the refraction of the ocean is the result of temperature and density changes as a function of depth as mentioned above, the three-dimensional physics can be simplified to two dimensions since the sound that gets from the transmitter to the receiver will travel in the vertical plane between them. The computer programs that calculate propagation take advantage of this simplification.

When internal waves move across the acoustic path they will refract the sound out of the plane, so the computations must be 3-D to match the 3-D physics. Going back to 3-D from 2-D for the differential equation *ray tracing* approach to calculation is straightforward; but all other computational methods will need major overhauls because they relied heavily on the 2-D simplification. Historically the acoustic interaction part of internal wave simulations has used 2-D propagation models.

This dissertation research is exploratory in nature, taking advantage of ever increasing computer power and memory to investigate the interaction of internal waves and acoustic propagation. The methodology is to examine in detail specific instances of internal wave fields in a specific 750 km propagation scenario. A phenomena to be labeled "spatial synchronization" was discovered early, and became the cornerstone for understanding both 2-D and 3-D interactions that caused time-stable but amplitude-unstable realizations. The methodology and resulting understanding are deterministic, not stochastic.

CHAPTER 1

Introduction

1.1 Background

The speed of sound in ocean waters depends on temperature, pressure, and to a lesser extent salinity. An increase in temperature of $1°C$ increases the speed of sound by 4.6 meters per second[1]. By transmitting an acoustic pulse over a fixed range, changes in acoustic traveltime can be related to changes in average ocean temperature over the propagation path. In other words, one can construct an acoustic thermometer which estimates changes in ocean temperature.

This is the key concept to an international project[1] aimed at detecting global changes in average ocean temperature. It is desirable to separate the transmitter and receiver by great distances to obtain a global average temperature. Local measurements contain temperature variations due to ocean circulation processes such as mesoscale eddies (ocean eddies with diameters on the scale of 100 km). To monitor small changes in average temperature, acoustic propagation over long ranges can be an asset. For a change in average ocean temperature of ΔT in $°C$, the change in acoustic traveltime in seconds is approximated by the relation

$$\Delta \tau \approx -2R\Delta T \tag{1.1}$$

where R is the transmitter-receiver separation in Mm (megameters). Longer ranges allows a measured traveltime change to relate to a more sensitive change in average ocean temperature. The accuracy in determining a change in acoustic traveltime will depend on the

---

[1] The Acoustic Thermometry of Ocean Climates Project

1

signal-to-noise ratio of a resolved[2] received pulse. The received signal energy will decrease with longer range propagation causing experiment designers to face a trade off in selecting transmitter and receiver locations. The acoustic signal must be composed of low frequencies to propagate through the deep ocean thousands of kilometers without suffering catastrophic attenuation. At frequencies of the order of 75 hz the attenuation of sound in the ocean is of the order of 0.001 dB/km. This attenuation factor increases exponentially with the square of acoustic frequency making long range propagation of acoustic frequencies over several hundred hertz impractical.

The sound takes multiple paths to the receiver, creating many wavefront arrivals, known as multipath. By transmitting a broadband waveform, many of the early wavefront arrivals can be resolved. By tracking the received time-domain phase of an early arrival, precise changes in the transmitter-to-receiver acoustic traveltime can be estimated, creating a very accurate acoustic thermometer. To obtain sufficient signal energy and pulse resolution at the receiver, the propagating waveform is a continuously periodic large time-bandwidth product signal with a time period precisely equivalent to an integer number of center frequency cycles, so that consecutive periods can be directly coherently summed and making continuous transmissions implementable for some signaling types. Candidate signal types are phase modulated waveforms based on maximal period linear binary pseudo-random sequences (known as m-sequences) [2] and swept frequency modulated waveforms [3]. "Continuously periodic" refers to many identical periods being transmitted consecutively. Period-to-period time-domain phase changes of an early (resolved) wavefront arrival correspond to precise measurements of traveltime change integrated along the particular propagation path. Each wavefront arrival has traveled a unique path and corresponds to a unique interrogation of the ocean. It is also desirable to transmit a source waveform with an appropriate spectral shape such that the time-domain pulse sidelobes are low with respect to the pulse peak. In summary, it is desirable to employ a low frequency (reduce attenuation), large time-bandwidth product (increase energy and improve resolution) source waveform for long range acoustic propagation experiments.

---

[2]The reference is to resolution in the time domain. Two pulses separated in time such that it can be distinguished that two pulses are present is a qualitative description of resolution.
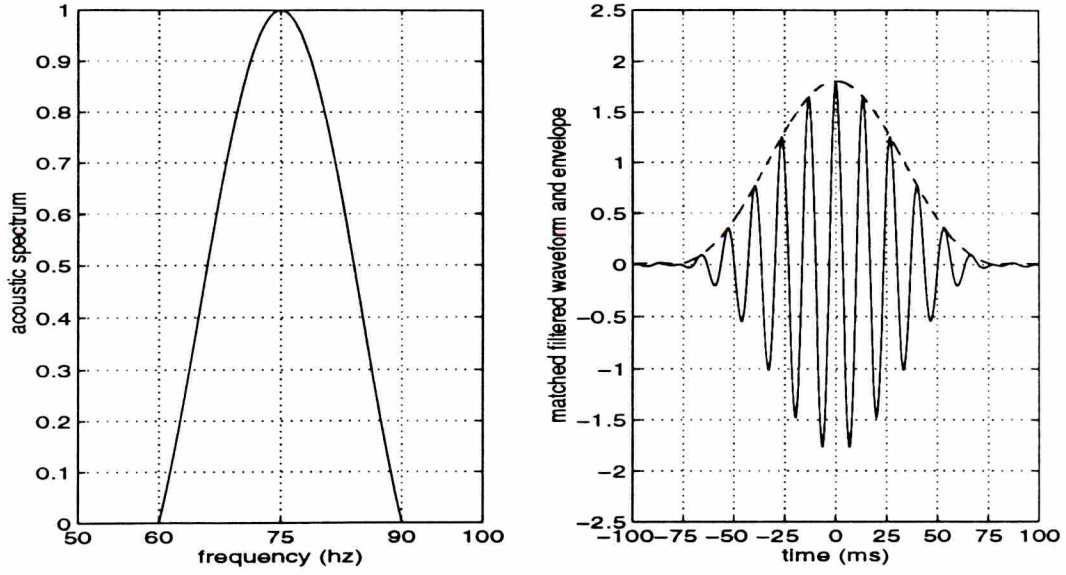
Figure 1.1: The source voltage spectrum is shown to the left. Only the active positive frequencies are displayed. The voltage spectrum is centered at 75 hz, has a bandwidth of 15 hz, and null-to-null covers 30 hz from 60 hz to 90 hz. The time-domain envelope (dashed) and waveform (solid) of the received and matched filtered pulse is shown to the right. The effective transmitted acoustic pulse consists of 5 cycles of a 75 hz waveform. This is referred to as a Q of 5. The "Q" is equal to the center-frequency divided by the bandwidth, in this case $75/15 = 5$.

Figure 1.1 shows the voltage spectrum of a desirable low-frequency, broadband source signal and the matched filtered time-domain waveform. The center frequency, f_c, is 75 hz and the bandwidth is $W = 15$ hz. The null-to-null operational bandwidth is 30 hz (from 60 to 90 hz). The voltage spectrum, $S(f)$, is sinc-shaped and defined by

$$S(f) = \begin{cases} \frac{1}{2}\mathrm{sinc}(f - \frac{f_c}{W}) & f_c - W < f < f_c + W \\ \frac{1}{2}\mathrm{sinc}(f + \frac{f_c}{W}) & -f_c - W < f < -f_c + W \\ 0 & \text{otherwise} \end{cases} \quad (1.2)$$

where f is the acoustic frequency. The corresponding baseband spectrum is

$$\tilde{S}(f) = \begin{cases} \mathrm{sinc}(f/W) & -W < f < W \\ 0 & \text{otherwise} \end{cases} \quad (1.3)$$

If the spectrum were not truncated, the effective time-domain pulse would consist of exactly Q f_c-cycles. In this case, $Q = 5$ and $f_c = 75$ hz cycles. In general, $Q = f_c/W$ so that the

3

spectrum described in Equation 1.2 has a Q equal to 5 as well. The resolution of the pulse is approximately $1/W$. The truncation of the spectrum yields a resulting matched filtered time-domain pulse with a smoothed rounded shape and a resolution of 72 ms. The time-domain envelope is shown using a dashed curve. The time-domain sidelobes are below a level of 0.1 giving a 19 dB peak-to-sidelobe level for this matched filtered signal. For multipath receptions, the signal sidelobes can be a cause of self interference.

Figure 1.2 shows the envelope and phase of two consecutively received and processed transmissions created from a computer simulation of 1 Mm range acoustic propagation through the deep ocean. No noise was included in the simulation, and the low frequency broadband source waveform described by Equation 1.1 was used. The early resolved wavefront arrivals are apparent by the single pulses early in the reception. The two arrivals vary in envelope, but only slightly vary in time-domain phase. These changes are the result of the time-varying ocean model. A change in time-domain phase of $\Delta\phi$ (cycles) corresponds to a traveltime change (in seconds), $\Delta\tau$, of

$$\Delta\tau = \Delta\phi/f_c, \tag{1.4}$$

where f_c is the acoustic waveform center frequency. A positive value of $\Delta\tau$ indicates the second transmission experienced an increase in traveltime. For the first arrival near 167.2 seconds, $\Delta\phi = 0.1$ cycles which corresponds to a change in traveltime of $1.\bar{3}$ ms and a change in average ocean temperature of $0.000\bar{6}\,C°$ along this particular propagation path. This is an over simplification of the processing and analysis required to determine changes in ocean temperature, but the main point of the procedure is accurately illustrated.

The average power of an early arrival is low. Shipping noise interferes with the reception throughout the signal band. Long integration times are required to obtain sufficient signal energy with respect to noise and interference levels to reliably estimate the received phase. This is accomplished by transmitting long periods or coherently summing consecutive periods. If the time-domain phase is not stable, beneficial coherent integration times are short, sufficient signal energy can not be accumulated, and time-domain phase measurements can not be used for precise traveltime measurements. Phase instabilities can be the result of transmitter/receiver motion or induced by physical ocean processes which contribute dy-
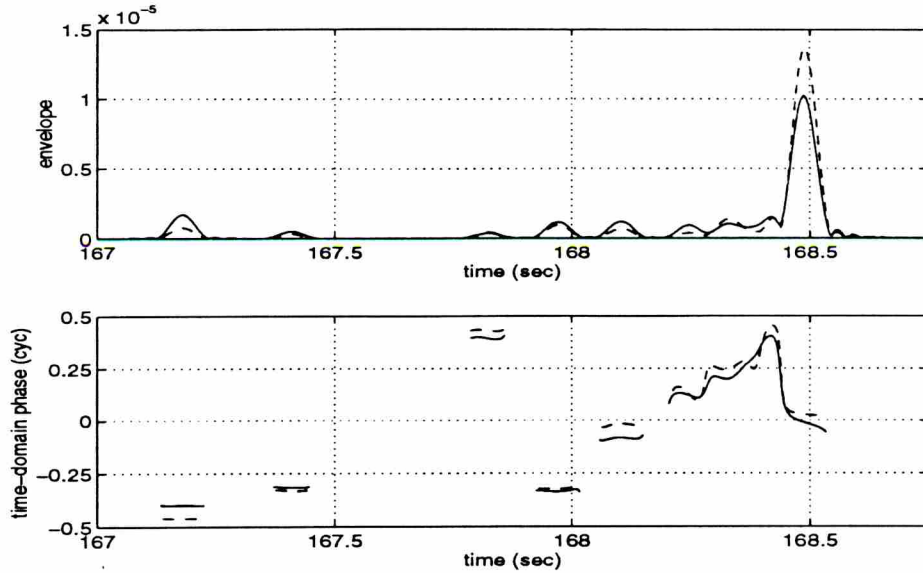
Figure 1.2: The time-domain envelope (top) and phase (bottom) receptions from two long range transmissions (solid and dashed lines). Changes in the time-domain phase between the receptions can be used to compute the average change in traveltime along the propagation path. Each arrival corresponds to a unique propagation path through the ocean.

namically to the ocean sound speed field. Motions of the transmitter and receiver can be eliminated either through rigid moorings or tracking their movement and removing the effective movement from the received data via signal processing techniques. It is of critical importance to determine if ocean processes can cause significant phase fluctuations during expected coherent integration times of 20 minutes to a few hours.

From long-range acoustic propagation experimental results, the amplitude of individual early arrivals is reported to fluctuate[4]. Histograms of amplitude values taken over long time periods show a shape that is consistent with Rayleigh fading. An intuitive description of Rayleigh fading is that a single arrival is composed of many "micromultipath" arrivals, each taking a slightly different route from transmitter to receiver, and the Rayleigh amplitude is the result of constructive and destructive interference of the multiple arrivals via the dynamic relative traveltimes. In this case, the time-domain phase will be unstable. Experimental results with a rigidly moored transmitter and receiving array show that the period-to-period time-domain phase remains relatively stable over durations of significant

5

amplitude fluctuation. This observation is not consistent with the traditional Rayleigh fading model.

It has been conjectured by Birdsall that it must be internal waves which modulate the acoustic amplitude without significantly affecting the r   ived time-domain phase. Internal waves are the physical ocean process believed to have the most significant impact on the received acoustic waveform for time scales under 12 hours, and therefore become the immediate candidate causing the Rayleigh-like amplitude fading / stable time-domain phase phenomenon. The internal wave field is composed of a series of horizontally propagating modes. Internal waves are viewed by most researchers as a stochastic disturbance to the ocean sound-speed field and are believed to significantly contribute to an ultimate uncertainty in the time-domain amplitude and phase of the received acoustic waveform. Considerable work has been expended for over thirty years to assess the impact that internal waves have on long range acoustic propagation.

1.2 Stochastic versus deterministic modeling

To investigate acoustic propagation through deep ocean internal wave fields, it is necessary to establish a model defining the impact of internal waves on the propagating acoustic waveform. Deep ocean internal wave fields over long range propagation paths are a three-dimensional, time-varying, complex, large-scale system. Researchers have primarily modeled the internal wave field as a random field[5]-[12] . A deterministic model could entail accounting for each internal wave that has a significant impact on acoustic propagation. If manageable, the deterministic approach would yield detailed information on the internal wave field. This information is of interest to oceanographers, climatologists, and naval forces. Also internal-wave induced variations on the received waveform once determined could be removed to help understand other ocean processes that modulate the received signal.

1.2.1 Stochastic modeling

Since the mid 1970s there have been continual advances in the understanding of deep-ocean internal-wave fields and acoustic propagation through them[5]-[12]. Much of the early

6

success was based on a path-integral technique[5]. This technique exploits the geometrical optics approximation for propagation in the absence of internal waves and integrates the internal-wave effects along this path to estimate statistics on received acoustic observables. Several experiments in the 1970's provided theoreticians measured data on acoustic fluctuation with which to compare their predictions[5]. The observations of these experiments were the received acoustic phase and intensity spectra. The measured spectra agreed with theoretical predictions from the path-integral theory, giving support to their conjecture that internal waves significantly impact long-range, deep-ocean acoustic propagation[7].

Users of the path-integral technique understand the limits of its applicability. Recent long-range, low frequency ocean acoustic propagation experiments have gathered precise data that cannot be quantitatively characterized using path-integral techniques[11]. For this reason, numerical simulations have been developed. A realization of a random field is constructed to represent the ocean sound speed field. A propagation method is used to simulate acoustic propagation through the field to a down range hydrophone. The field is advanced discretely in time, each time simulating the received waveform. Time averages are taken to estimate first and second order statistics of the received phase and intensity of the wavefront arrivals.

An example of numerical simulation statistical estimates matching measured acoustic reception statistics from a long-range propagation experiment is described in [12]. In this work a 2D (range and depth) ocean sound-speed model was constructed, representing the deep-ocean waveguide (deterministically) and the internal-wave field (stochastically) present during the experiment. The internal-wave field model was composed of hundreds of internal waves and was in agreement with the Garrett-Munk spectrum[3][6]. The parabolic equation (PE) propagation method was used to simulate acoustic propagation. The experimental measurements showed unexpected acoustic fluctuations (significant variance in received phase). The simulation results also showed these fluctuations, yielding strong evidence they can be attributed to the internal-wave field. In summary, previous and continuing successful work in internal-wave ocean modeling is based on characterizing the statistical properties

---

[3]The Garret-Munk spectrum is the current stochastic description of deep ocean internal waves. It was developed in the early 1970's and is based on limited experimental data.

of the received acoustic signal based on a random-field interpretation of the internal-wave sound speed perturbations and is carried out using a 2D ocean model. It is important to note that long time averages (over days) are taken to compute variance estimates.

1.2.2 Deterministic modeling

The research reported in this dissertation uses a different approach. Numerical simulation is used to study acoustic propagation through internal-wave fields. The approach uses 3D modeling and deterministically models both the deep-ocean waveguide and the internal-wave field. Physically, the internal-wave field is composed of a summation of internal wave modes. The goal is to understand how specific internal waves impact the received acoustic signal, as opposed to understanding how a stochastic parameterization of the internal-wave field affects the statistics of the received acoustic observables.

A deterministic analysis of sound propagation through internal wave fields was initiated in the mid 1970's by DeFerrari *et al*[13]. This study was limited to an internal wavefields impact on acoustic traveltime. By 1980, the deterministic approach was abandoned, and the research community exclusively selected the path integral (stochastic) technique. The deterministic approach was resurrected by Techau in the late 1980s. This framework was employed to demonstrate that oscillatory perturbations to a range-invariant sound-speed profile can cause the amplitude of early arrivals to change without significantly changing the arrival traveltime (phase) [14]. Ray tracing was used in a 2D ocean model. Techau used the concept of timefronts [15] to describe the model ocean impulse response.

In this dissertation, a numerical simulation tool was developed to simulate long-range acoustic propagation through deep ocean internal wave fields. For long-range propagation numerical simulations, the amount of computing power available is a major factor when determining the detail of the ocean model. Since computing power will steadily increase through the years and ocean processes are rather slowly moving (time scales of hours), there is interest in how a given internal-wave field, which could be thought of as a single realization of a random field, deterministically affects acoustic propagation in hopes that future models can estimate and track large-scale ocean processes. This would not only yield valuable oceanographic information, but also may allow signal processesors to estimate and

remove the effects of these processes on the received acoustic arrival, allowing for longer coherent integration times and improved ocean process estimates.

1.3   Research goals

A goal of this research is to establish the feasibility that internal waves can cause early acoustic arrivals to have fluctuating time-domain amplitude coincident with stable time-domain phase. The interest in early wavefront arrivals is because these acoustic arrivals are expected to be resolved and changes in traveltime can be monitored. The fluctuating amplitude and stable phase phenomenon has been observed during long range acoustical experiments and has been previously unexplained. This requires an establishment of a numerical simulation tool for long-range acoustic propagation that is in agreement with fundamental physical principles as well as experimental observations. With such a tool in place, it is a goal of this research to demonstrate the extent individual internal waves can be identified via a deterministic interpretation of the received acoustic waveform.

1.4   Research path

Pursuing these research goals has revealed a wealth of information on modeling long-range deep-ocean acoustic propagation and receptions. An overview of the research path followed to meet the goals is listed and summarized. These topics are addressed in detail in the dissertation and lead to a comprehensive contribution to the field of underwater acoustic modeling and signal processing.

Initially, a numerical simulation tool is needed to simulate acoustic propagation through deep ocean internal wave fields. The tool consists of three major components: a description of the sound speed field (ocean model), simulation of acoustic propagation through the field based on a numerical solution of the wave equation (propagation method), and signal processing of the simulated received acoustic waveform. In developing these resources several research products were developed and are listed below here.

□ Importance to clearly define the physical and computational ocean models

- Development and validation of a low-frequency broadband ray-tracing propagation method
- Derivation and validation of a 3D ray tracing propagation method

- Development and validation of a method to construct diffracted wavefronts

Given the ability to simulate long range acoustic propagation through internal wave fields, it is desirable to determine if any class of internal wave modes significantly impacts the acoustic reception. These internal wave modes will most likely be successfully identified through a deterministic analysis of the acoustic reception.

- Established that internal waves that are spatially synchronized to an arrival's acoustic path cycle length significantly affect the acoustic reception, while spatially non-synchronized internal waves have little impact on the reception
- Established conditions under which spatially synchronized internal waves coherently focus and defocus the acoustic wavefront in the vertical plane
- Established conditions under which spatially synchronized internal waves coherently focus and defocus the acoustic wavefront in the transverse plane
- Comparisons of 3D and N x 2D modeling techniques demonstrate that complete 3D modeling techniques are required to deterministically simulate long range acoustic propagation through internal wave fields

Long-range acoustic propagation is simulated using a 3D time-varying computational ocean model and a ray tracing propagation method. A reduced internal wave model is employed that includes one to a few spatially synchronized internal waves and several spatially non-synchronized internal waves. The simulation results from the reduced internal wave model are consistent with fundamental observations of long range acoustical experiments.

- Established the feasibility that internal waves can cause early acoustic arrivals to have Rayleigh-like amplitude fluctuation coincident with stable time-domain phase
- Simulated early acoustic receptions were determined to consist of a single coherent wavefront sheet for a 750 km range
- Experimental data shows consistency with the modeled data

The nature of the research was exploratory. A deterministic framework for long-range acoustic propagation is established to host underwater acoustic signal processing algorithms. This work contributes to establishing the direction of future signal processing algorithms

such that they will contain a detailed deterministic description of the physics of acoustic propagation.

CHAPTER 2

Physical and computational ocean models

Table 2.1 shows the fundamental building blocks required to simulate acoustic propagation through the ocean and analyze the received acoustic waveform. The basic process consists of characterizing a physical description of the ocean features that impact acoustic propagation. In this study, the physical motion of internal waves are characterized by a second-order differential equation and associated boundary conditions. This description is mapped to a 3D and time varying sound speed field called the *physical ocean model*. For computer implementation, the physical ocean model is translated to a *computational ocean model*. This is the sound speed field that is coded into the numerical simulation. It is

Physical ocean model (Physical Characterization of the Sound Speed Field)
Computational Ocean Model (Computer Implementation of the Sound Speed Field)
Propagation Method (Numerical Simulation of Acoustic Propagation)
Signal Processing (Extraction of Information from Received Acoustic Waveform)

Table 2.1: Building blocks of acoustic propagation simulation and analysis

desirable to have these two ocean models equivalent, but most implementations make this prohibitive based on limitations in computer instruction rates and memory. With a computational ocean model in place, the wave equation is numerically solved using a *propagation method*[1] to simulate acoustic propagation. Several propagation methods have been developed [16]. *Signal processing* algorithms are developed to extract oceanographic or source signal information from the received acoustic waveforms. The trend in the underwater acoustic signal processing community is to incorporate details of the physical propagation into the framework of the signal processing algorithms as evidenced in [4] [17] [18], and [19]. The propagation methods and signal processing techniques will be addressed in following chapters. This chapter focuses on physical and computational ocean models describing the deep ocean acoustic channel.

2.1 Physical ocean model

Many long-range sound experiments have shown that seasonal variations, internal waves, tides, Rossby waves, currents, and mesoscale eddies impact acoustic transmission[5]. By the mid 1970's oceanographers had identified internal waves as the most important source of variability on time scales less than 12 hours[6]. The physical ocean model employed here is a combination of a range-invariant Munk sound-speed profile and space and time varying perturbations to the sound speed profile induced by horizontally propagating internal waves. These two contributions to the sound-speed field will be described independently, then combined in a sensible way according to [5].

2.1.1 Munk profile

The Munk profile is a popular academic sound-speed profile for mid-latitude deep-ocean regions[20]. The speed of sound is a function of temperature and pressure. Temperature changes dominate the shape of the sound-speed profile near the ocean surface, and changes in pressure dominate the shape of the sound-speed profile in the deeper ocean. These competing effects cause a sound speed minimum typically near a depth of 1 km. The

---

[1]The phrase *propagation method* refers to a computer method to simulate acoustic propagation.

13

sound speed does not typically vary by more than 5% over the water column, but this variation is significant for acoustic propagation. Propagating sound is refracted toward the depth of minimum sound speed, the sound channel axis, and thus, the deep ocean acts as a waveguide.

The Munk profile, $c_{\text{Munk}}(z)$, describes the sound speed as it varies with depth. It describes the primary features of the deep-ocean channel[20]. The formula for the sound speed as a function of depth is

$$c_{\text{Munk}}(z) = c_0[1 + \epsilon(e^{-\eta} + \eta - 1)] \tag{2.1}$$

where c_0 is the minimum sound speed, $\eta = 2(z - z_0)/b$, z_0 is the depth of the minimum sound speed, ϵ is a dimensionless parameter controlling the overall sound-speed variation, and b is the buoyancy decay parameter.

Two sound-speed profiles were used in this work. Their profiles are plotted in Figure 2.1. The solid curve represents a Munk profile commonly used for academic studies. The following parameter values are used to define $c_{\text{Munk}}(z)$: $z_0 = 1200\,\text{m}$, $c_0 = 1480\,\text{m/s}$, $b = 1040\,\text{m}$, $\epsilon = 0.006$. The dashed curve represents a Munk profile fit to environmental data taken during a long range acoustic experiment in the North Pacific. This data is known as the SLICE 89 data[12]. The following parameter values are taken to define $c_{\text{S89}}(z)$: $z_0 = 800\,\text{m}$, $c_0 = 1478\,\text{m/s}$, $b = 533\,\text{m}$, $\epsilon = 0.003$.

2.1.2 Internal waves

Internal waves are slowly moving density waves and are similar to the familiar ocean surface waves, except they occur internal to the ocean. For a detailed description of internal waves see [21].

The displacement of all internal waves with a given wavenumber, k in radians/meter, can be described in terms of a series of horizontally propagating modes each of the form, $W_j(k, z) \cos(k_x x + k_y y - \omega_j(k)t)$. Here x, y, z form a Cartesian coordinate system. $W_j(k, z)$ is internal wave mode j of wavenumber k, and it describes the relative vertical displacement of an isodensity with equilibrium depth z. The internal-wave angular frequency for each mode is denoted by $\omega_j(k)$ in radians/second. Without internal waves the relevant acoustic

14
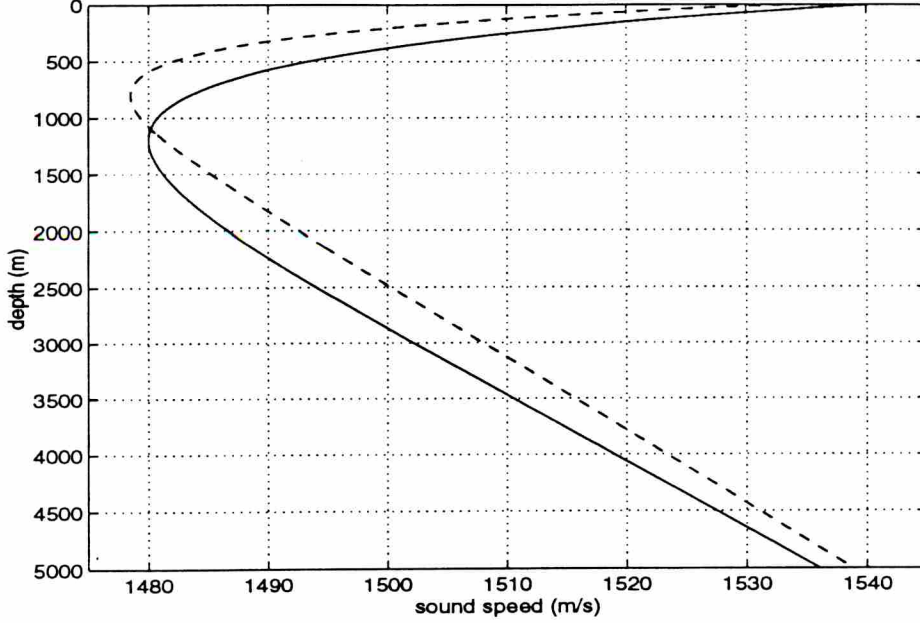
Figure 2.1: **Munk sound-speed profiles. The parameters for the two sound speed profiles are defined in the text. The solid curve represents $c_{\mathrm{Munk}}(z)$, and the dashed curve represents $c_{\mathrm{S89}}(z)$.**

propagation is in the XZ-plane, and the corresponding horizontal direction is the *nominal acoustic direction*. The angle the internal-wave propagation direction makes with respect to the nominal acoustic direction is denoted by θ, so that $k_x = k \cos \theta$ and $k_y = k \sin \theta$. This geometry is described in Figure 2.2

The discrete set of internal waves for a given wavenumber, k, is obtained through the "eigen" solutions of the following differential equation (derived from the equations of motion)[21].

$$\frac{\partial^2 W_j(k,z)}{\partial z^2} + k^2 \left(\frac{N^2(z) - \omega_j^2(k)}{\omega_j^2(k) - \omega_i^2} \right) W_j(k,z) = 0 \qquad (2.2)$$

The physically reasonable boundary conditions are zero vertical displacement at the surface, $W_j(k,0) = 0$, and at the bottom of the ocean, $W_j(k,z_b) = 0$.

The "shooting method" with a fourth-order Runge-Kutta integrator was used to solve for the internal-wave functions and corresponding wavenumbers[22]. A Bessel function based solution was also employed as a check[5]. The modes are ordered such that $\omega_j(k) < \omega_{j+1}(k)$. The inertial angular frequency, ω_i, is a function of the latitude and is introduced by including

15
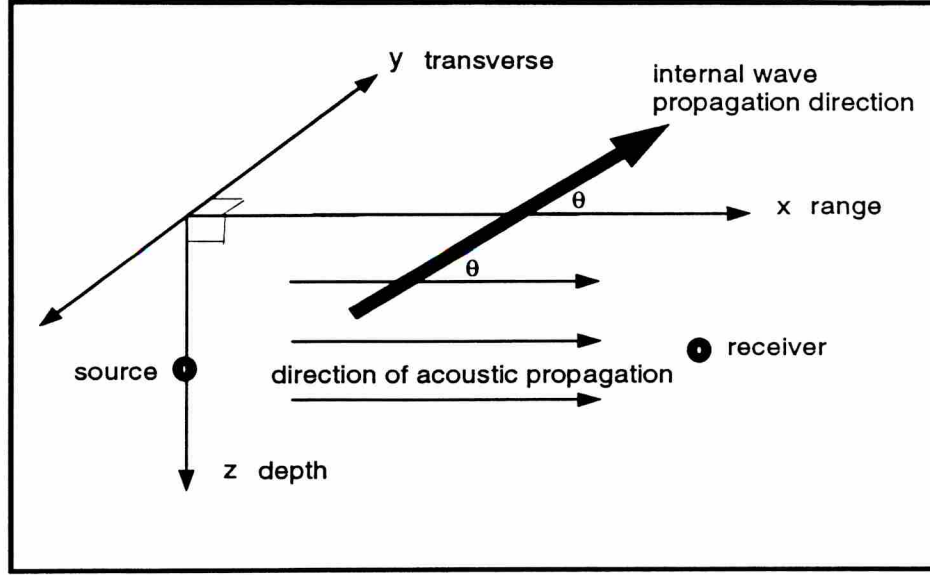
Figure 2.2: The Cartesian coordinate system, direction of acoustic propagation, and internal wave propagation direction are defined.

the Coriolis acceleration into the equations of motion. The inertial frequency takes values from 0 cph (cycles per hour) at the equator to $0.08\bar{3}$ cph at the poles. The density gradient is described in terms of the buoyancy frequency, $N(z)$, the frequency at which an isodensity displaced from its equilibrium position will oscillate.[2] A simple and accepted model of the buoyancy frequency is to assume an exponential decrease with depth, z

$$N(z) = N_0 e^{-z/b} \qquad (2.3)$$

where b is the buoyancy decay parameter and N_0 is the extrapolated surface buoyancy frequency. When an external force displaces water from the equilibrium positions, internal waves result.

From measurements and analysis, Garrett and Munk have determined strengths for normalized internal waves [6]. The modes $W_j(k, z)$ are normalized according to the following condition

$$\int_0^{z_b} (N^2(z) - \omega_i^2) W_j^2(k, z) dz = 1 \qquad (2.4)$$

For a given wavenumber, k, a majority of the internal-wave energy tends to reside in the lower-order modes; however, the higher-order modes may have an important affect on the

---

[2]Electrical engineers would call this the impulse response frequency or pole frequency of a circuit.

received waveform and thus cannot be ignored. Using a stochastic ocean model, Colosi *et al* found that only internal waves of mode $j < 10$ significantly impact early arrival wavefront statistics [12].

Consider M propagating internal waves present in the ocean that influence acoustic propagation. The mth internal wave has vertical shape $W_{j,m}(k_m, z)$ of the jth mode with wavenumber k_m, and has angular frequency $\omega_{j,m}$, all related by Equation 2.2. In the model this internal wave is given an amplitude and phase represented by the complex number $G_{j,m}(k_m, \theta_m)$, where θ_m is the horizontal angle of travel of this internal wave relative to the nominal acoustic direction.

The displacement of an isodensity by the mth internal wave is

$$\zeta_m(x, y, z, t) = \Re e \left(G_{j,m}(k_m, \theta_m) W_{j,m}(k_m, z) \, e^{i(k_m x \cos \theta_m + k_m y \sin \theta_m - \omega_{m,j}(k)t)} \right) \qquad (2.5)$$

The aggregate displacement is the sum of these propagating internal wave displacements.

$$\zeta(x, y, z, t) = \sum_{m=1}^{M} \zeta_m(x, y, z, t) \qquad (2.6)$$

Following [5], the change in sound speed induced by the internal waves is related to the displacement of the isodensity by

$$\delta c(x, y, z, t) = 2.5 \, c_o \, N^2(z) \, \zeta(x, y, z, t) \qquad (2.7)$$

Three internal wave modes are plotted in Figure 2.3. The change in sound speed, $\delta c(z)$, for a fixed time and x-y location is plotted. The assumed monotonically decreasing form of the buoyancy frequency, $N(z)$, in Equation 2.3 causes the the internal wave modes to be an oscillatory function above some critical depth and an exponentially decaying function below this depth. The critical depth is a function of the internal wave angular frequency and is the depth where

$$N(z) = \omega_j(k) \qquad (2.8)$$

since this is the condition the non-constant coefficient of the bracketed term in Equation 2.2 equals zero. This accounts for the majority of the internal wave induced change in sound speed being in the shallower depths, typically within the first kilometer.

In the current research the complex magnitudes $G_{j,m}$ are picked to have reasonable or interesting magnitudes consistent with the Garret-Munk spectrum. They are not random
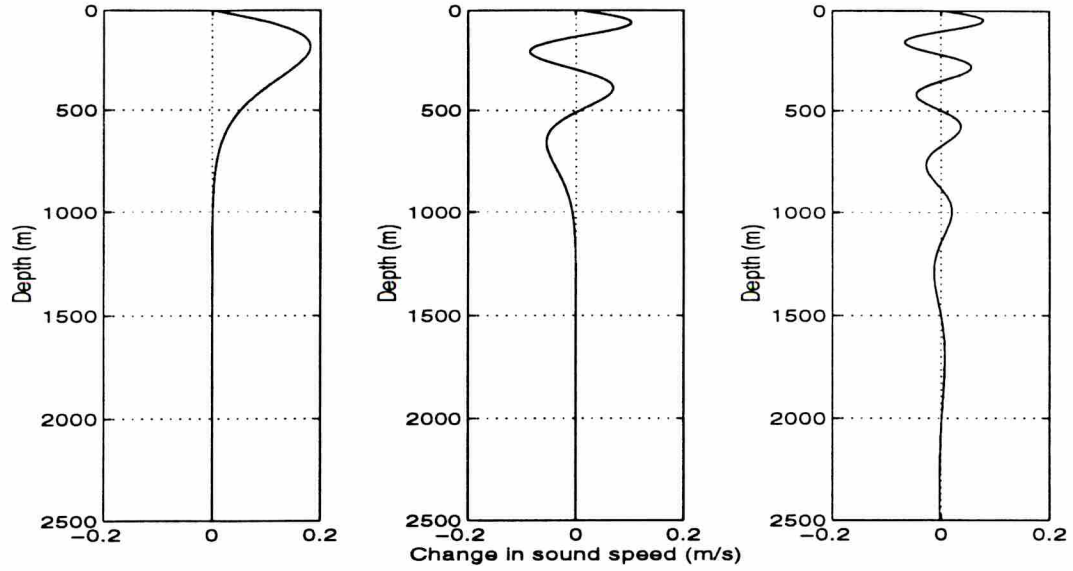
Figure 2.3: δc **for three internal-wave modes** $W_j(k, z)$**: left:** $j = 1$, $k/2\pi = 1.315$ **cyc /km,** $\omega/2\pi = 2.00$ **cyc/hr center:**$j = 4$, $k/2\pi = 2.046$ **cyc /km,** $\omega/2\pi = 1.31$ **cyc/hr right:** $j = 10$, $k/2\pi = 0.231$ **cyc /km,** $\omega/2\pi = 0.14$ **cyc/hr.**

processes of time or space. The amplitude and propagation direction of the internal waves do not change over the 750 km range and four hour interval used to study their impact on acoustic propagation.

It is recognized that this coherence may not be consistent with stochastic internal wave theory. It is part of the assumptions made to initiate a deterministic analysis.

2.1.3 Physical ocean model: an example

After establishing a set of internal waves to be included in the sound speed model, the 3D time-varying sound-speed field is completely specified by

$$c(x, y, z, t) = c_{\text{Munk}}(z) + \delta c(x, y, z, t) \tag{2.9}$$

where $c_{\text{Munk}}(z)$ is defined in Equation 2.1, and $\delta c(x, y, z, t)$ is defined in Equations 2.3 - 2.7.

Equation 2.9 is the physical ocean model used for this study. A physical ocean model is a representation of the sound-speed field based on the understanding of the physical ocean processes under study. In other words, no compromises have been made to accommodate

18

symbol	definition	Value
j	internal-wave mode number	1 - 21
$k_m/2\pi$	internal-wave cyclic wavenumber	0.10 to 2.10 cyc / km
θ_m	internal wave propagation direction angle	0° to 360°
$G_{j,m}(k,\theta)$	internal-wave amplitude and phase (complex)	$\mid G \mid < 10$
$\omega_{j,m}(k)/2\pi$	internal-wave frequency	0.1 to 2.0 cph
M	number of internal waves	1 - 7
$\omega_i/2\pi$	inertial frequency	0.05 cph
$N_0/2\pi$	surface buoyancy frequency	3 cph
b	buoyancy frequency decay parameter	1040 m
c_0	minimum sound speed for Munk profile	1480 m/s
z_0	depth of minimum sound speed	1200 m
ϵ	strength of deviation for Munk profile	0.006

Table 2.2: Summary of ocean model parameters

for computer limitations or the particular propagation method. Physical ocean models are 3D and time-varying.

Table 2.2 lists the parameters required to define the physical ocean model. Column three of the table defines the parameters or range of parameters used in the simulations. The parameters in the first 4 rows of the table are selected for each of the M internal waves. The internal-wave frequency, $\omega_{j,m}(k)$, is determined by specifying the wavenumber, k_m, and mode number, j, but is included for completeness. The later 5 rows of the table specify the range-invariant properties of the deep ocean channel.

2.2   Computational ocean models

Researchers would like to use a computational ocean model consistent with the current physical understanding of internal waves, a full complement of modes generated from Equation 2.2 in accordance with the Garrett-Munk spectrum. Unfortunately, modern computer limitations do not allow implementation of a full 3D time-varying internal wave model over megameter ranges using the method of Equation 2.9. To use this approach, compromises must be made. Recently, Colosi *et al* used a 2D computational ocean model and represented the Garrett-Munk spectrum by using hundreds of internal waves[12]. In this dissertation, a full 3D time-varying computational ocean model was used, but the number of internal waves was limited to make the model computationally implementable. Fortuitously, in Chapter

4 it is shown that early acoustic arrivals are sensitive to a reduced class of (spatially synchronized) internal waves. In some sense, it is possible that these internal waves may fairly represent the Garret-Munk spectrum in that we are modeling the few modes (from a much larger set of modes) that significantly impact this specific acoustic reception.

As previously mentioned, it is common to represent the physical ocean model using a 2D computational ocean model in range and depth. This model is obtained from the 3D physical ocean model by setting $y = 0$ in Equation 2.9. However, the actual 3D physical ocean model corresponding to this 2D computational ocean model is one where all internal waves are propagating in the direction of sound propagation (or the exact opposite direction); thus, $\theta_m = 0°$ or $180°$, so that $k_y = 0$ and $k = \pm k_x$. However when y is set to zero the term $k_m y \sin \theta_m$ is effectively removed from Equation 2.9, and a new set of effective k values are generated, namely $k_m \cos \theta_m$, that have corresponding modes, $W_{j,m}(k_m, z)$, and frequencies, $\omega_{j,m}(k)$, that are not consistent with Equation 2.2.
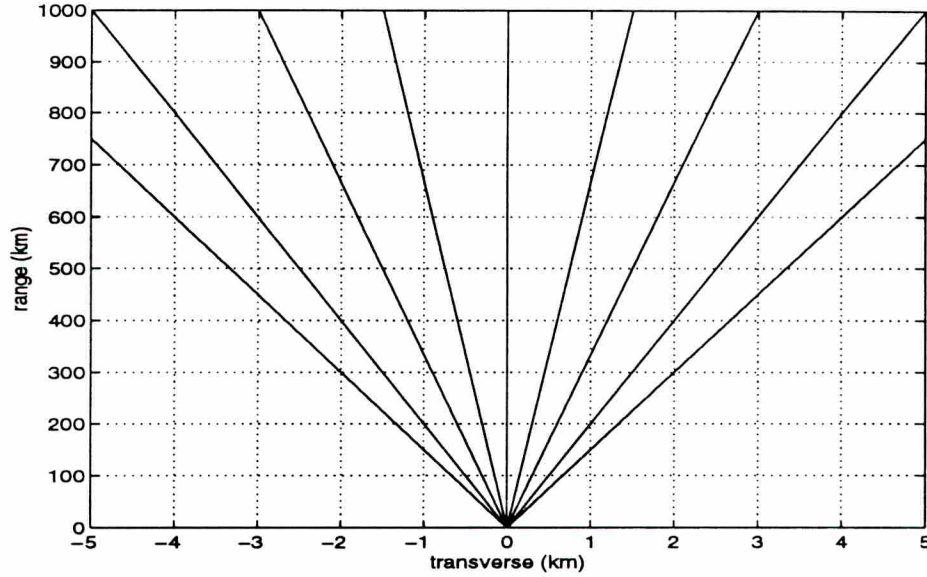
Figure 2.4: This is a plan view showing the planes used for N x 2D propagation.

From another view, only when the physical ocean model is composed of internal wave modes traveling in the nominal acoustic plane is a 2D computational ocean model consistent with the physical ocean model. Other than this degenerate case, a 2D computa-

20

tional ocean model does not maintain internal wave direction information. Moreover, and very importantly, the 2D computational ocean model neglects transverse refraction. Since $\partial(\delta c)/\partial y \neq 0$, rays will refract out of the nominal acoustic plane, and this refraction carries information on the internal-wave modes present in the field.

One way researchers model a 3D field is to propagate the sound over several 2D slices of the ocean, this is called N x 2D modeling [24]. Figure 2.4 shows a plan view of the ocean describing the N x 2D propagation planes. For a source at coordinate $(x, y) = (0, 0)$, the acoustics are propagated within the planes depicted in the figure. Typically, N is on the order of 10 or 100 depending on the range and variability of the ocean model. Since, for each slice the sound is constrained to the 2D slice in which it originates, we have the same physical interpretation as the case where the acoustics are forced to remain in a 2D plane. For this reason, even considering an infinite number of 2D slices, results from this modeling technique do not approach that of a 3D model when internal waves are present.

After establishing the ocean model to be studied, the wave equation must be solved over this model to simulate acoustic propagation. There are several methods to accomplish this, all with different and varying degrees of assumptions. The propagation methods suitable for long range deep ocean propagation are investigated in the following chapter.

CHAPTER 3

Methods of Propagation Simulation

This chapter addresses methods to simulate long-range acoustic propagation through the deep ocean. The focus is on propagation methods (methods to simulate acoustic propagation) suitable for 3D computational ocean models. This leads to an investigation of 3D low frequency broadband ray tracing.

3.1 Overview: normal modes, PE, rays

Table 3.1 summarizes a selection of the propagation methods available to simulate acoustic propagation through 2D range invariant, 2D range variant, and 3D space variant computational ocean models. Each of the propagation methods will be addressed in the following sections and supporting appendices. Three brands of propagation methods are addressed: normal mode methods, parabolic equation (PE) methods, and ray tracing methods. A propagation method not studied here is based on a direct discretization and numerical integration of the wave equation[16]. This approach is computationally intensive and is prohibitive for long range acoustic modeling and has been limited to the solution of special short range scattering problems[16].

Validation of a propagation method within the framework of the computational ocean model under study is critical. Subsequent analysis and processing carries little or no meaning if the propagation method produces erroneous received acoustic waveforms. Unfortunately, the only propagation method that yields a ground truth[1] received waveform is the normal mode solution to the wave equation restricted to range invariant computational ocean mod-

---

[1]The phrase *ground truth* refers to an a solution known to be exact.

Computational Ocean Models	2D		3D
	Range invariant	Range variant	Space variant
Normal Modes	Ground truth	Not ground truth. Adiabatic approximation used to extend method to range varying ocean models.	2D methods used in an N × 2D framework to approximate 3D modeling.
PE	Low-angle approximation. Inaccurate modeling of early wavefront arrivals	Popular Method. Incorporates diffracted, refracted, and reflected energy; thus considered a " full physics" method.	Impractical implementation. 2D methods used in an N × 2D framework for 3D modeling.
Ray Tracing	High-frequency approx. Accurate modeling of early wavefront arrivals. Does not incorporate diffraction.	Computationally efficient	Practical implementation

Table 3.1: **This table comments on the utility of the normal mode, PE, and ray tracing propagation methods for 2D range invariant, 2D range variant and 3D space variant computational ocean models.**

els. Certain contrived range varying cases have "ground truth" solutions as well [25], but these solutions do not offer assistance to validating propagation methods used in internal wave field ocean models. To study the effect of an internal wave field's impact on acoustic propagation, a time and space variant computational model is needed. As a first step, candidate propagation methods must be benchmarked against the normal mode method in a range invariant model to establish an upper bound on the accuracy expected for propagation through range varying models. Extensions of a propagation method to range varying models should be handled cautiously. The normal mode propagation method is reviewed in Section 3.2.

Simulating acoustic propagation through 2D range invariant computational ocean models (Column one of Table 3.1) will be addressed by benchmarking the PE and ray tracing

propagation methods against the normal mode ground truth case. A specific benchmarking exercise is described in Section 3.5 to illustrate the general result that the ray propagation method is superior to the standard PE propagation method for the modeling of early wavefront arrivals after long range propagation through the deep ocean.

The PE propagation method uses a first-order approximate form of the wave equation (called the parabolic wave equation) and Fast Fourier Transform techniques to efficiently compute the vertical acoustic pressure field[2], $p(x_o, z)$, in a range-wise recursive manner. Said symbolically, $p(x_o, z) \rightarrow p(x_o + \Delta x, z)$. Given a vertical acoustic pressure field at the source, this solution is conducted repeatedly to march the vertical acoustic pressure field in range over great distances. The computed pressure field represents a single frequency waveform. Broadband acoustic propagation is simulated by repeating the procedure for many (maybe hundreds) of frequencies within the acoustic operational bandwidth. In Table 3.1, the attributes listed for the PE propagation method for 2D range-variant and 2D range-invariant computational ocean models actually apply to each method; that is, all 2D PE simulation of propagation is regarded as inaccurate modeling of early arrivals and considered a "full physics" method. The standard PE propagation method is reviewed in Section 3.3.

The standard ray tracing propagation method is based on a high frequency solution to the wave equation. The propagating acoustic wavefront is computed by tracing rays. Rays are traced by numerically integrating a set of differential equations. A large number of rays at varying initial trajectories can be traced to simulate acoustic propagation of an impulse from a source. In general, the impulse response is denoted by $h_{x_o, y_o, z_o, t_o}(x, y, z, t)$ and defines the location (x, y, z) of the impulse after t seconds of propagation from a source located at (x_o, y_o, z_o) emitted at time t_o. The impulse response is evaluated by fixing one or more of the impulse response arguments. The notation $h_{x_o, y_o, z_o}(x, y, z, | t = T)$ defines the location of the impulse in space after T seconds of propagation[3]. For 2D computational ocean models the y coordinate is suppressed, $h_{x_o, z_o}(x, z | t = T)$. This impulse response is called a *timefront*. The acoustic rays travel normal to the timefront. The notation $h_{x_o, y_o, z_o}(z, t | x = X, y = Y)$ defines the impulse response to a fixed range (and transverse

---

[2]The vertical acoustic pressure field is the pressure across depth evaluated at a given range, $p(x_o, z)$.

[3]For time-invariant computational ocean models, the transmission time, t_o is typically suppressed.
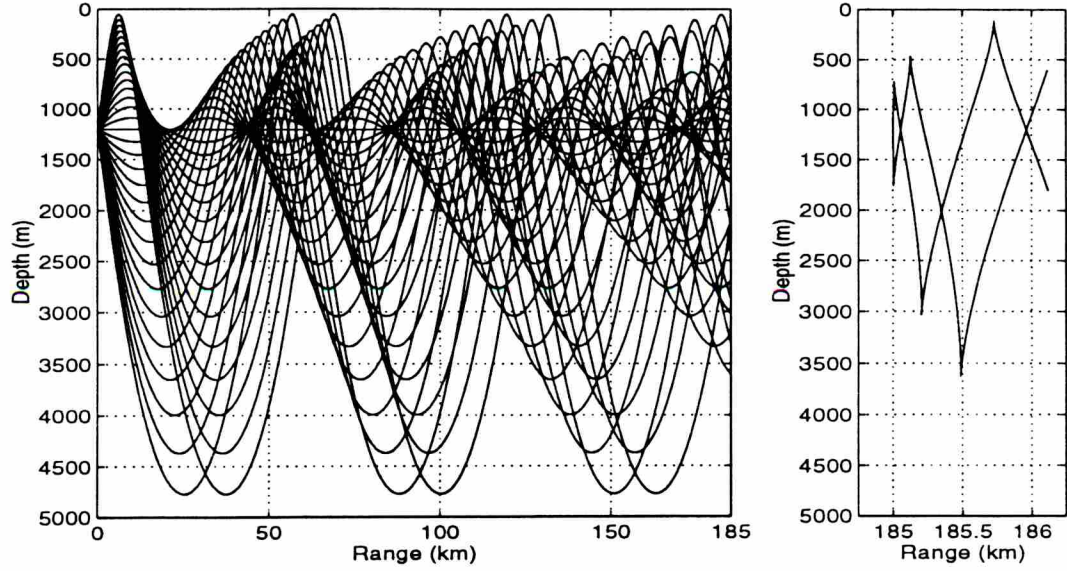
Figure 3.1: The figure to the left shows the ray paths propagated through a deep ocean channel. Clearly, the sound is refracted away from the ocean surface and bottom allowing for successful long range propagation. The figure to the right shows a timefront. The rays were propagated each for 125 seconds. The ray endpoints are connected to construct the current position of the front. The accordion shape is typical for deep ocean propagation.

coordinate for 3D modeling). This is the impulse response <u>measured</u> by a vertical line array[4] and for this reason serves great utility. This impulse response is termed a *measurement front*. Similarly, the notation $h_{x_o,y_o,z_o}(t \mid x = X, y = Y, z = Z)$ defines the impulse response at a single hydrophone at location (X, Y, Z) from a source located at (x_o, y_o, z_o). This is termed the *phone impulse respone*.

In Figure 3.1, rays are traced through the range-invariant deep ocean sound-speed model, $c_{\mathrm{Munk}}(z)$. The rays traced have one degree separation in launch angle, the ray inclination at the source and range between $\pm 15°$. The low angle acoustic energy travels near the sound channel axis and lags the high-angle acoustic energy. The high-angle energy travels near the ocean surface and bottom and is received first at a receiver down range. Energy outside of this $\pm 15°$-swath will reflect off the ocean surface and is assumed to not propagate over long ranges. The source is located on the sound channel axis at a depth of 1200 m. The

---

[4]A vertical line array is a set of hydrophones positioned along a vertical line

25
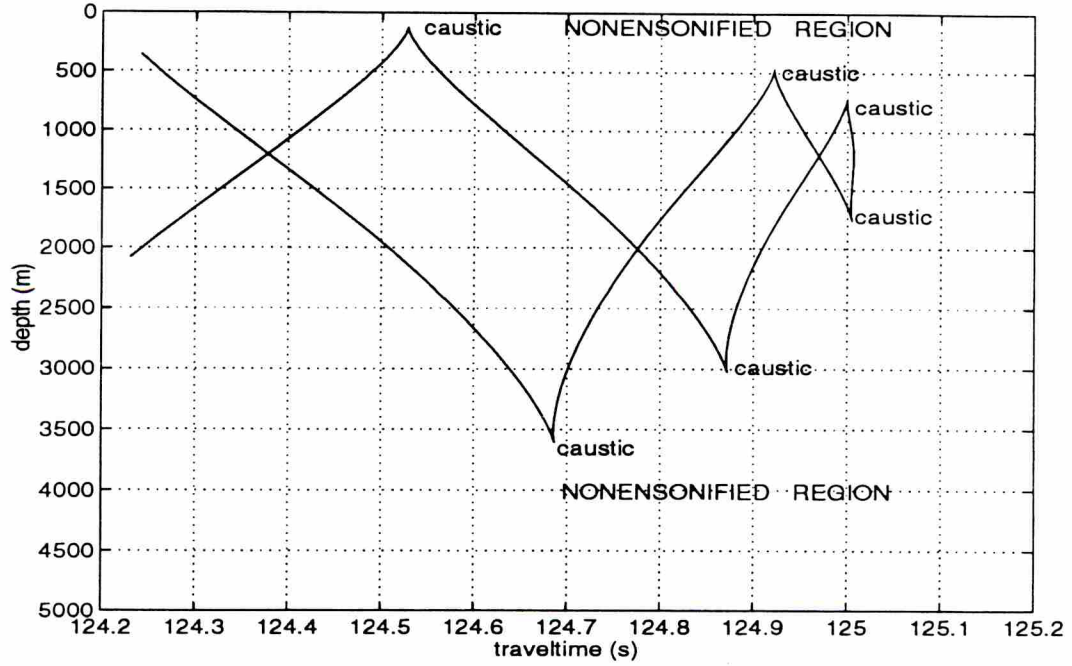
Figure 3.2: Measurement front at a range of 185 km through a deep ocean sound speed profile. The number of totally refracted arrivals and their traveltimes can be determined for a receiver at any depth. An axial receiver, in this case at 1200 m deep, will receive 7 pulses, two sets of two which will arrive simultaneously at 124.38 and 124.98 seconds. There are six caustic points and they are labeled on the figure. Exterior to the measurement front is the non-ensonified region or shadow zone. This area will not receive totally refracted wavefronts computed using ray tracing techniques; however, diffracted wavefronts are known to exist in this region from complete solutions of the wave equation and experimental measurements.

ray paths paint the location the acoustic field has traveled, giving an intuitive view of deep ocean acoustic propagation. It is clear that the rays are refracted away from the ocean surface and bottom to channel the acoustic energy and allow propagation over long ranges. The rays are traced each for a fixed time of 125 seconds. By connecting the ray endpoints a timefront, $h_{x_o=0m,z_o=1200m}(x, z \mid t = 125s)$, is formed and is shown in Figure 3.1 to the right. It is useful to determine the amplitude and phase along the timefront so that a source signal can be convolved with the timefront to determine the source response. These issues are addressed in subsequent sections.

26

The ray paths create sharp boundaries between ensonified regions and non-ensonified regions. This boundary is called a caustic and is the result of infinite-frequency computations where diffraction effects are not incorporated. A caustic point is the location of which two adjacent ray paths cross. Caustic points are identified on timefronts or measurement fronts as places where two sheets connect at a cusp. The non-enosonifed regions are located above surface-side cusps and below bottom-side cusps. The term "non-ensonified" is a misnomer in that diffracted acoustic energy leaks into this region.

An example of a measurement front, $h_{x_o=0m, z_o=1200m}(z, t \mid x = 186km)$ is shown in Figure 3.2 for the range-invariant deep ocean sound-speed model $c_{\text{Munk}}(z)$. The range of 186 km is approximately equivalent to 125 seconds of propagation. The measurement front has a reversed shape with respect to the timefront in Figure 3.1. The caustic points, cusps, and non-ensonified regions are labeled in the figure. The ray propagation method is further described in Section 3.4.

Column 2 of Table 3.1 addresses propagation methods for 2D range variant computational ocean models. For this case, the PE propagation method has gained overwhelming popularity in the research community of underwater sound propagation. Because both diffracted, refracted, and reflected energy is modeled for low frequency acoustic signals, researchers call the PE propagation method a "full physics" solution to the wave equation; however, the construct of the PE recursion is not an exact solution to the wave equation. The normal mode expansion loses its ground truth superiority for range variant computational ocean models; however, the adiabatic approximation can be employed to maintain the normal mode construct through a range varying model [19]. The adiabatic approximation assumes that modes do not transfer energy to other modes. In actuality, modes transfer energy during propagation. This is called mode coupling and is described by equations which lead to a computationally expensive implementation[16]. Two-dimensional range-variant ray tracing is computationally efficient but as with all standard ray tracing computations, carries the burden of being based on a high frequency approximation. With current and future long range, deep ocean acoustical experiments moving to lower acoustic frequencies, ray propagation techniques have fallen out of favor. A comparison of propagation methods in a 2D range varying computational ocean model is addressed in Section 3.7.

27

If the complete dimensionality of the physical ocean model must be maintained in the computational ocean model, a 3D space varying model is necessary. Any propagation method suitable for 2D range varying computational ocean models can be artificially extended to a propagation method in a 3D computational ocean model by propagating within a series of 2D computational ocean models at different azimuth angles from the receiver. This is called N x 2D modeling as described in Chapter 2 and currently is the most popular model used to study 3D propagation. These computations confine the acoustics to the 2D plane and do not allow the expression of the effects of transverse refraction on the acoustic reception. For a deterministic investigation of long-range acoustic propagation it is imperative to maintain the complete three-dimensionality of the ocean model, and N x 2D modeling leads to inaccurate results[5].

Column 3 in Table 3.1 addresses propagation methods for 3D space varying computational ocean models. Normal mode propagation methods through a 3D computational ocean model have been addressed within an N x 2D framework [26]. Others have propagated normal mode solutions along a given ray path in a 3D model. This approach is applicable when the entire vertical acoustic pressure field is similarly transversely refracted, as expected to result from sound speed changes caused by mesoscale eddies or bathymetric features but not for sound-speed perturbations caused by internal waves. The PE propagation method can be derived for complete 3D computations; however, the implementation is effectively not implementable due to prohibitive computer run times and memory requirements[27]. The utility of ray tracing is it's flexibility. By adding two additional first-order differential equations to the suite of equations for numerical integration, ray tracing can be extended to complete 3D computations. **With present day computers, ray tracing is the only viable 3D propagation method for 3D computational ocean models.** With this being the case, the high frequency approximation must be seriously addressed, and a procedure must be developed and validated to establish a 3D, low-frequency, broadband, ray tracing propagation method. First, the normal mode and PE propagation methods are reviewed followed by the development of 3D low frequency broadband ray tracing.

---

[5]This is demonstrated in Chapter 4

3.2   Normal modes: the ground truth solution

For sound propagation through a range invariant sound speed profile, the normal mode solution to the wave equation is essentially exact. Normal modes are physical, not only a mathematical basis, in the sense that each mode describes an acoustic disturbance which propagates horizontally through the environment independently of all other modes[28].

For a 2D range invariant computational ocean model, the normal-mode constructed complex baseband time-domain waveform for a given depth and range is[16]

$$p_{mode}(x,z,t) = e^{i\pi/4} \int_{-W}^{W} \tilde{S}(f) \sum_{m=1}^{M} U_m(\Omega, z_s) U_m(\Omega, z) \sqrt{\frac{2\pi}{\kappa_m(\Omega)x}} \, e^{-i\kappa_m(\Omega)x} \, e^{i2\pi ft} \, df \quad (3.1)$$

This solution results from the separability of range and depth in solving the wave equation. The first M normal modes are summed. Each normal mode represents a broadband waveform. The solution is not precisely *ground truth* in that an infinite number of normal modes have not been included in the sum; however, for long range scenarios this solution can be regarded as ground truth within certain bounds.

Constructing a received waveform using normal modes is straight forward once the normal-mode functions, $U_m(\Omega, z)$, and wavenumbers, $\kappa_m(\Omega)$, for the desired sound-speed profile and frequency band are obtained. The source at depth z_s is specified by its spectrum, $\tilde{S}(f)$, which covers an operational bandwidth of $f_c - W$ to $f_c + W$. An unconventional but useful notation to distinguish baseband functions from passband functions is established

$$\Omega = 2\pi(f + f_c) \quad (3.2)$$

All passband functions have angular frequency arguments, and all baseband functions have cyclic frequency arguments. The normal-mode (eigen) functions and wavenumbers (eigenvalues) are obtained through normalized solutions of a second-order differential equation. The solutions of the equation are obtained numerically, and this is no easy task when accuracy is at a premium. To declare the normal-mode constructed waveforms for a range-invariant sound-speed profile as the "ground truth" solution, the normal-mode functions and wavenumbers must be very accurate, a large number of normal modes must be included, and the receiver must be sufficiently distant so that the continuum of evanescent

modes (the spatial transient due to a small source size) have died out. This concern is further addressed in Appendix A.

There are an ensemble of ways to extend the normal mode solution to an approximate solution in range-variant computational ocean models. Using the adiabatic approximation and eigenvalue perturbation formula [19], one can map internal wave induced perturbations to the sound speed profile to perturbations in the modal wavenumber. $\Delta c(x, z) \rightarrow \Delta \kappa_m(\Omega, x)$, and $\kappa_m(\Omega)x$ is replaced by $\kappa_m(\Omega)x + \int_0^R \Delta \kappa_m(\Omega, x')dx'$ in Equation 3.1. This technique leads to a reasonably efficient implementation for internal-wave sound-speed perturbations; however, as illustrated in Section 3.7, the utility of this technique is suspect for long range propagation through internal wave fields.

3.3   Parabolic equation

Application of the parabolic equation (PE) is attributed to Leontovich and Fock for their work in radio wave propagation in the atmosphere in the 1940s. The work was introduced to the underwater sound community by Hardin and Tappert in the early 1970s[29]. The method reduces the wave equation to first-order by making a "low angle approximation." The low angle approximation means the solution better characterizes energy departing horizontally toward the receiver as opposed to energy that leaves at a launch angle, α, where the departure of $\sin \alpha$ from α makes a significant difference (see Figure 3.1 for a ray interpretation of high angle and low angle acoustic energy). The first-order equation is solved numerically by marching a single frequency solution in range and using efficient Fast Fourier Transform techniques. Broadband computations are obtained by marching solutions over an appropriate sampling of the frequency spectrum.

The standard single-frequency PE equation steps the vertical pressure field, $p(x, z)$, by way of the following relations

$$\Upsilon(x_1 + \Delta x, z) = e^{\frac{i\Omega}{2c_o}[\frac{c_o^2}{c^2(x,z)}-1]\Delta x} F^{-1}(e^{-i\frac{c_o\Delta x}{2\Omega}k^2} F(\Upsilon(x_1, z))) \tag{3.3}$$

$$p(x, z) = \frac{\Upsilon(x, z)}{\sqrt{x}} e^{i(\frac{\Omega}{c_s}x - \frac{\pi}{4})} \tag{3.4}$$

The function, $\Upsilon(x, z)$, is the envelope of the pressure field, and F and F^{-1} are the Fourier Transform and inverse Fourier Transform operators. The operator F transforms data from

depth space, z, to wavenumber space, k. The use of the symbol k is not the internal wave wavenumber, but this symbol is used as the parabolic equation wavenumber.

Just as employers of ray tracing must be concerned with the high frequency approximation, employers of the PE method must be concerned with the low angle approximation. Development of high-angle PE methods is a topic of current research [30]. Another concern of PE based implementations is the starting field, used to initiate the recursive marching equation. The most popular starting field is the *Gaussian Source*[16].

$$\Upsilon(0, z) = \sqrt{\frac{\Omega}{c_s}} e^{-\frac{1}{2}(\frac{\Omega}{c_s})^2(z-z_s)^2} \tag{3.5}$$

This initial condition is widely used in practice because of its simple analytic form. A more complex *normal mode starter* is recommended for benchmarking exercises. This starter is defined by Equation 3.1 evaluated at $x = 0$ where a normalization is executed to keep the solution from infinity.

3.4 Ray tracing

Ray tracing has been used for many decades in underwater acoustics. Snell's Law, derivable from the ray solution to the wave equation that governs the refraction of rays, dates back to 1626[16]. The ray tracing equations are derived from the wave equation by making a high acoustic frequency approximation and assuming the acoustic amplitude and phase are separable. Standard 3D ray tracing requires 6 first-order, coupled, nonlinear, ordinary differential equations. The amplitudes along the wavefront can be calculated using a ray endpoint density method (requiring no further differential equations) or using a differential equation method (requiring four additional differential equations to be integrated along with the ray equations). These methods are described in Section 3.4.2.

Low frequency ray tracing through ocean channels has only recently been addressed, and these methods focus on accounting for acoustic energy which "leaks" into the shadow zones[6] due to diffraction. The most popular method is called Gaussian beam tracing[31] and is based on the idea that a ray should be considered as a statistically varying curve with Gaussian statistics. This method is successful in accounting for acoustic leakage into

---

[6]The terms "shadow zone" and "non-ensonified region" are synonyms.

the shadow zones in a qualitative way, but does not lead to precise computations. Other techniques have been presented in the literature over the past 15 years [32][33].

In this work a 3D, low-frequency, broadband, ray tracing propagation method is developed. The remainder of this chapter focuses on this propagation method starting with the standard ray tracing equations to compute the number of arrivals and corresponding traveltimes at a down range receiver. Next, the calculation of the wavefront arrival amplitudes is addressed for 3D computational ocean models, followed by time-domain phase calculations for each arrival. These results are used to construct received acoustic waveforms. The low frequency broadband waveforms are benchmarked against a 2D range-invariant normal mode computation, serving as ground truth. This leads to promising results, and an auxiliary technique to locate wavefronts resulting from diffraction effects is developed in Section 3.6. In Section 3.7 the low frequency broadband ray tracing method is evaluated in a 2D range variant computational ocean model. Other propagation methods are compared for a study of long-range acoustic propagation through internal-wave fields. Also in Section 3.7, the 3D, low-frequency, broadband propagation method is discussed. This method has the absolute advantage of simulating complete 3D time-varying propagation. Rays are traced independent of the source spectrum and the procedure does not need to be repeated for each frequency, reducing low-frequency long-range computation time by factors of two to three orders of magnitude over normal mode and PE based propagation methods.

3.4.1 Ray tracing equations: number of arrivals and traveltimes

The ray solution to the wave equation leads to a computationally efficient propagation method. Rays are launched from the source location at different initial trajectories defined by the launch angles α_o and ψ_o, the ray inclination and ray azimuth angle at the source, respectively. Figure 3.3 shows the rectangular coordinate system employed. x denotes the range coordinate, y denotes the transverse coordinate, and z (positive downward) denotes the depth coordinate. A single ray is drawn and the launch angles are indicated.

The ray path propagated through a 3D computational ocean model is determined through the numerical integration of 6 coupled, non-linear, ordinary differential equations.
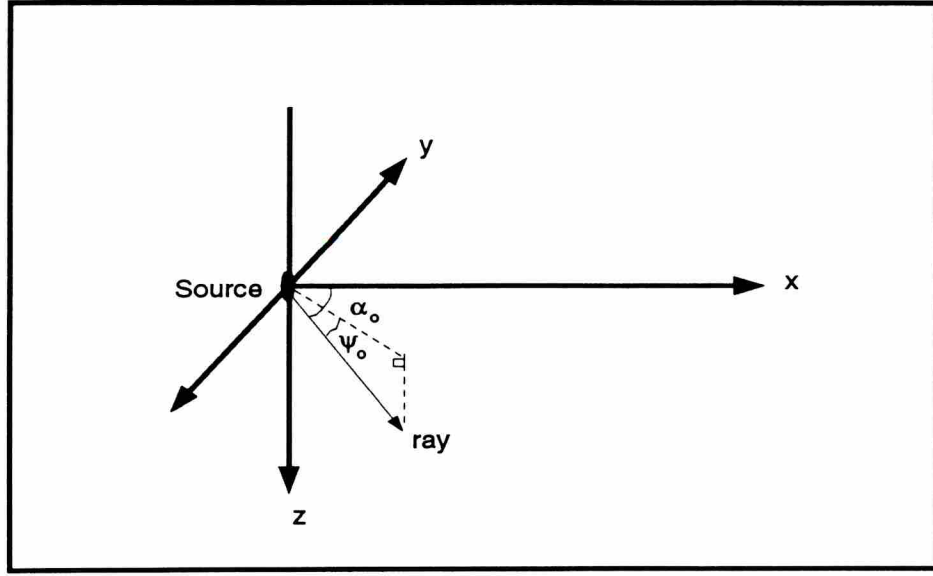
Figure 3.3: The rectangular coordinate system is shown. The coordinate x denotes the range and is in the nominal acoustic direction. The coordinate y denotes the transverse coordinate typically not included in long range acoustic modeling. The coordinate z is positive downward and indicates depth. Rays are launched from the source with initial launch angles defined by inclination and azimuth angles α and ψ respectively.

These standard ray tracing equations are defined in Equations 3.6 - 3.11.

$$\frac{dt}{dx} = \frac{1}{c^2 A} \tag{3.6}$$

$$\frac{dz}{dx} = \frac{B}{A} \tag{3.7}$$

$$\frac{dy}{dx} = \frac{D}{A} \tag{3.8}$$

$$\frac{dA}{dx} = -\frac{1}{c}\frac{\partial c}{\partial x}\frac{dt}{dx} \tag{3.9}$$

$$\frac{dB}{dx} = -\frac{1}{c}\frac{\partial c}{\partial z}\frac{dt}{dx} \tag{3.10}$$

$$\frac{dD}{dx} = -\frac{1}{c}\frac{\partial c}{\partial y}\frac{dt}{dx} \tag{3.11}$$

The initial conditions are the source location, (x_o, y_o, z_o), the transmission time t_o, and initial auxiliary parameters defined in Equations 3.12 - 3.14.

$$A_o = \frac{\cos \alpha_o \cos \psi_o}{c_s} \tag{3.12}$$

33

$$B_o = \frac{\sin \alpha_o}{c_s} \qquad (3.13)$$

$$D_o = \frac{\cos \alpha_o \sin \psi_o}{c_s} \qquad (3.14)$$

The sound speed, $c(x, y, z, t)$ is denoted by c, and the sound speed at the source at the time of transmission is denoted c_s. Commonly, the source is located on the sound channel axis so that c_s is set to c_o. The auxiliary parameter A tracks the quantity $\frac{\cos \alpha \cos \psi}{c}$. This value is strictly positive and division by this quantity does not lead to numerical instabilities in the ray computations. The angles α and ψ denote the ray inclination and azimuth along the ray path. The ray tracing equations are derived from the wave equation in Appendix B.

The equations are numerically integrated using a 4th order Runge-Kutta integration routine[22], and a 5-tap finite impulse response (FIR) spatial filter is used to approximate the partial derivatives[23]. The independent variable is range for the equations presented. They can easily be manipulated such that the independent variable is time. Both fixed step-size and adaptive step size algorithms were used to execute the numerical integration.

The number of rays that connect the source and receiver (termed eigenrays) determine the number of totally refracted wavefront arrivals. The corresponding traveltimes are directly computed from integration of time along the ray path. The ray inclination, α, evaluated at the receiver represents the angle of arrival of a wavefront and can be computed from the auxiliary parameter B at the receiver

$$\alpha = \sin^{-1} cB \qquad (3.15)$$

3.4.2 Amplitude computations

The amplitude of the acoustic waveform along each ray can be calculated using two methods: a differential equation method and a ray end point density method. The differential equation method is introduced for 3D computations, and the ray endpoint density method is developed.

34

Differential equation method

The differential equation method is based on tracking the height and width of the cross sectional area of an imaginary ray tube about the ray path. An intuitive description is developed here, and the derivation is contained in Appendix B. Four first-order, coupled, ordinary differential equations are needed to track these parameters. The cross section of the ray tube is taken along the wavefront. The wavefront is perpendicular to the ray trajectory and these three orthogonal components (r along the ray path, w along the wavefront, and y) compose a 3D ray centered coordinate system. The relation between the ray centered coordinate system (r, w, y) and the 3D rectangular coordinate system (x, y, z) is through α the current ray inclination as described by Equations 3.16 and 3.17 and shown in Figure 3.4. For long range propagation only rays with azimuth launch angles, ψ_o near 0° need to be considered and it is assumed that $\psi = 0°$ for the derivation of this amplitude calculation method (detailed in Appendix B).

$$x = r \cos \alpha - w \sin \alpha \tag{3.16}$$

$$z = r \sin \alpha + w \cos \alpha \tag{3.17}$$

$$y = y \tag{3.18}$$

The ray tube is constructed such that constant power is maintained over the cross sectional area along the wavefront; thus, the cross sectional area is inversely proportional to the average intensity of the acoustic waveform. Intensity, I, is a measure of the rate of energy flow (power, $\wp$) through a unit area, ΔA, perpendicular to the direction of wave propagation[7].

$$I = \wp / \Delta A \tag{3.19}$$

This cross sectional area, ΔA, is monitored by its height along the wavefront coordinate, w, and width measured along the transverse coordinate, y, using the symbols q and v respectively such that $\Delta A = qv$. These parameters are labeled in Figure 3.5 where the concept of a ray tube is illustrated.

---

[7]A single plane wave is assumed.
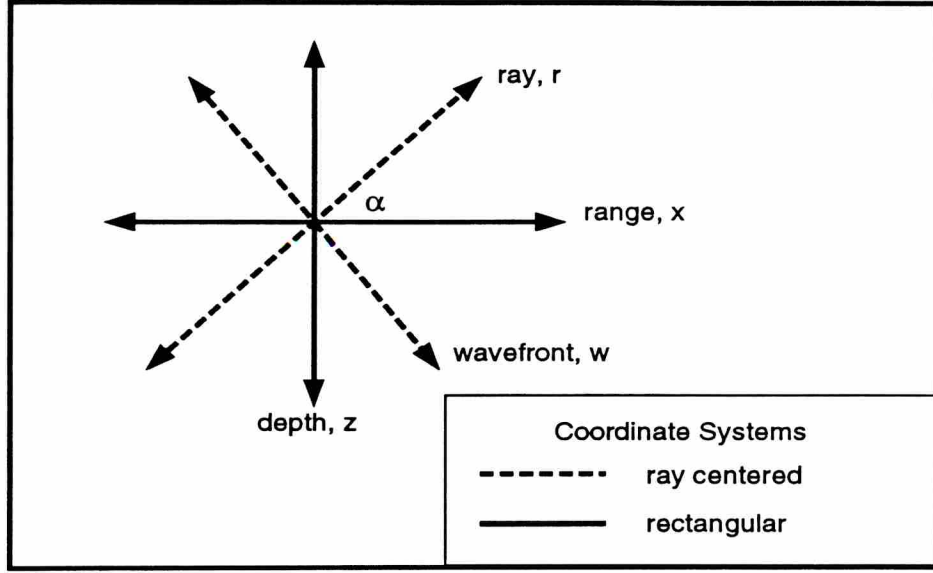
Figure 3.4: The ray centered coordinate system is shown in two dimensions. The current ray inclination angle, α, defines the relation between the ray centered and rectangular coordinate systems.

For a 2D computational ocean model only two additional differential equations are required to track the height of the ray tube, q. The width of the ray tube is equivalent to the propagation range. The differential equations for the 2D case are derived in [31], and have been modified to agree with the coordinate system and independent integration variable used in this treatment. The two differential equations required to compute q along the ray are

$$\frac{dq}{dx} = \frac{s}{A} \tag{3.20}$$

$$\frac{ds}{dx} = \frac{-q}{Ac^3}\frac{\partial^2 c}{\partial w^2} \tag{3.21}$$

The initial conditions are $s_o = 1/c_o$ and $q_o = 0$. The s parameter is updated proportional to the curvature of the sound speed field along the wavefront coordinate w and determines whether the local acoustic rays diverge ($\frac{\partial^2 c}{\partial w^2} > 0$) or converge ($\frac{\partial^2 c}{\partial w^2} < 0$) to yield an increase or decrease in acoustic power, respectively. By iteratively applying the chain rule to construct a change of coordinates we find

$$\frac{\partial^2 c}{\partial w^2} = c^2(\frac{\partial^2 c}{\partial x^2}B^2 + 2\frac{\partial^2 c}{\partial x \partial z}AB + \frac{\partial^2 c}{\partial z^2}A^2) \tag{3.22}$$

36
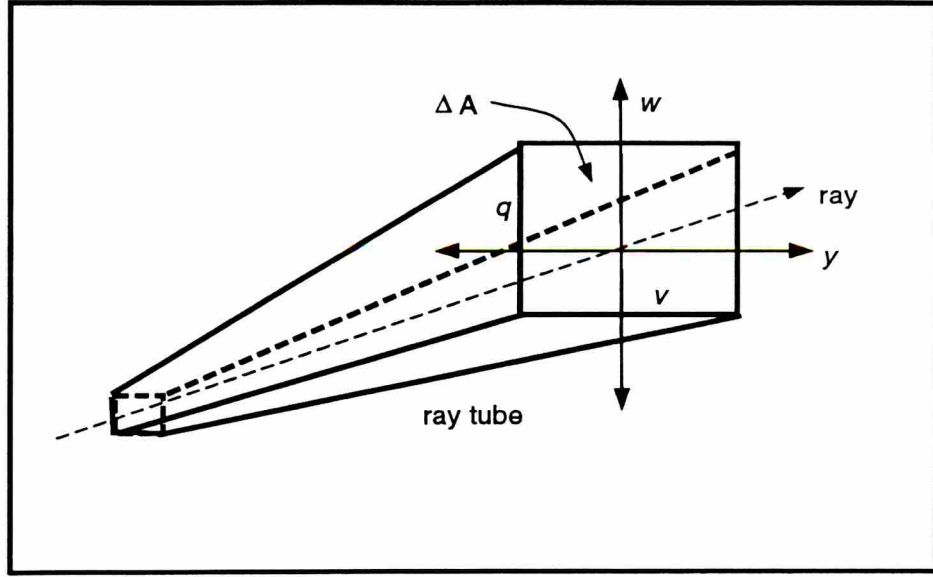
Figure 3.5: **The ray tube with cross sectional area** ΔA **drawn in the ray centered coordinate system. The values** q **and** v **denote the height and width of the ray tube and are used to compute the acoustic amplitude along the front.**

so that

$$\frac{ds}{dx} = \frac{-q}{Ac}\left(\frac{\partial^2 c}{\partial x^2}B^2 + 2\frac{\partial^2 c}{\partial x \partial z}AB + \frac{\partial^2 c}{\partial z^2}A^2\right) \tag{3.23}$$

Extending this method to three dimensions, the two differential equations required to track the width of the ray tube are

$$\frac{dv}{dx} = \frac{u}{A} \tag{3.24}$$

$$\frac{du}{dx} = \frac{-v}{Ac^3}\frac{\partial^2 c}{\partial y^2} \tag{3.25}$$

The initial conditions are $u_o = 1/c_o$ and $v_o = 0$. The sound speed curvature along the orthogonal coordinate, y, is monitored to track the width of the ray tube. These equations are derived in Appendix B.

These equations are directly implementable using a Runge-Kutta integration routine. The second-order partial derivatives are computed using a 5-tap FIR spatial filter. To obtain the compact form for Equations 3.24 and 3.25, it was assumed the ray is traveling in the nominal acoustic plane and that the ray tube does not rotate.

The acoustic intensity of the wavefront at a downfield location is proportional to $1/qv$,

37

and the acoustic amplitude is proportional to $1/\sqrt{qv}$. If the the sound speed gradient in the y direction equals zero, then v is equivalent to the range and is consistent with cylindrical spreading.

Ray endpoint density method

The ray endpoint density method to compute the amplitude is based on tracing a large number of rays closely and uniformly spaced in launch angles. The density of the ray endpoints at some down range receiver location can be used to calculate the received acoustic amplitude. By launching a quiver of rays separated by small angles $\Delta\alpha_o$ and $\Delta\psi_o$, the
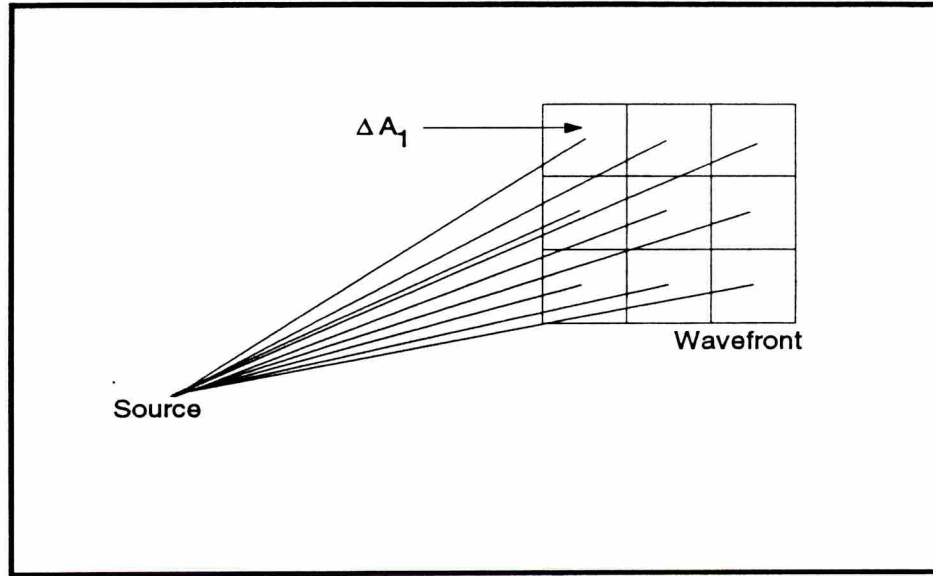
Figure 3.6: A set of rays are propagated 1 meter from the source. The rays are uniformly spaced in launch angle by $\Delta\alpha_o$ and $\Delta\psi_o$ in inclination and azimuth respectively. Each ray represents an equal area of the wavefront and an equal power contribution to the acoustic waveform.

wavefront area associated with each ray 1 meter from the source is

$$\Delta A_1 = \Delta\alpha_o\Delta\psi_o \qquad (3.26)$$

where ΔA_1 is in units m^2 and the angles are measured in radians. This is sketched in Figure 3.6. Each ray represents an equal power contribution to the wavefront. The effective cross sectional area of a given ray down range, denoted ΔA_2, will contribute equal power across

this area such that we have the relation through a conservation of power

$$I_1 \Delta A_1 = I_2 \Delta A_2 \tag{3.27}$$

where I_1 and I_2 indicate the average intensity at the two points along the ray. The construct is analogous to that of a ray tube and a similar diagram is shown in Figure 3.7. The cross
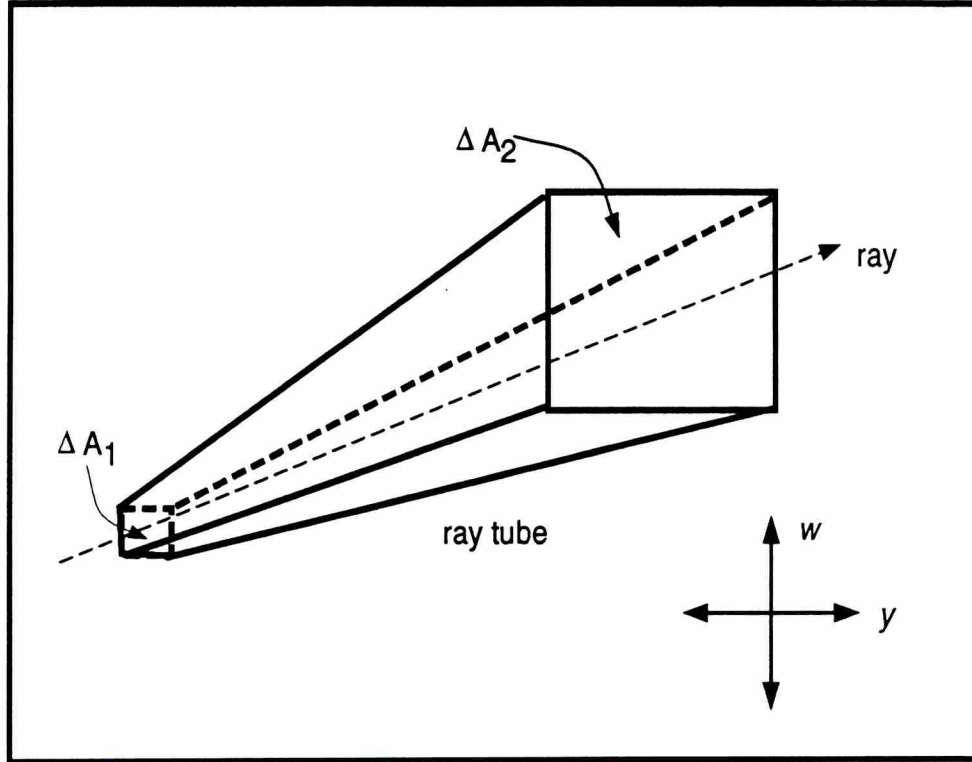
Figure 3.7: **The ray tube is redrawn to describe the ray endpoint density method. This method is based on the cross sectional area a single ray represents along the wavefront as the acoustic ray propagates down range.**

sectional area ΔA_2 is computed by counting the number of ray endpoints which land within an observational area A_{obs} centered at the receiver location.

$$\Delta A_2 = A_{obs}/N \tag{3.28}$$

where N is the ray endpoint count within the observation area. Thus, ΔA_2 represents the effective cross sectional area of a single ray's tube at the receiver point. From Equations

3.26, 3.27, and 3.28 the ratio of intensities is

$$\frac{I_2}{I_1} = \frac{\Delta A_1}{\Delta A_2} = N \frac{\Delta \alpha_o \, \Delta \psi_o}{A_{obs}} \tag{3.29}$$

The acoustic amplitude relative to the amplitude one meter from the source is simply the square root of Equation 3.29

$$a = \sqrt{N \frac{\Delta \alpha_o \, \Delta \psi_o}{A_{obs}}} \tag{3.30}$$

To obtain a more local estimate, a two-dimensional Gaussian window centered on the receiver location can be applied to the ray endpoint counts to weight their distance from the actual receiver location. In summary, the amplitude of a received wavefront can be calculated by estimating the ray endpoint density about the receiver point. This is accomplished by propagating a large number of rays uniformly and closely spaced in launch angles. To guarantee sufficient accuracy, the density of the rays at the source is increased until the computed power across the wavefront converges.

In Chapter 4, it will be of interest to calculate the change in received power due to the presence of an internal wave field filling the propagation path. The ratio of the received power with the internal wave field present and the internal wave field not present is equivalent to the ratio of the ray endpoint counts within an equivalent observation area for the two cases. By transmitting a set of rays that could potentially contribute to the down range arrival, the change in power across the entire front can be efficiently computed by simply taking this ratio at any hypothesized receiver location. For a given area, the ratio of received acoustic power and received acoustic intensity are equal.

There are advantages to each amplitude calculation method. The differential equation method is an infinite acoustic frequency calculation. The ray tube cross sectional area can vanish yielding an infinite received acoustic intensity. The ray endpoint density method is based on a finite frequency interpretation of the infinite frequency ray tracing computations. Through an implicit spatial averaging the ray endpoint density estimate does not yield infinite intensity computations at a caustic; moreover, a significant advantage of the ray endpoint density method is that it can be tuned to underestimate amplitude gains at caustics, the point where the differential equation method predicts infinite amplitudes. In Chapter 4, the results of acoustic propagation through internal wave fields show great

amplitude fluctuation of the received waveform using the ray endpoint density amplitude calculation, since the ray endpoint density method conservatively evaluates amplitude fluctuations it is an appropriate technique to use. If the differential equation method were used, large amplitude fluctuations could be attributed to errors in the amplitude computation method.

When the amplitude is calculated away from a caustic, the two methods yield essentially identical results. The differences in the amplitude computations using the two techniques has been experimentally determined to be less than 1 percent or less than a tenth of a dB.

3.4.3 Time-domain phase computations

The received time-domain phase associated with a given wavefront arrival is a function of the traveltime and number of caustic interactions. The traveltime for each ray path is directly computed from the standard ray tracing equations by integration of Equation 3.6.

Consider the differential equation interpretation of computing the acoustic amplitude. The cross sectional area of the ray tube becomes zero when the ray crosses at a caustic. At this point, the amplitude is computed as infinite and is a well documented problem with infinite-frequency acoustic amplitude computations. At the caustic point, the acoustic phase advances by 90°. Intuitively, the ray-tube cross sectional area is proportional to the reciprocal of the acoustic intensity along the ray. At a caustic, the ray tube area experiences a sign change as the height or width of the ray tube crosses through zero. Since the acoustic pressure is proportional to the square root of the intensity, propagation through a caustic relates to a $\sqrt{-1}$ change in acoustic pressure or equivalently a 90° change in phase. This has been proven formally in [34]. What is interesting to note in this work is that caustics can also occur due to a sound speed gradient in the transverse direction, allowing the width of the ray tube to experience a zero crossing. The number of these caustics can be tallied using the differential equation amplitude calculation method since encountering a caustic corresponds to q or v passing through zero (changing sign).

The time-domain phase of a single wavefront arrival may change over consecutive acoustic transmissions. Recall, the acoustic signal is transmitted periodically with a period equal to an integer number of carrier cycles. If a time-invariant computational ocean model is em-

41

ployed, the time-domain phase of a single wavefront arrival will remain precisely constant. This likely is the case for a time-varying computational ocean model. The period-to-period change in time-domain phase is computed by calculating the time-difference-of-arrival of the wavefront over consecutive transmissions. The change in acoustic traveltime (seconds) is mapped to a change in phase (cycles) through the center frequency, f_c by

$$\Delta\phi = \Delta\tau / f_c \qquad (3.31)$$

By tracking the wavefront using the differential equation method for amplitude calculation, the total number of caustics encountered along the propagation path can be monitored. If this number changes between transmissions, the time-domain phase can be advanced or retarded by the appropriate number of quarter cycles. Please note that these phase changes do not result in a change in traveltime, only a change in phase. This means that a change in phase may not always relate to a change in traveltime and using changes in time-domain phase as a precise measure of a change in traveltime may not be appropriate as discussed in Chapter 1. If this is the case, traveltime measurements should be based on the peak of the envelope of a resolved pulse reception since this measurement is independent of the caustic phase.

3.4.4   Waveform construction

Waveforms are constructed by coherently summing the received wavefront arrivals at a down range source. The number of arrivals and their traveltimes at any range and depth are easily extracted from ray tracing results, as long as rays can be constructed to the point of interest. The received acoustic waveforms are created by constructing a baseband complex pulse at each ray-tracing arrival time. The phase of the pulse is the sum of the traveltime delay and the caustic phase. A received waveform is constructed as a coherent summation of arrivals.

As an example, the source and receiver are located on the sound channel axis at a depth of 800 m and separated by 500 km. A range-invariant 2D computational ocean model is used as described by $c_{S89}(z)$ in Chapter 2. Rays are traced for the 500 km distance. The ray endpoints are connected to form a measurement front. $h_{z_o=800m,x_o=0m}(z,t \mid x = 500km)$. The measurement front is shown at the top of Figure 3.8. For a given depth, the number of
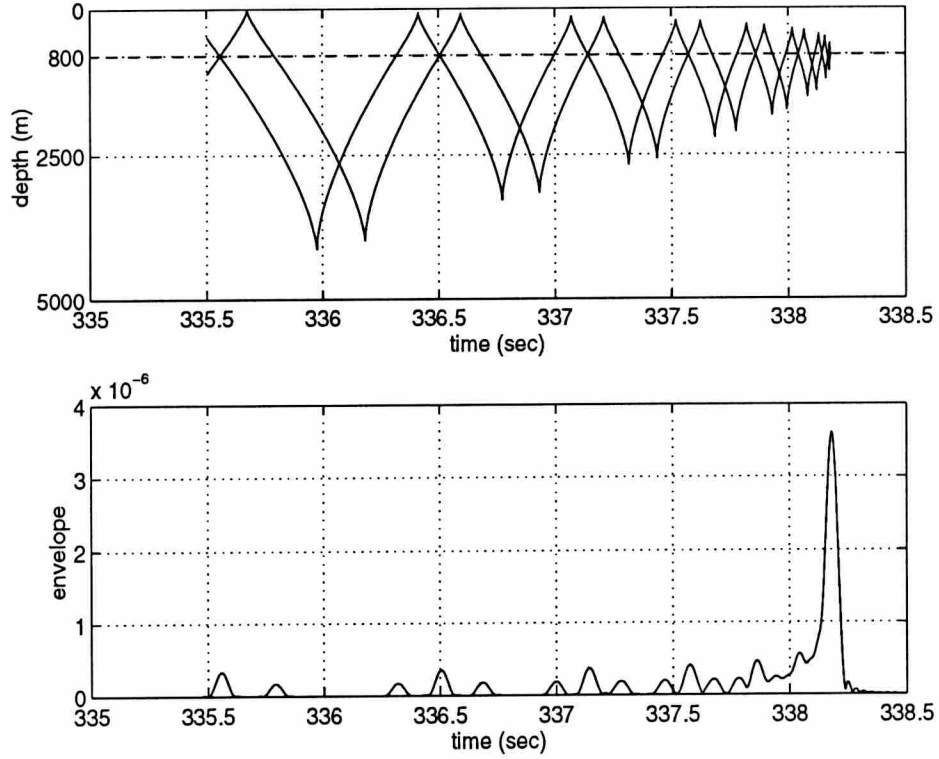
Figure 3.8: The top figure shows the measurement front after 500 km of propagation through a deep ocean sound speed profile with the source on the sound channel axis, 800 meters deep. The number of arrivals and the corresponding traveltimes can be determined for a receiver at any depth. The intersection of the dashed line and the measurement front define the arrival traveltimes for a 800 meter deep receiver. The bottom figure shows the envelope of the 800 meter deep reception.

arrivals, N, and their traveltimes, τ_n, are directly obtained. The amplitude of each arrival, a_n, was computed using both the differential equation and ray endpoint density methods yielding equivalent results. The source is spectrally centered at 75 hz and is sinc-shaped with nulls at 60 and 90 hz and was defined in Equation 1.2. There are $N = 32$ arrivals for a receiver depth of 800 m.

The number of sign changes of the q parameter from Equation 3.20 is tallied along the ray path for each arrival. This number is denoted by ς_n, and the caustic phase for the nth received signal is $\varsigma_n/4$ cycles. The ray-tracing constructed complex baseband time-domain

waveform is

$$p_{ray}(t) = \sum_{n=1}^{N} a_n s(t - \tau_n) e^{i\varsigma_n \pi/2} \tag{3.32}$$

which is the convolution of the time-domain source signal and the phone impulse response. Equation 3.32 represents the summation of pulses arriving without dispersion along each of the eigenray paths. The time-domain pulses, $s(t - \tau_n)$, are complex valued, and $p_{ray}(t)$ represents a model of a complex demodulated acoustic reception. It is easier to construct the waveform in the frequency domain using the real baseband signal spectrum $\tilde{S}(f)$, the baseband equivalent of the passband spectrum $S(f)$. The corresponding baseband frequency-domain description is

$$P_{ray}(f) = \sum_{n=1}^{N} a_n \tilde{S}(f) e^{-i2\pi(f+f_c)\tau_n} e^{i\varsigma_n \pi/2} \tag{3.33}$$

The envelope of the received waveform is shown in the bottom of Figure 3.8. The early wavefront arrivals are resolved while the terminal section is composed of many unresolved wavefront arrivals. It is typical for long range acoustic receptions to begin with relatively weak wavefront arrivals and build to a relatively loud terminal arrival known as the *crescendo*.

The amplitudes of the thirty-two arrivals were calculated by both the differential equation method and the ray endpoint density method. These methods yield nearly identical results for this reception, deviating less than 0.02 dB for any arrival amplitude computation. The only time these results differ is where the receiver is located within meters of a caustic, when the differential equation based method will yield erroneously large amplitude results.

3.5 2D range invariant benchmarking

For long-range acoustic propagation through the deep ocean channel, it is demonstrated that ray methods yield essentially identical arrival structures and sound-field amplitudes as the normal mode (ground truth) propagation method.

Benchmarking propagation methods against the normal mode solution to the wave equation for range-invariant cases is a critical step to acoustic modeling. Range invariant benchmarking exercises compare the envelope and phase of the computed received waveform from different propagation methods at a specified transmitter/receiver geometry and source signal.

3.5.1 Ray tracing benchmarking
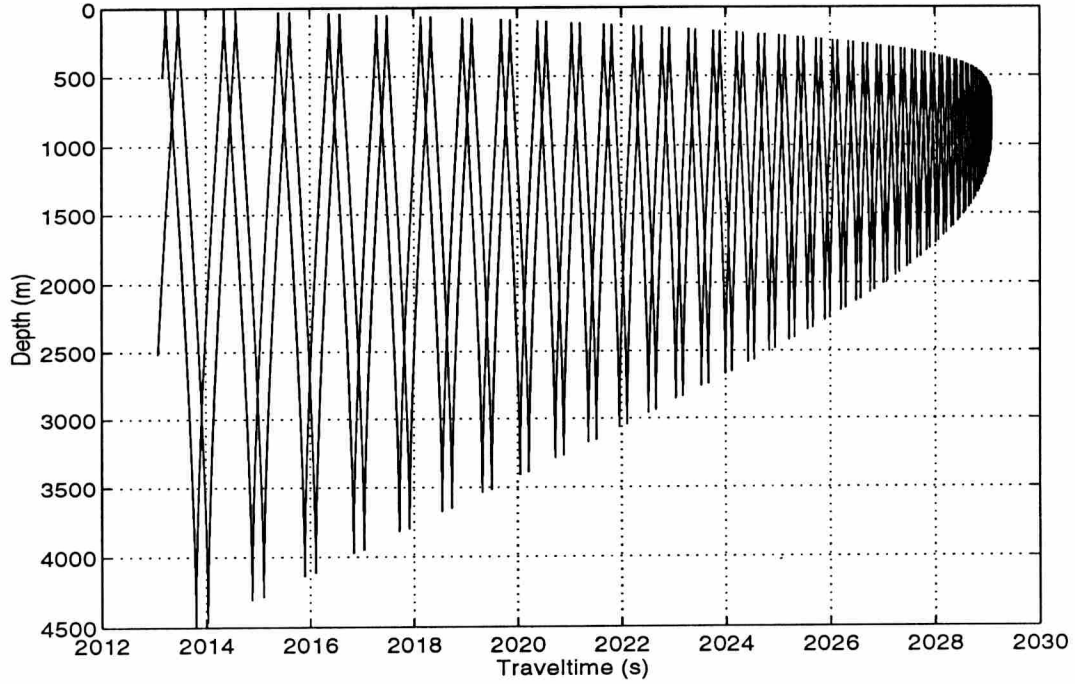
Figure 3.9: A measurement front after 3 Mm of propagation through a deep ocean sound speed profile. The source is located on the sound channel axis, 800 meters deep.

A single benchmarking scenario is illustrated to demonstrate the general results. The range-invariant computational ocean model is described by the sound-speed profile, $c_{S89}(z)$, which is defined in Chapter 2. The source is located on the sound channel axis, $z_s = 800$ m. The receivers are located at a range of 3 Mm. The source signal is low frequency and broadband and is described in Equation 1.2. The simulation sampling rate is 240 Hz, and the signal will consist of 4096 samples allowing the simulated time-domain waveform to cover over 17 seconds.

The envelopes of the low-frequency broadband ray and normal-mode constructed waveforms are plotted in Figure 3.10. The receiver depth is 800 m. The ray constructed waveform is composed of 171 arrivals and spans 15 seconds. Both the differential equation and ray endpoint density amplitude calculation methods yield essentially identical results. In comparing the 171 amplitude calculations using the two methods, the computed amplitudes do not differ by more than 0.05 dB, where the maximum and minimum amplitudes computed

45
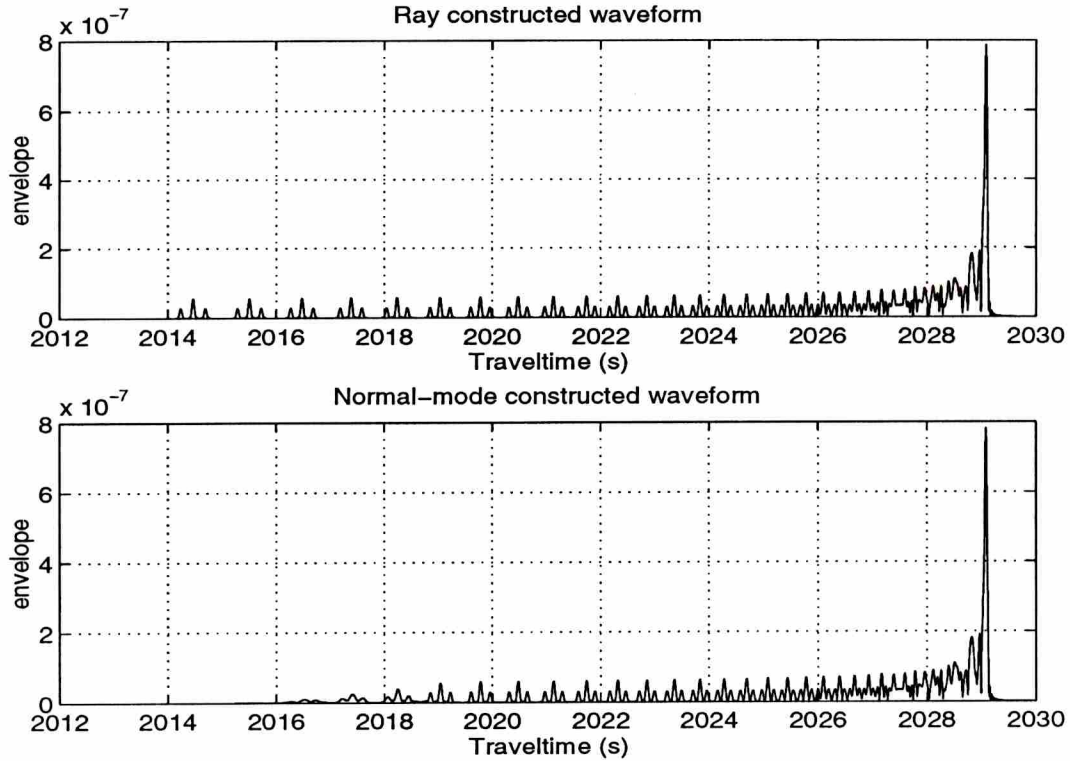
Figure 3.10: The top figure shows the envelope of the simulated acoustic reception at a depth of 800 meters using the ray propagation method. The bottom figure shows the envelope of the simulated acoustic reception at a depth of 800 meters using the normal mode propagation method.

using either method differ by more than 26 dB. Returning to Figure 3.10, the normal-mode and ray waveform envelopes are very similar. Only 65 normal-modes were used, and the earliest arrivals are not present in the normal-mode constructed waveform because the higher (not included) normal modes have faster group velocities, arrive earlier, and construct the early wavefront arrivals.

Taking a close look at the crescendo in Figure 3.11, the waveform envelopes are essentially exact. The ray constructed waveform is plotted using a solid line, and the normal-mode constructed waveform is plotted using a dashed line. The envelope match is absolute. The waveforms were not normalized. The arrivals in this section are unresolved. The individual ray-arrival phases are critical in determining the envelope shape. If the caustic phase were not added to each arrival, the ray constructed waveform envelope would not be

46

similar to the normal-mode constructed waveform.
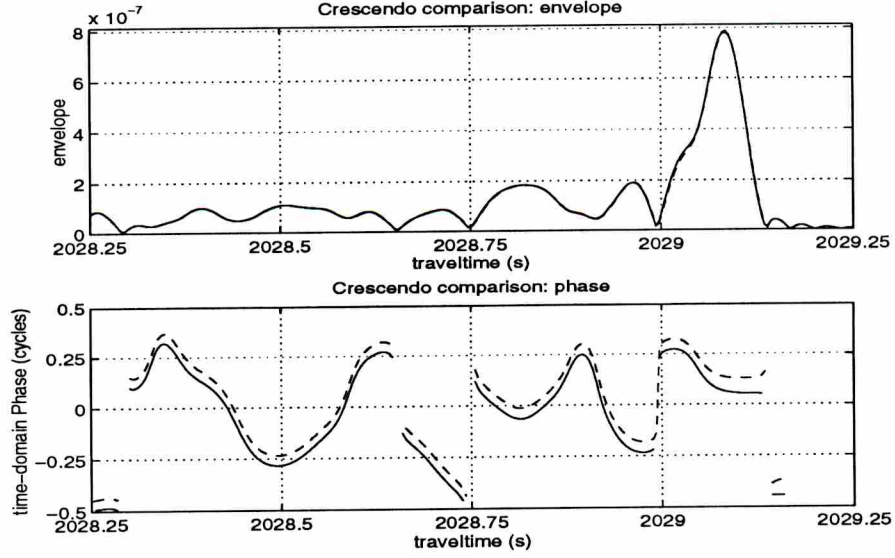
Figure 3.11: **The top figure shows the envelopes of the ray constructed waveform (solid) and normal mode constructed waveform (dashed) for the last second of the reception, crescendo. The two envelopes are essentially identical. The bottom figure shows the time-domain phase of the ray constructed waveform (solid) and normal mode constructed waveform (dashed).**

The phase comparison in the bottom plot of Figure 3.11 shows that the time-domain phases are very similar. The absolute phase differs by 0.03 cycles or 0.4 ms. This is within the expected tolerance of the computations. This small phase error decreases with shorter range propagation.

In Figure 3.12 the middle section of the arrival is investigated. The same dashed/solid convention is used to identify the curves. The waveform envelopes are essentially identical. The amplitudes assigned to the individual arrivals using the ray endpoint density and differential equation methods are in excellent agreement with the normal-mode solution. Arrivals are unresolved after $t = 2027.25$ seconds. The absolute time-domain phase comparison shows the same bias as seen in Figure 3.11, suggesting that the phase (traveltime) difference is predominantly independent of launch angle.

In Figure 3.13 the early section of the arrival is shown. This is the only section of the arrival where the envelopes significantly differ. This is due to the number of normal

47
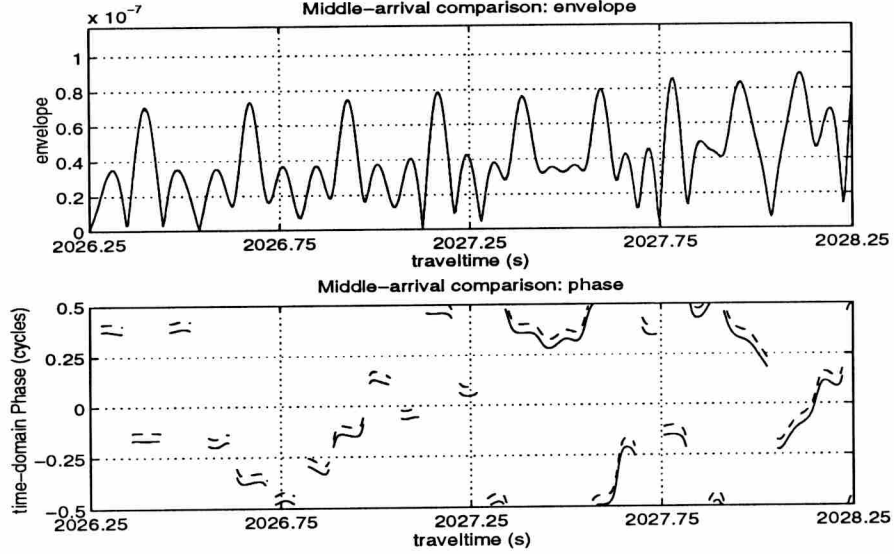
Figure 3.12: **The top figure shows the envelopes of the ray constructed waveform (solid) and normal mode constructed waveform (dashed) for a middle section of the reception. The two envelopes are essentially identical. The bottom figure shows the time-domain phase of the ray constructed waveform (solid) and normal mode constructed waveform (dashed).**

modes included in the normal-mode constructed arrival (dashed line). Sixty-five modes were included. The time-domain phase of the normal-mode constructed waveform is not constant under a pulse but becomes flat as the amplitudes match the ray waveform at $t = 2018.75$ seconds, indicating 65 modes are adequate thereafter.

For this example, 120,000 normal modes are required ($M = 200$ modes each at 60 frequencies based on a 0.5 Hz sampling of the 30 Hz wide broadband source) to accurately represent the complete arrival structure [8]. The arrival is equivalently represented by 171 ray arrivals, albeit 30,000 rays were traced to construct the measurement front. The normal-mode constructed and ray-constructed waveforms are identical for the pre-crescendo arrivals. Thus, ray and mode methods should be seen as complementary. Only a relatively few modes are required to construct the crescendo portion of the arrival where the rays are highly unresolved. Also, only a relatively few rays (and many modes) are required to construct

---

[8] Normal modes greater than $M = 200$ will interact with the ocean surface and/or bottom and are assumed to not travel long ranges without being catastrophically attenuated.
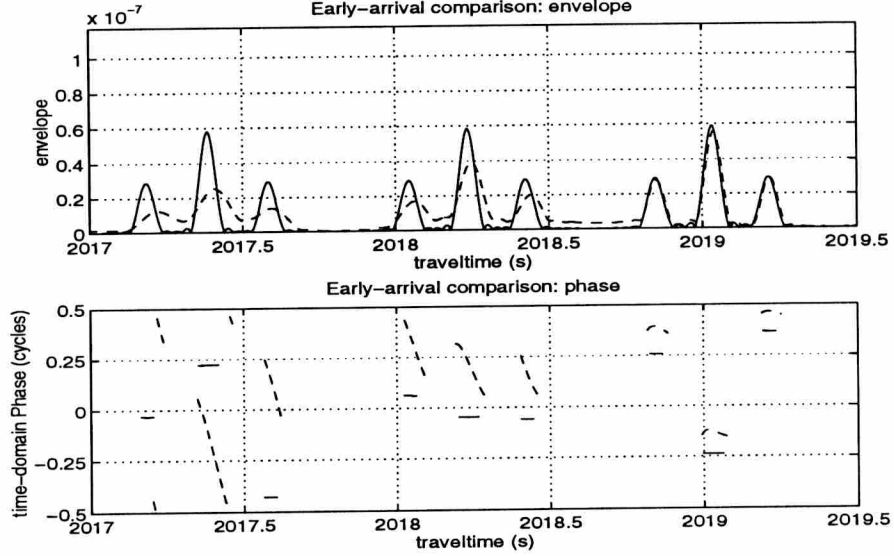
Figure 3.13: The top figure shows the envelopes of the ray constructed waveform (dashed) and normal mode constructed waveform (solid) for the early part of the reception. The two envelopes differ because an insufficient number of normal modes was included in the modeling. The bottom figure shows the time-domain phase of the ray constructed waveform (solid) and normal mode constructed waveform (dashed). The disagreement is due to the insufficient number of normal modes included in the modeling

the pre-crescendo arrival structure.

These comparisons have been repeated at many source and receiver depths for several range-invariant sound speed profiles. The results are similar to the set presented with one class of exceptions. For off-axis source or receiver, since diffraction effects are not included in the ray-tracing solution, as much as the last 0.2 seconds of the crescendo constructed using each method do not accurately match. However, prior to this last section of the crescendo, the waveforms accurately match, including throughout times when the ray arrivals are unresolved. For the case demonstrated, the receiver is not *near* any caustics and effects from diffraction are not significant. There are many corrections one can apply to ray tracing results: beam displacement, Gaussian beams, caustic/shadow zone corrections, and diffracted rays[35]. None were applied for this comparison. In Section 3.6 a method to include all diffracted wavefronts is developed. Prior, the PE propagation method is

49

benchmarked against the normal mode method for this range-invariant case.

3.5.2 PE benchmarking

The PE propagation method has enjoyed a rather unchecked wave of popularity for low frequency acoustic propagation studies. The *standard* PE method has been the primary algorithm used by researchers to implement a PE based propagation method prior to 1990. Improvements on the standard method remains a topic of current research, and many improvements in accuracy have been achieved at the expense of computation time. In this section, through a range-invariant benchmarking exercise, it is highlighted why the standard PE propagation method is not suitable for a deterministic analysis of long range acoustic propagation.
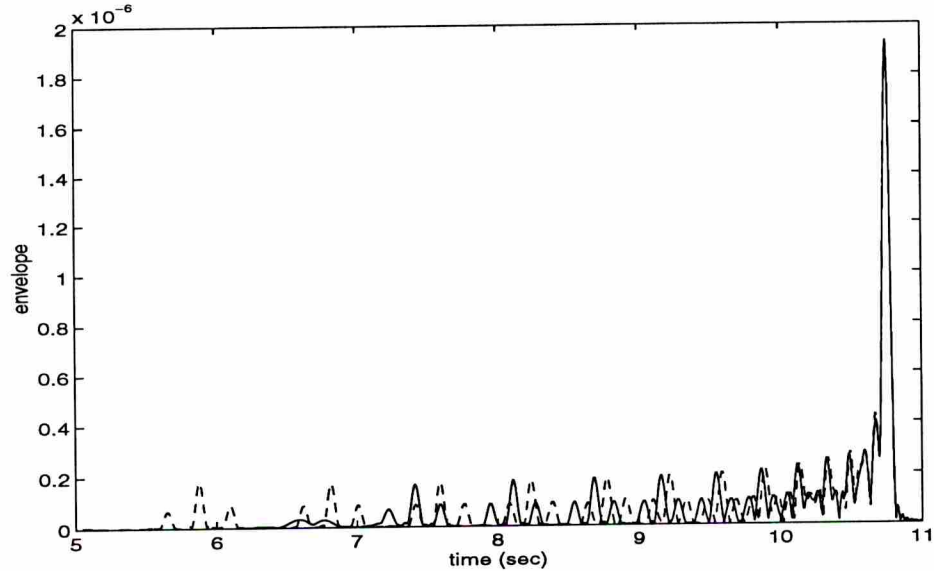
Figure 3.14: The figure shows the normal mode (solid) and PE (dashed) constructed waveform envelopes for an axial reception after 1 Mm propagation through a deep ocean sound speed profile.

A similar model is used as with the ray tracing benchmarking example. The same 2D computational ocean model, $c_{S89}(z)$, was used, and the source and receiver were located on the sound channel axis. The only difference is that in this case, the range is reduced from 3 Mm to 1 Mm. The same acoustic signal is used as described in Equation 1.2. The envelopes of the normal mode constructed waveform (solid line) and the PE constructed
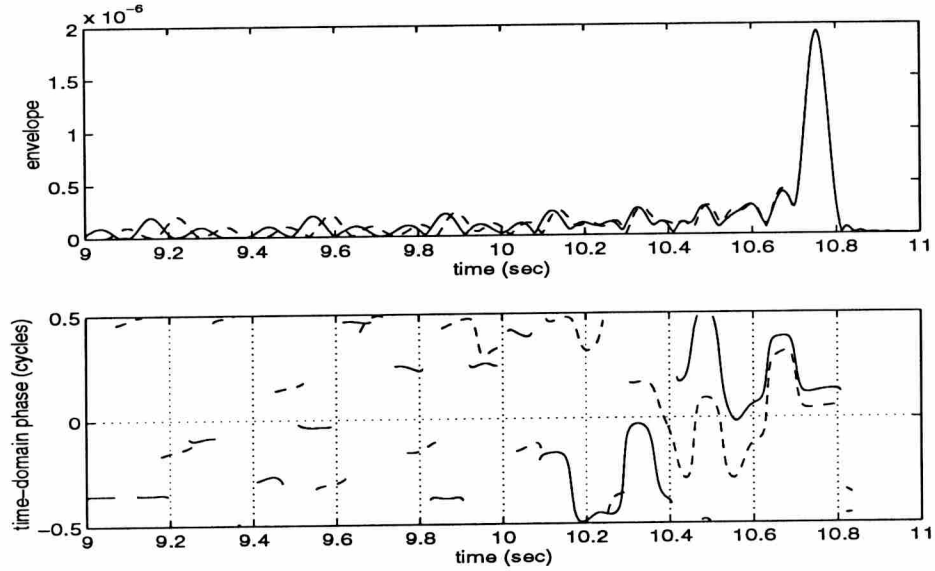
Figure 3.15: The top figure shows the normal mode constructed waveform envelope (solid) and the PE constructed waveform (dashed) for the last two seconds of the reception. The envelopes are in agreement throughout the crescendo where the PE low angle approximation is adequate. The earlier arrivals, corresponding to high angle ray arrivals, is not accurately modeled using the standard PE propagation method. The bottom figure shows the time-domain phase for the normal mode (solid) and PE (dashed) constructed waveforms. The agreement is best near the crescendo.

waveform are shown in Figure 3.14. The normal mode constructed waveform can fairly be considered as ground truth after the 8.0 second time mark based on the limited number of normal modes included. The early arriving (high angle) wavefronts show a significant difference in arrival time. This significant error for long-range deep ocean propagation has been reported in [36]. It is clear that the high-frequency approximation for ray tracing is not nearly as critical as the low-angle approximation for the PE propagation method for the scenario evaluated.

In Figure 3.15, the time-domain envelope and phase of the waveforms are shown for the last two seconds. The envelope match is good for the terminal arrivals. These correspond to the low-angle rays and fit well within the low-angle assumption to form the standard PE recursion. The time-domain phase differs only slightly near the terminal arrival, but varies

significantly with earlier arrivals. The obvious arrival time discrepancies in the envelope comparison reflect a traveltime induced time-domain phase discrepancy.

The discrepancy in both the time-domain envelope and phase of the acoustic arrival compared against the ground truth solution increases with transmitter receiver separation. Additional traveltime (a waveform shift to the right along the time axis) corresponds to a decrease in time-domain phase. Although the standard PE propagation method is termed a "fast" solution to the wave equation, run times are 100 to 1000 times longer than for the ray propagation method for the cases studied by the author. Since the ray method computes the ray paths and amplitudes independent of the source spectrum, significant computations are saved for simulation of broadband acoustic propagation. Along with the computational savings, the ray tracing propagation method is more accurate for long range deep ocean propagation. In all of the simulations, the step sizes to integrate the differential equations were decreased until there was no longer a change in the final computations[9].

The PE propagation method can not fully incorporate a time-varying computational ocean model. The sound speed field must be frozen as the acoustic signal propagates through the medium. A larger disadvantage is that the PE propagation method suffers a significant increase in computation time and memory requirements to move to a 3D computational ocean model.

Since we are ultimately interested in a deterministic analysis on the acoustic propagation through the ocean model, based on the benchmarking results and with the computing power available, we move to use of the ray tracing propagation method.

For the low frequency, broadband acoustic signals of interest the high-frequency approximation is reasonably met; however, ray tracing equations do not incorporate diffracted energy. The next section develops a method to model diffracted wavefronts.

3.6 Diffracted wavefronts

Two extensions of standard ray tracing to match full-wave normal-mode computations for acoustic propagation through a range-invariant sound-speed profile are described. A

---

[9]Even though the PE propagation method yields inaccurate results for the early acoustic arrivals, the method does converge to a stable solution as the numerical step size is decreased.

52

received acoustic waveform can be described solely in terms of refracted and diffracted wavefront arrivals. Previous ray modeling in this dissertation has addressed only refracted arrivals which make up the vast majority of the received acoustic energy. The first extension of standard ray tracing is well known to researchers in the field of ocean acoustic propagation. A diffracted wavefront in the shadow zone is modeled as a wavefront. However it is necessary to review this work to present the second extension to standard ray tracing. **The well-known diffracted wavefronts above/below caustics in the shadow zone are used to define another class of diffracted wavefronts which have not been previously modeled using ray tracing techniques.**

3.6.1 Standard ray-tracing constructed waveform

Using standard ray-tracing computations, broadband acoustic receptions are modeled by identifying the number of arrivals (eigenrays), their amplitudes, traveltimes, and caustic phases, as described in Section 3.4. The source and receiver locations as well as the source spectrum must be known. Without considering diffraction, acoustic waveforms can be constructed that match normal-mode computations exceptionally well, except possibly during and after the crescendo where diffraction effects can be significant.

Figure 3.16 shows the measurement front for a deep-ocean range-invariant sound speed profile, $c_{Munk}(z)$. The source is located at the sound-channel axis (a depth of 1200 m), and the receiver is at a range of 500 km. A hydrophone on the sound-channel axis will receive 18 arrivals. The traveltimes are specified where the measurement front crosses the receiver depth. The simultaneously received arrivals combine coherently since they share the same traveltime and caustic phase.

The cusps of the measurement front represent caustic points and the area above the surface-side cusps and below the bottom-side cusps is termed the "non-ensonified region" or "shadow zone," the area where no refracted acoustic energy is present.

For a hydrophone at a depth of 500 m, there are 12 totally refracted multipath receptions, from 335.7943 to 337.5682 seconds. Standard ray-tracing results do not incorporate diffraction of acoustic energy into the shadow zones, but exact solutions of the wave equation and other propagation techniques verify the existence of this acoustic leakage[32]. In

Figure 3.17, the envelopes of the normal-mode and ray constructed waveforms are plotted. The spectrum of the waveform is centered at 75 Hz and is sinc-shaped and bandlimited to the first nulls at 60 and 90 Hz as defined in Equation 1.2. The normal-mode constructed waveform (dashed line), which incorporates diffraction, shows a trailing arrival at 337.7356 seconds, while the ray-constructed waveform (solid line) does not model this arrival. Returning to Figure 3.16, we see this arrival is precisely coincident with a caustic cusp (as indicated by the time marker at 337.7356 seconds). For the waveforms in Figure 3.17, only 65 normal-modes were included in the normal-mode constructed waveform causing the early arrivals to be inaccurately modeled.

3.6.2 Diffracted arrivals above/below caustics

White and Pedersen's evaluation of acoustic energy in the shadow-zone demonstrates[33] that wavefronts can be used to model acoustic energy in the shadow zones above/below caustics. The leakage is in the form of an arrival with essentially the exact traveltime of the caustic cusp. In Figure 3.18, we modify the measurement front of Figure 3.16 to include the diffracted arrivals by extending spurs vertically from the cusps. The diffracted front also affects the ensonified region, but this is essentially insignificant. For an arrival at 500 m, the corrected model predicts three diffracted arrivals with traveltimes of 337.7356, 337.8005, and 337.8373 seconds. The earliest diffracted pulse arrives approximately 0.17 seconds after the last ray-predicted arrival. White and Pedersen additionally state that the caustic phase attributed to the arrival (above or below) a caustic cusp should advance 45° and the amplitude should fall off rapidly with depth away from the cusp.

In Figure 3.19, the envelope and phase of the 550 meter deep reception is plotted, and we focus on the last second of the reception. The normal-mode constructed waveform is plotted using a dashed line and the corrected ray constructed waveform is plotted using a solid line. By incorporating the three additional diffracted arrivals, a waveform is constructed which is in agreement with normal-mode solutions; although, the last two arrivals are quite weak and not visible on this plot. Several other simulation configurations have been studied to verify that the arrivals have traveltimes coincident with the caustic cusps and have the 45° additional caustic phase.
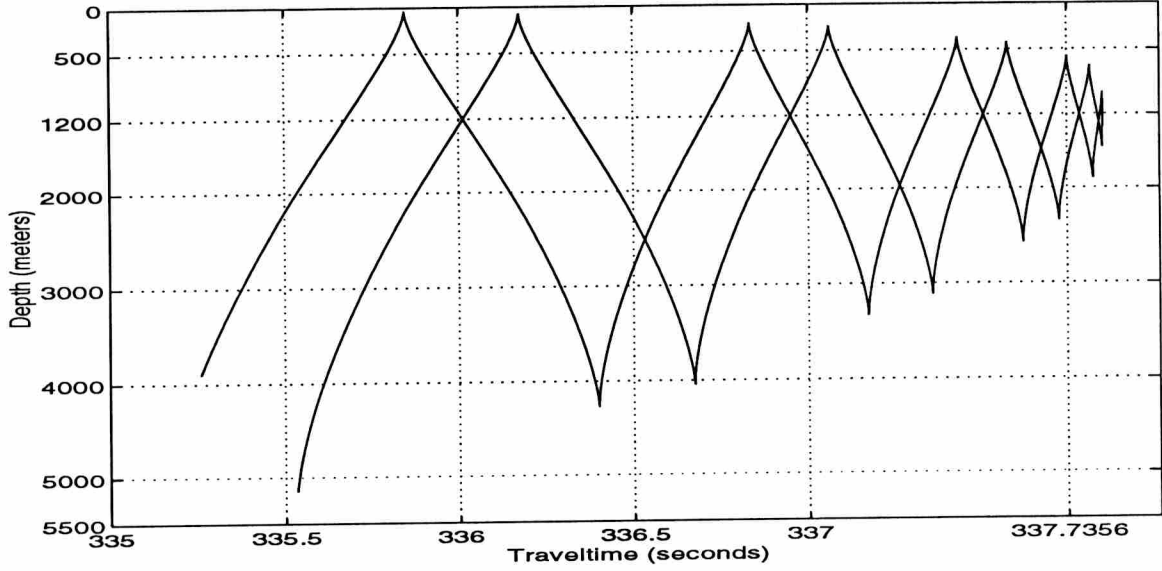
Figure 3.16: Measurement front: 1200 m source, 500 km range. There are 9 surface-side caustic cusps and 8 bottom-side caustic cusps. The shadow zone is exterior to the measurement front. A 500 deep receiver will not receive a totally refracted arrival with a traveltime of 337.7356 seconds, but known extensions to the ray tracing propagation method will predict a diffracted arrival with this traveltime.

3.6.3 Reciprocity

Since acoustic propagation is *reciprocal* for our ocean model, it will be interesting to determine where the well-known diffracted fronts above and below caustics *map* for reciprocal transmissions. From a ray perspective, reciprocity means that the ray from a source located at point p_o and passing through point p_r at traveltime T_r can be traced backwards from p_r over the reversed path through p_o with identical traveltime T_r. In terms of the phone impulse response the statement of reciprocity is

$$h_{x_o,z_o}(t \mid x_r, z_r) = h_{x_r,z_r}(t \mid x_o, z_o) \tag{3.34}$$

Consider a source at depth z_o, not on the sound channel axis. (An axial source will turn out to be trivial.) The goal is to map the location of the known-to-exist diffracted fronts above/below the cusps into the measurement front for the reciprocal transmission. This is accomplished in a two-step procedure and will be further described by way of an example.

55
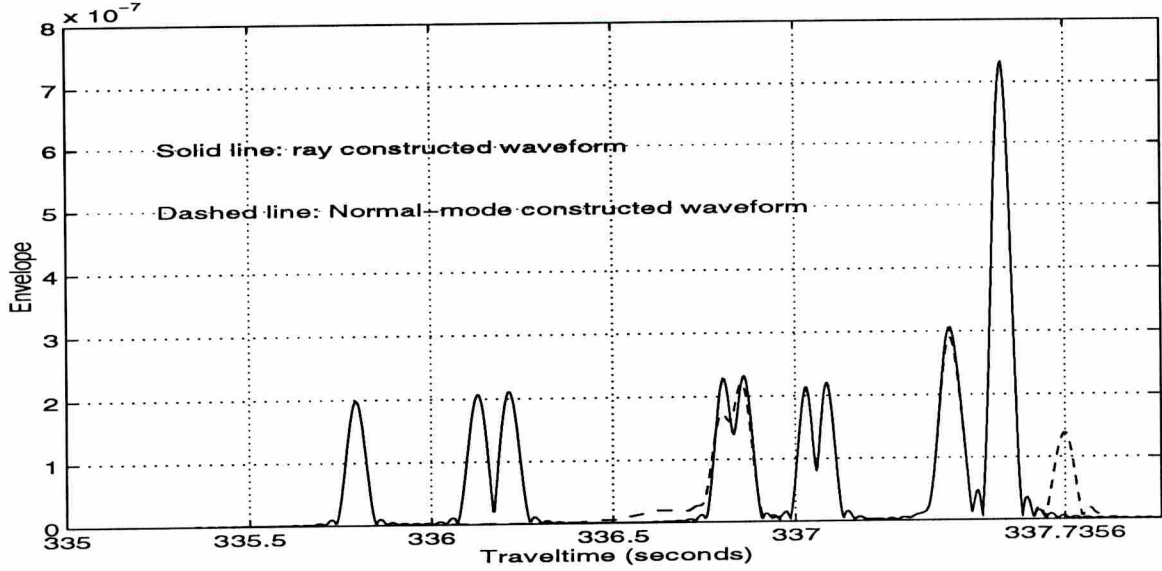
Figure 3.17: Envelopes of normal-mode (dashed) and ray (solid) constructed arrivals. Source depth 1200 m, range 500 km, receiver depth 500 m. The normal mode solution to the wave equation includes both refracted and diffracted energy. The normal mode constructed waveform shows an arrival with a traveltime of 337.7356 seconds where standard ray tracing computations do not model this arrival.

Step P: Calculate the measurement front for the source depth, z_o, and range R. This will be called the *primary front*, $h_{z_o}(z, t \mid x = R)$.

Step H: Consider a hypothetical source depth z_r and calculate the corresponding measurement front for the range R. Call this the *hypo front*, $h_{z_r}(z, t \mid x = R)$. By reciprocity, the traveltimes to depth z_o on the *hypo front* correspond to the traveltimes on the *primary front* to depth z_r. $h_{z_r}(t \mid x_o, z_o) = h_{z_o}(t \mid x_r, z_r)$. If z_o lies exterior to any caustics of the *hypo front*, say at times $t_r[n]$, add the diffracted eigenray endpoint "z_r at time $t_r[n]$" to the *primary front*.

Repeat Step H for all reasonable source depths. This yields an extension of the *primary front* consisting of diffracted arrivals whose traveltimes are greater than all of the totally refracted arrivals.

A brief example will make the procedure clear. Consider the measurement front from a $z_o = 500$ m deep source at a range of $R = 500$ km shown in Figure 3.20A. The wavefronts are

56
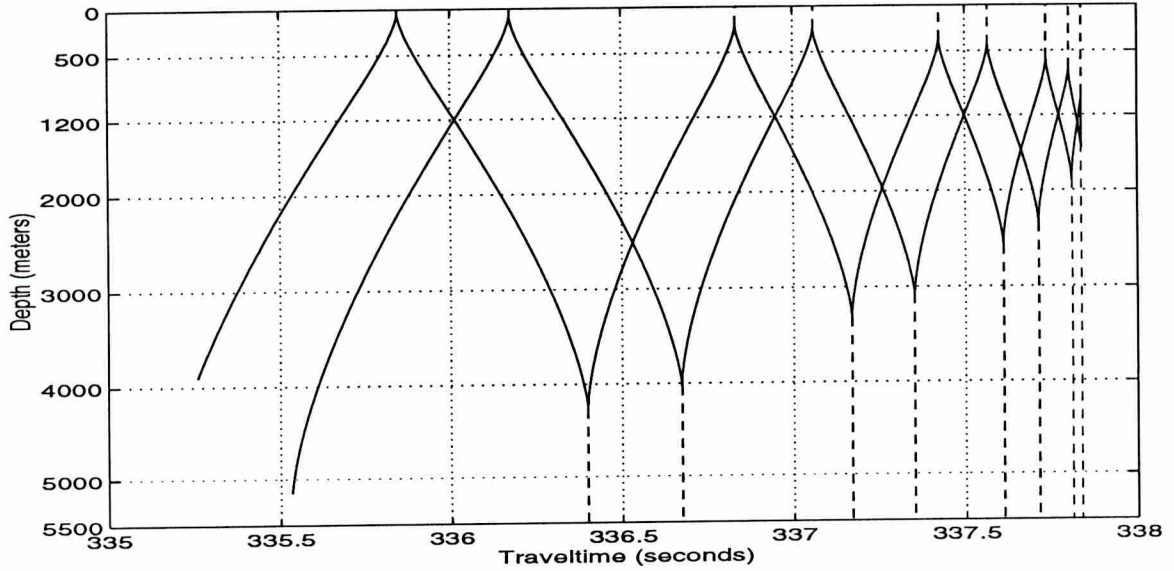
Figure 3.18: Measurement front: source 1200 m, range 500 km (solid). Diffracted Measurement fronts (dashed). For a 500 meter deep receiver, three diffracted wavefronts will be received with traveltimes of **337.7356, 337.8005, and 337.8373 seconds.**

the result of standard ray tracing and are totally refracted. Let this be the *primary front* of Step P. For Step H, consider the *hypo front* from a $z_r = 1200$ m deep source. This is shown in Figure 3.16. Evaluating the arrival times at a depth of $z_o = 500$ m, three diffracted arrivals will be present at $t_r[1] = 337.7356, t_r[2] = 337.8005$, and $t_r[3] = 337.8373$ seconds. These points (marked by x) are added to the *primary front* at a depth of $z_r = 1200$ m. This is shown in Figure 3.20B. Step H is repeated. Consider the *hypo front* from a $z_r = 1400$ m deep source shown in Figure 3.20C. Evaluating the arrival times at a depth of $z_o = 500$ m, three diffracted arrivals will be present at $t_r[1] = 337.7201, t_r[2] = 337.8124$, and $t_r[3] = 337.8322$ seconds. These points are added to the *primary front* at a depth of $z_r = 1400$ m. This is shown in Figure 3.20D where we have connected the diffracted arrival points and the shape of the diffracted front begins to take form.

After conducting Step H across all reasonable source depths, (Step H was executed for $z_r = 600$ to 2600 meters in 20 m increments) the diffracted measurement front is formed for a source at a depth of 500 meters and a range of 500 km. In Figure 3.21 the measurement front corresponding to the totally refracted rays is plotted using a solid line and the diffracted

57
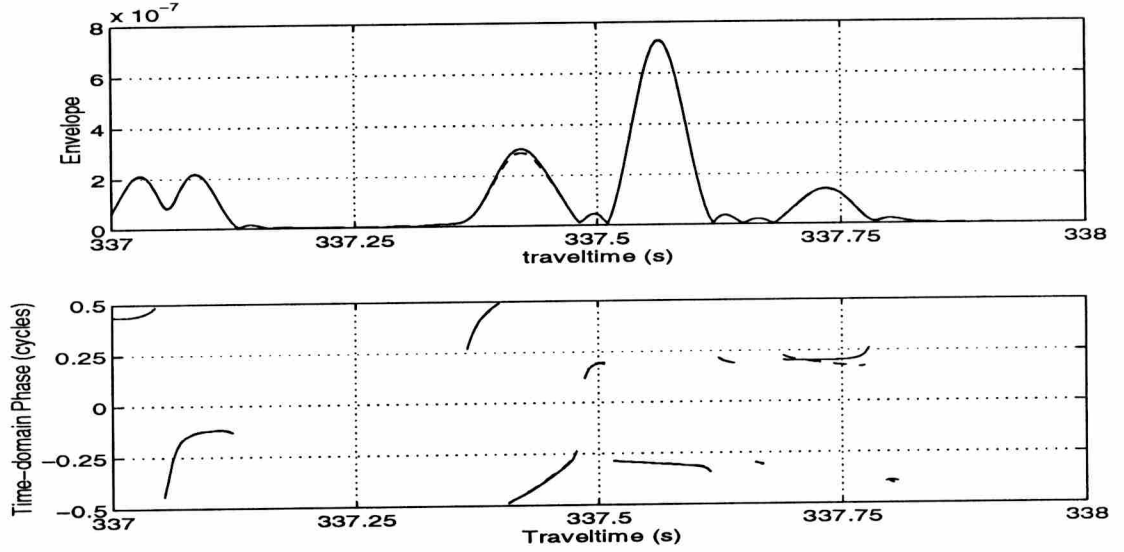
Figure 3.19: Last second of reception. Envelope and phase of received wave-
forms: normal mode (dashed) corrected ray (solid). Source
1200 m, range 500 km, receiver 500 m. The amplitude of the
diffracted ray arrival was selected to match the normal-mode
constructed waveform.

measurement front, computed using reciprocity, is plotted using a dashed line.

In Figure 3.22, normal modes are used to construct the waveform envelope in depth-time
space analogous to a ray constructed measurement front. The thin lines of the measurement
fronts have been effectively replaced by the actual pulse structure. The logarithm of the
envelope is displayed to enhance the weaker diffracted fronts. This enhances the visibility of
the weaker fronts, but also enhances the time-domain sidelobes of the stronger arrivals. A
gray scale is used, and light intensities indicate loud arrivals while dark intensities indicate
weak arrivals. By comparison with Figure 3.21, the first two diffracted fronts are visible.
The third diffracted front is as weak as the time-domain sidelobes of the previously arriving
pulses and cannot be made visible through the log enhancement.

3.6.4   Discussion

The method identifies the traveltimes, caustic phases, and direction of arrivals of these
additional fronts impinging on an array at range R. The diffracted fronts extend the ac-
cordion shape mimicking the totally refracted fronts. Using normal mode theory, we have

58
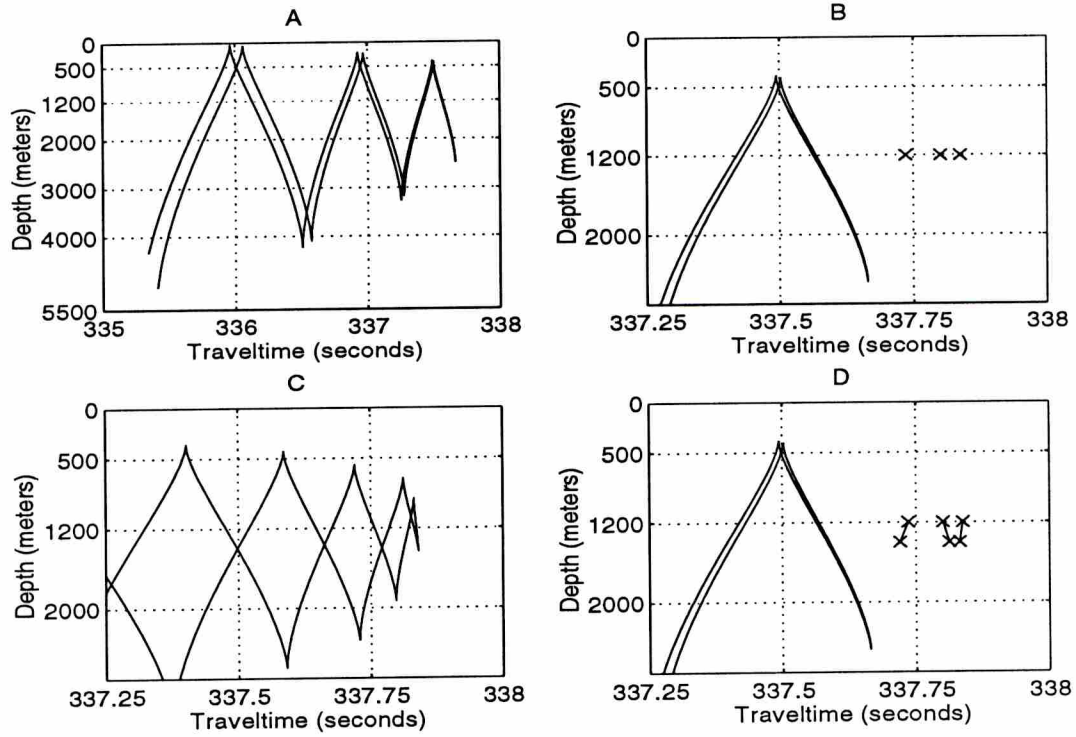
Figure 3.20: Example of P and H Steps to construct diffracted wavefronts.
A: Step P *primary front*. B: *primary front* and three diffracted
traveltime and depth points marked by an x. C: *hypo front* for
$z_r = 1400$ m. Three diffracted traveltimes are evaluated at the
caustic cusps below a depth of 500 m. D: Traveltimes obtained
from C are mapped into the reciprocal space at a depth of
1400 m. This step is repeated for many depths to construct
the complete diffracted front.

determined that the amplitudes of the diffracted arrivals can be greater than the loudest
totally refracted arrival or can be essentially insignificant.

In Figure 3.23, results from standard PE propagation method are compared to the nor-
mal mode constructed waveform for the last second for this same scenario. As previously
discussed the standard PE method does not yield comparable results for high-angle propa-
gation. Since the source is at a depth of 500 m, there is not a direct axial path from source
to receiver where the PE method yields reliable results. Nevertheless, the PE results do
show the primary diffracted wavefront, a benefit the standard ray tracing computations do
not have. The time-domain phase is shown, and there is a difference of approximately a
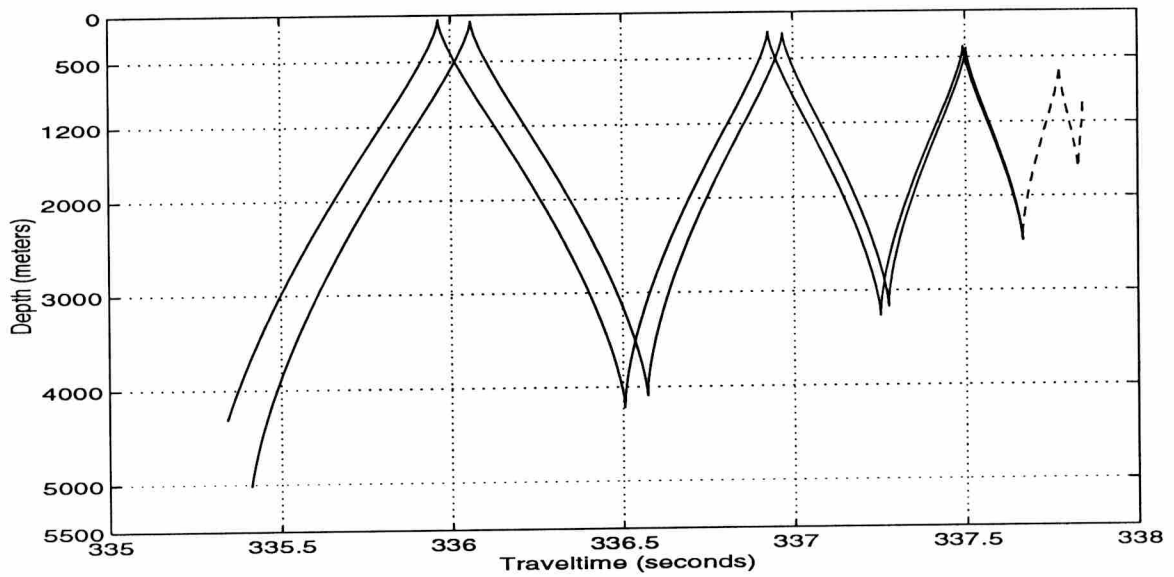
Figure 3.21: Measurement front: source 500 m, range 500 km (solid). Diffracted wavefronts, obtained using reciprocity (dashed).
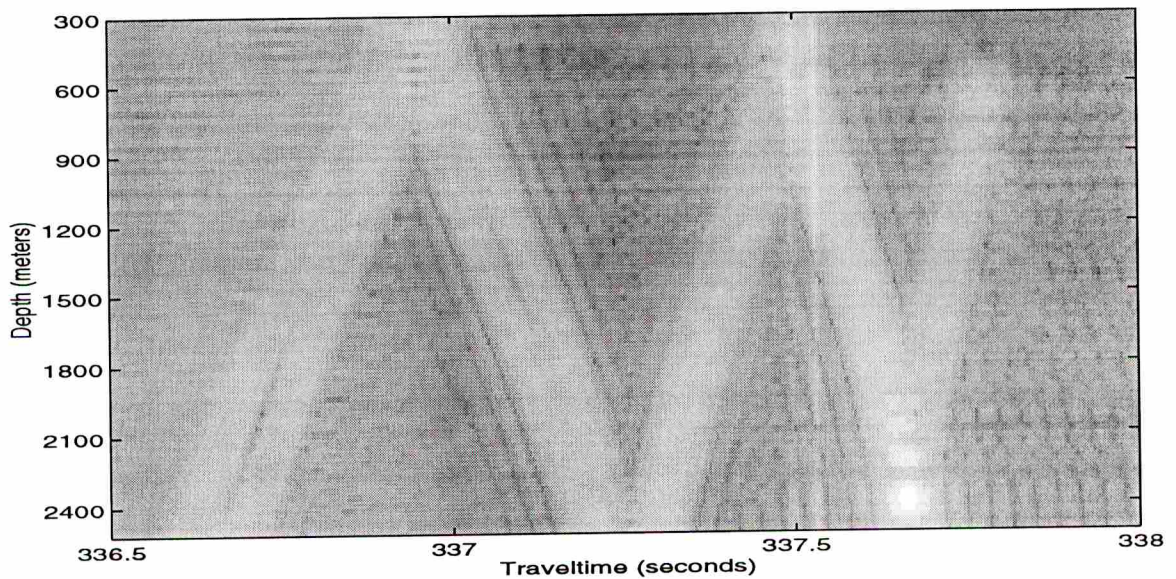
Figure 3.22: Normal-Mode computed wavefront envelope encoded in gray scale. White indicates a loud arrival and black indicates no sound. The first two sheets of the diffracted wavefront are visible.

60
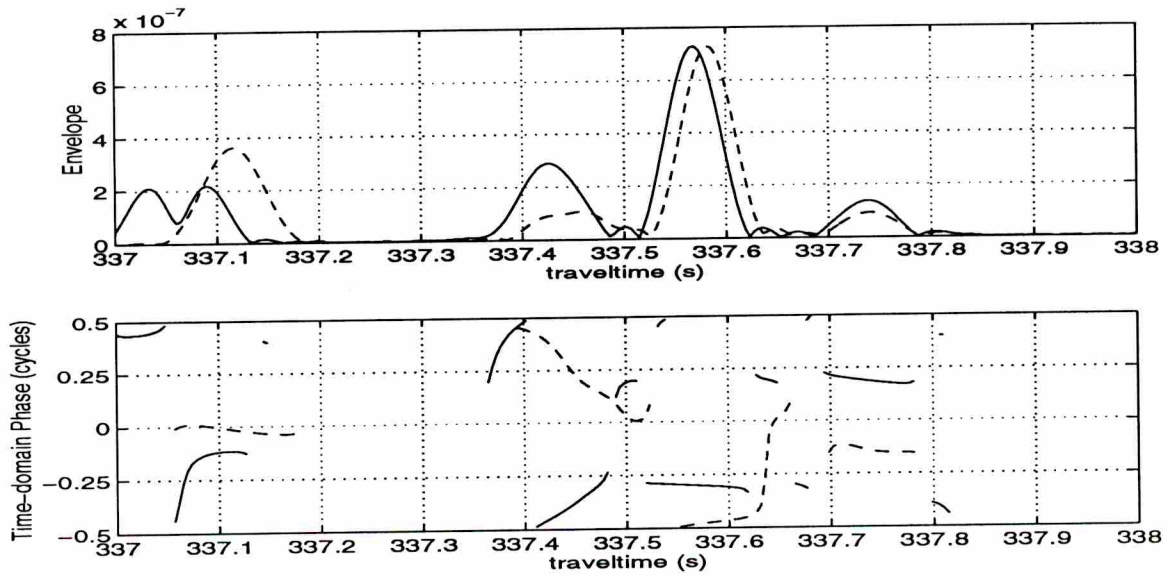
Figure 3.23: The top figure shows the normal mode (solid) and PE (dashed) constructed waveform envelopes. The PE propagation method does account for the diffracted wavefront. The bottom figure shows the time-domain phase for the normal mode (solid) and PE (dashed) constructed waveforms. The time-domain phase differs by more than a quarter of a cycle for the primary diffracted wavefront arrival.
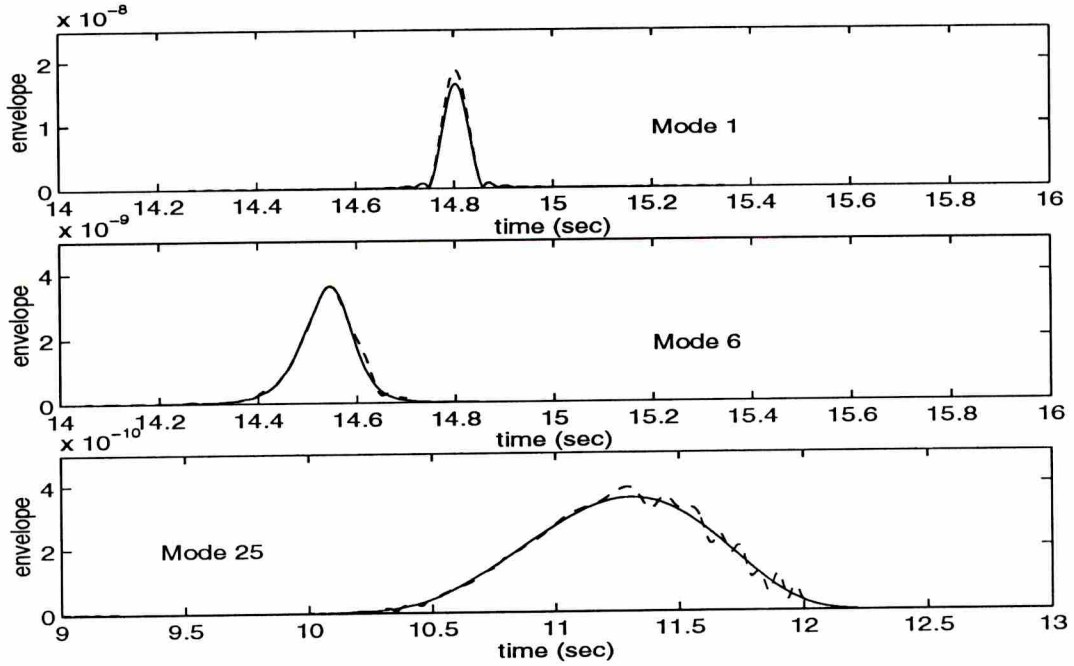
Figure 3.24: The broadband mode filter signal envelopes from modeled receptions along a 40 phone vertical line array are shown for normal mode constructed waveforms (solid) and ray constructed waveforms (dashed). The filter was designed to pass mode 1 for the top figure, mode 6 for the second figure and mode 25 for the bottom figure.

quarter cycle for the diffracted front. The diffracted ray constructed waveform time-domain phase precisely matched with the normal mode (ground truth) waveform.

Another benefit of a ray-based reciprocal method over PE computations for computing the diffracted and refracted energy is that the exact number of arrivals and their travel-times, phases, and direction of arrival can be computed whether or not the arrivals are resolved. Please note that the PE propagation method produces the received pressure field and does not give specific information on the individual wavefront arrivals. For long range propagation (multiple megameters) the diffracted arrivals will be unresolved.

By constructing acoustic arrivals at several depths along a vertical line array, using the ray methods described in this chapter, broadband mode forming[37] can be used to monitor single normal acoustic mode arrivals. Broadband mode forming is a vertical spatial filtering procedure which exploits the orthogonality of the normal acoustic modes as a function

of depth to extract single mode receptions. Figure 3.23 shows the broadband mode filter output for normal modes 1, 6, and 25[10]. The precise normal mode output envelope is drawn using a solid line and the normal mode filtered ray constructed waveforms are drawn using a dashed line. The low-frequency broadband source as described in Equation 1.2 is used and propagated over a 1 Mm propagation path. Acoustic mode 1 arrives last and is dispersed the least of all modes. Higher modes arrive earlier and are increasingly dispersed[11].

The broadband mode filtered outputs using the ray constructed waveforms yield nearly identical arrival envelopes as compared to the normal mode (ground truth) envelopes. It is useful to have acoustic waveforms described in terms of wavefront arrivals because much of our understanding of the impact of ocean processes on acoustic propagation is based on amplitude and phase fluctuations of wavefront arrivals. These fluctuations can be induced on a ray-constructed waveform and the impact on a given normal mode can be studied by analyzing the mode filter outputs.

Many underwater acoustic signal processing algorithms are based on a ray or normal-mode framework. It is important to understand the similarities and differences of ray and normal-mode based propagation modeling to understand the strengths and weaknesses of various signal processing algorithms with equivalent goals. Recently proposed source localization techniques exploit the ability to trace wavefront (ray) arrivals back to the source [39][40]. These approaches do not require full-wave matched-field processing[41] and exploit the numerical efficiency of ray tracing. However, a warning is served that diffracted wavefronts mimic totally refracted wavefronts but will not trace back to the source along an eigenray path, potentially causing a significant increase in uncertainty in the source location estimates.

---

[10]For more information on normal modes please see Appendix A.

[11]Each acoustic mode is composed of a sum of horizontally propagating *sub*modes, one submode for each inband acoustic frequency. Each submode travels at a different horizontal speed and at the receiver the submodes do not arrive simultaneously, but *dispersed*.

3.7   2D and 3D range variant propagation

For range varying computational ocean models, a ground truth solution can not be computed. In general, based on the nature of the variations to the sound speed field and the goal of a given study, a favorable propagation method can be selected. For example, propagation from shallow water over an abrupt shelf to deep water may be best modeled using normal mode theory employing mode coupling to model range dependence. Short range shallow water propagation through a varying sound speed profile with well known varying bottom properties may be best modeled using a PE propagation method. For long-range propagation through internal wave fields where it is of interest to study the early resolved wavefront arrivals, use of a ray propagation method is best.

In this work, it is of interest to focus on the propagation of the early resolved wavefronts and how they are affected by the presence of an internal wave field. The early arrivals correspond to the high angle rays. High angle rays reach their apex within a few hundred meters of the surface where the internal wave field is most active. Figure 3.25 shows a high angle ray path through a deep ocean sound speed profile, $c_{\text{Munk}}(z)$. This is the physical propagation path of the acoustic signal which represents an early resolved arrival. The dark and light shading represents the change in sound speed due to a single propagating internal wave mode. Light areas represent positive changes in sound speed and dark areas represent negative changes to the sound speed. This particular internal wave has special properties that will be discussed in detail in Chapter 4. Currently, it is of interest to compare the received acoustic waveforms generated from the available 2D range varying propagation methods for 2D range varying computational ocean models.

The ray propagation method is used to construct the received waveform envelope with and without the presence of an internal wave. This is shown in Figure 3.26 where the solid line describes the envelope with no internal wave present, and the dashed line describes the received acoustic envelope with the internal wave present. The sound speed profile used is $c_{\text{Munk}}(z)$. The source is located on the sound channel axis at 1200 meters deep. The receiver is located at a depth of 1250 meters and is 745 km from the source. The low frequency, broadband source signal is defined in Equation 1.2. The internal wave, $W_j(k, z)$ is defined by
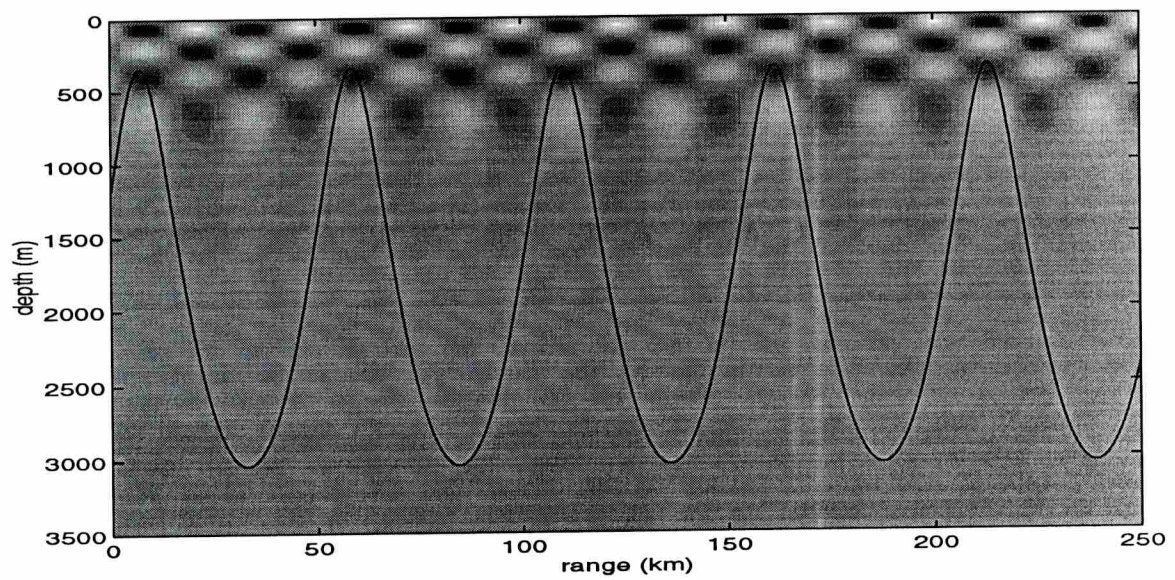
Figure 3.25: The dark line represents a single high-angle ray path which corresponds to an early arriving and possibly resolved wavefront at a down range receiver. The checkerboard pattern above 800 m is the change in sound speed induced by a single internal wave mode. Light areas indicate positive changes in sound speed and dark areas represent negative changes in sound speed.

65

the parameters: $j = 4$, $k/2\pi = 2.046\,cyc/km$, $\omega_j(k)/2\pi = 1.31\,cph$, $|\,G\,|= 0.2$, $\angle G = 21°$, and $\theta = 86°$. [j is the mode number; k is the wavenumber; $\omega_j(k)$ is the internal wave angular frequency; G is the complex internal wave strength and phase; θ is the propagation direction angle with respect to the nominal acoustic plane; the acoustic path cycle length is 56.4 km.] The 2D computational ocean model is described by

$$c(x, z, t) = c_{\text{Munk}}(z) + 2.5\,c_o\,N^2(z)\,\Re e\left(G_j(k, \theta)W_j(k, z)\,e^{i(kx\cos\theta + ky\sin\theta - \omega_j(k)t)}\right) \quad (3.35)$$

where $N(z)$ is defined in Equation 2.3. The model is studied for a transmission time of $t = 0$.

Any aggregate traveltime bias due to the presence of the internal wave is termed *internal wave bias* and has been addressed in several studies [5], [12], [7]. The main point is that the presence of the internal wave can have a significant impact on the envelope of the early acoustic arrivals as indicated by the arrival near the 9 second mark which has been significantly amplified by the presence of the single propagating internal wave mode.

The received waveform is constructed for the range varying normal mode propagation method and PE propagation method. The three received waveform envelopes are compared in Figure 3.27 where the ray constructed waveform is indicated using a dashed line, the PE constructed waveform using a dotted line, and the normal mode constructed waveform using a solid line. **None of the three propagation methods are in agreement.** As expected, the PE constructed waveform includes the effects of diffraction but does not accurately model the high angle acoustic propagation. The PE propagation method results are most reliable near the terminal section of the arrival. The normal mode propagation method does not show a significant variation due to the presence of the internal wave. The cyclic nature of a single internal wave mode causes a canceling effect in the perturbation calculation used for this method. Based on the numerous investigations similar to those presented in this chapter, the ray propagation method is best suited to describe the early ray arrivals, and these results will be relied upon to initiate a study of long range acoustic propagation through internal wave fields.

In moving to 3D space varying computational ocean models, the ray propagation method is the only method that can simulate 3D acoustic propagation with current computing
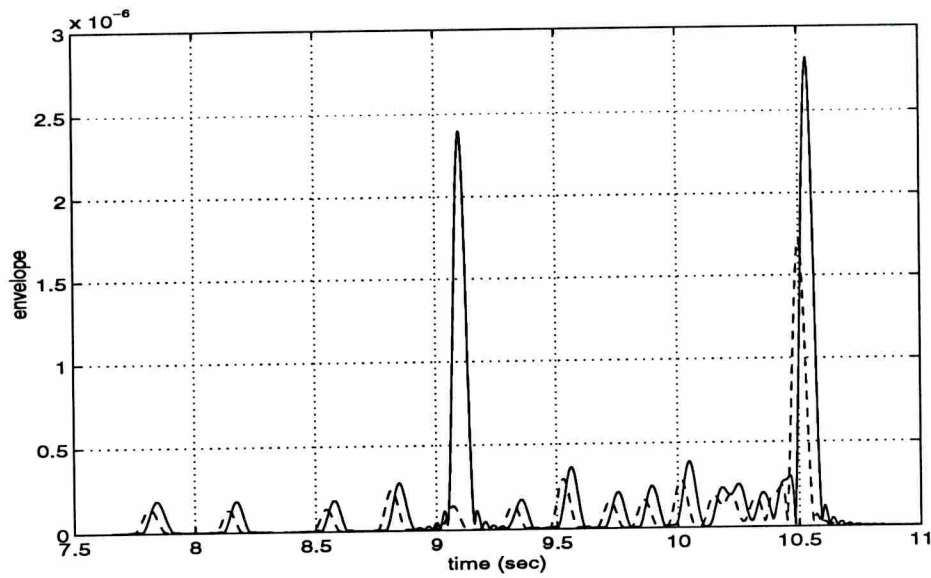
Figure 3.26: The ray constructed envelopes are shown for the case of no internal waves present in the ocean model (dashed) and a single internal wave field present in the ocean model (solid). The presence of the internal wave field has significantly changed the received envelope, especially the amplitude of the arrival just after the 9 second time mark. The apparent slight aggregate change in traveltime of all the arrivals is termed the internal wave bias.

power. It has been verified that low frequency broadband acoustic propagation can be accurately modeled using ray tracing computations. Two amplitude calculation methods have been developed and validated. The effects of diffraction have been studied and a procedure has been developed such that a modified ray propagation method can be considered as a "full physics" propagation method for 2D range invariant ocean models.

It is of interest to study the propagation of the early resolved wavefront arrivals, since these are the candidate receptions that can be used to measure changes in acoustic traveltime. Comparisons of 3D and N x 2D propagation methods will be addressed in Chapter 4 for these early wavefront arrivals. Additional studies are included to lead toward the feasibility of internal waves causing the received acoustic amplitude to mimic Rayleigh fading coincident with stable time-domain phase as well as determine the feasibility of identifying individual internal waves present in the propagation path based on the acoustic reception.
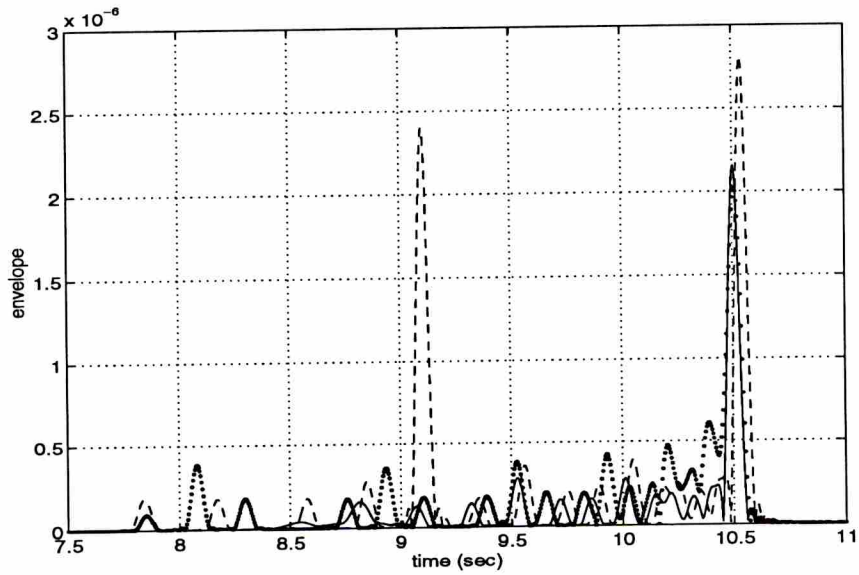
Figure 3.27: The normal mode (solid), PE (dotted), and ray tracing (dashed) constructed waveform envelopes are shown for the same 2D range varying computational ocean model. One internal wave is present in the ocean model. None of the three propagation methods are in agreement.

CHAPTER 4

Spatially synchronized internal waves

The class of spatially synchronized internal waves is defined and their impact on high-angle acoustic propagation is studied. Internal waves from this class have the potential to cause an early (high-angle) acoustic arrival to have stable time-domain phase coincident with fluctuating time-domain amplitude. The acoustic coherent (phase stable) focusing and defocusing (amplitude fluctuation) takes place in both the nominal acoustic plane and the YZ plane, and we call these vertical focusing and transverse focusing, respectively. In detailing the effects internal waves have on acoustic propagation, the dimensionality of the computational ocean model will be increased step by step from a range invariant, time invariant 2D model to a complete 3D space and time varying model. The computational ocean models used are in the form of Equation 2.9. The sound speed profile used to describe the deep ocean waveguide is the Munk profile denoted $c_{\text{Munk}}(z)$ and defined in Chapter 2. All simulations presented investigate a single early arrival at a range of approximately 750 km. The source is located on the sound channel axis at a depth of 1200 m. The rays with vertical launch angles, α_o, between $-12.0°$ and $-12.6°$ form the timefront sheet of interest. These rays all have 14 upper turning points, and their endpoints constitute a single down-going sheet of the timefront after 504 seconds of propagation.

4.1 Vertical focusing of acoustic rays

To begin the investigation of spatially synchronized internal waves, the ground work is established to define "vertical focusing" of the acoustic rays. Two-dimensional range-invariant and range-variant computational ocean models are studied. The results lead to a

69

study of micromultipath generation.

4.1.1   2D Range-invariant vertical focusing

To simplify the description of the deterministic impact of a single internal wave on acoustic propagation, a time-invariant 2D computational ocean model is used; $c(x, y, z, t) = c(x, 0, z, t_o)$. The simplest case is a single internal wave traveling perpendicular to the nominal acoustic plane. From Equation 2.5, when $\theta = \pm 90°$, $k_x = k \cos \theta = 0$, describing a range-invariant model where there is no transverse gradient, and sound strictly travels in the nominal acoustic plane as illustrated by the computational ocean model in Equation 4.1.

$$c(x, 0, z, t_o) = c_{\text{Munk}}(z) + \delta c(z) \tag{4.1}$$

The internal-wave induced sound-speed deviation, $\delta c(z)$, at the acoustic ray top turning depth is important since this is where the the majority of the internal-wave influence on acoustic propagation takes place[10]. An intuitive feel for a single internal wave's impact on acoustic propagation is developed by considering the shape of δc at the ray's top turning depth, and recalling that rays bend toward sound speed minimums. Figure 4.1 shows the change in sound speed caused by an internal wave with four sound speed extrema in the vertical ($j = 4$) and horizontal wavenumber $k/2\pi = 2.046$ cyc/km. In a range-invariant ocean model, each ray has a unique top turning depth, z_{tt}, by Snell's Law

$$z_{tt} = \min_{z \in (0, z_s)} \mid c(z) - \frac{c(z_s)}{\cos(\alpha_o)} \mid \tag{4.2}$$

Therefore, the underlying rays that form the timefront are refracted by the internal-wave gradient, $\partial(\delta c(z))/\partial z$, evaluated at the respective turning depths. Just as the Munk profile globally focuses rays to form the deep-ocean channel, the internal wave focuses rays locally. The top turning depths for rays with launch angles of $\alpha_o = \pm 14.9°, \pm 12.3°, \pm 9.3°, \pm 5.6°$ are identified in Figure 4.1. At these depths the internal wave induced change in sound speed gradient is zero. The internal wave focuses and defocuses the acoustic amplitude about these rays. For example, consider a timefront composed of rays with launch angles between $-12.0°$ and $-12.6°$. The rays with launch angles above $-12.3°$ will be refracted downward toward the $-12.3°$ ray. The rays with launch angles below $-12.3°$ will be refracted upward toward
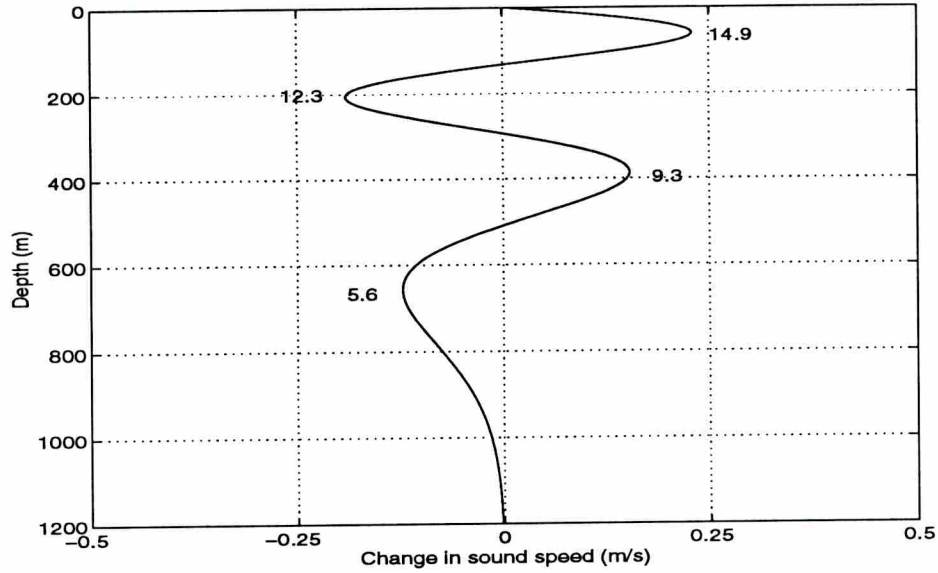
Figure 4.1: Internal-wave induced change in sound speed, $\delta c(z)$, and ray top-turning depths labeled by ray launch angle, α_z in degrees.

the $-12.3°$ ray. In both cases this is due to the locally "cupped" shape of the internal wave. The internal wave focuses the rays toward the unperturbed $-12.3°$ ray on the timefront. By similar reasoning, rays with top turning depths near 400 m are defocused away from the $-9.3°$ ray. The natural oscillatory shape of internal waves through the thermocline causes the amplitude of the early, high angle arrivals to be focused or defocused along the timefront. This is called "vertical focusing" since the focusing takes place in the nominal acoustic plane.

To quantify the amount of focusing and defocusing, the power relative to a no-internal-wave ocean reception using the ray endpoint density method is calculated for the $-12.3°$ arrival at a range of 750 km. The internal-wave induced power fluctuation is plotted in Figure 4.2 for various internal wave strengths defined by $\delta c(z)$ at $z = 202$ m. When the phase of the internal wave is reversed by a half cycle, defocusing results. It is concluded a single internal wave of modest strength can cause a significant acoustic amplitude change.

4.1.2 2D Range-variant vertical focusing

In actuality, the internal wave is propagating and a 2D range-variant computational ocean model results. When the internal wave wavelength projected in the direction of sound

71
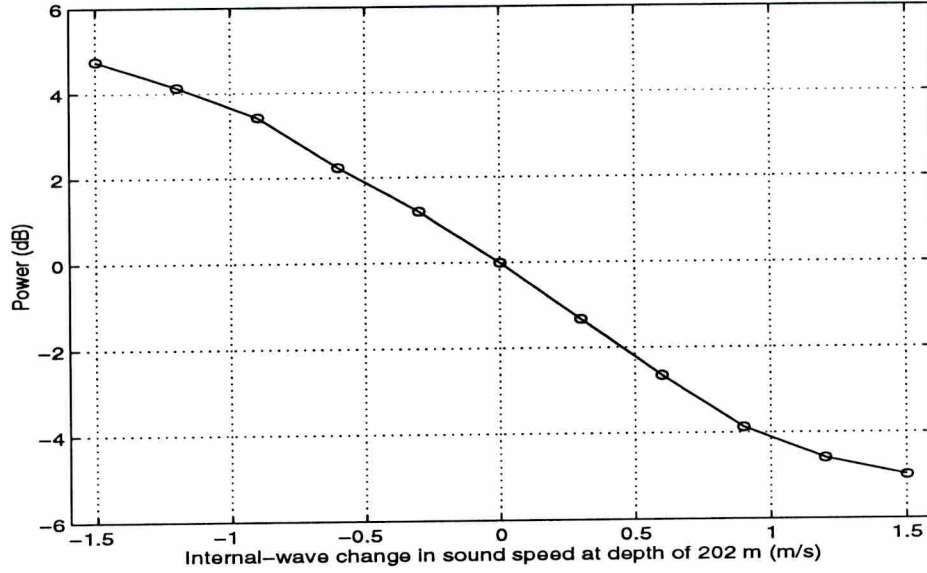
Figure 4.2: Internal wave induced power fluctuation resulting from coherent focusing and defocusing in range-invariant model. The arrival has a top-turning depth of 202 meters below the ocean surface.

propagation, $\Lambda_x = 2\pi/(k\cos\theta)$, is an integral multiple of the acoustic path cycle length, the propagating internal wave can appear to be range invariant. The impact of the internal wave is reinforced each time the acoustic wave travels through the upper thermocline. In this case, the internal wave is "spatially synchronized" to the acoustic arrival.

When an internal wave is propagating horizontally at an angle other than $\pm 90°$ to the acoustic propagation, the 2D computational ocean model is range variant, $c(x, 0, z, t)$. When Λ_x is large, thousands of meters, the internal wave changes slowly with range. This is referred to as the long-wavelength case. But for internal-wave propagation direction angles away from normal and large-k internal waves, Λ_x can be as low as a few hundred meters. This is referred to as the short-wavelength case. In this case, the rapid changing of the internal wave induced sound speed along the top turning portion of the acoustic path yields a canceling effect and a spatially synchronized internal wave causes little change in the received arrival amplitude or time-domain phase.

In the long-wavelength case, the effect of spatially synchronized internal waves can be significant. In a frozen ocean model (time invariant sound speed field), an internal wave is spatially synchronized with an arrival with acoustic ray path cycle length, $L_{ray}(\alpha_o)$, under

72
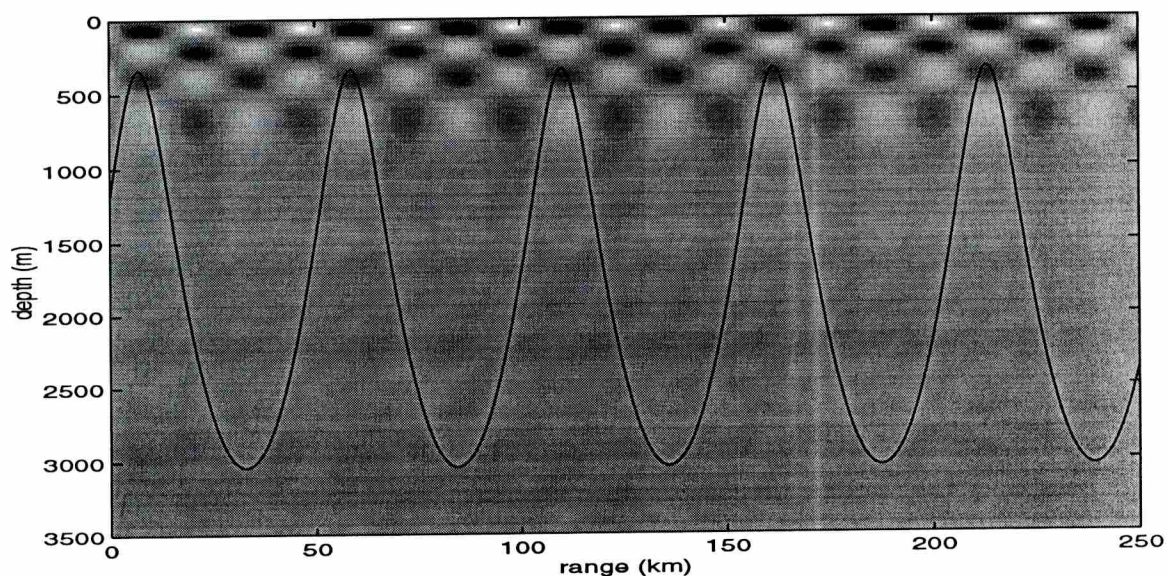
Figure 4.3: The dark line represents a single high-angle ray path which corresponds to an early arriving and possibly resolved wavefront at a down range receiver. The checkerboard pattern is the change in sound speed induced by a single internal wave mode. Light areas indicate positive changes in sound speed and dark areas represent negative changes in sound speed. This internal wave is spatially synchronized to the acoustic ray drawn. This is an example of the long-wavelength case where $n = 2$. This illustration demonstrates how the ray spatially samples the propagating internal wave, and how the spatial synchronization condition can cause a reinforcing effect on the bending of the acoustic ray paths.

73

the condition

$$L_{\text{ray}}(\alpha_o) = n\Lambda_x = \frac{2\pi n}{k\cos\theta} \qquad (4.3)$$

where n is an integer. Figure 3.25 is replicated in Figure 4.3 and shows a high angle ray that has an acoustic path cycle length that is twice ($n = 2$) the wavelength of the internal wave. The solid line denotes the ray path, and the shading across the field indicates changes in sound speed caused by the propagating internal wave.

Many seconds will pass between times when the propagating acoustic wave is at its top turning depth, and in this time the internal wave may have moved significantly; thus, a time-varying condition for spatial synchronization must be derived. By including time, the spatial synchronization condition becomes

$$L_{\text{ray}}(\alpha_o) = \frac{2n\pi}{k\cos\theta - \omega/c} \qquad (4.4)$$

For a given internal wave, the propagation direction angles required for spatial synchronization are

$$\theta = \cos^{-1}\left(\frac{2\pi n}{kL_{ray}(\alpha_o)} + \frac{\omega}{kc}\right) \qquad (4.5)$$

When the spatially synchronized internal-wave phase maximizes $\mid \delta c(z) \mid$ and the acoustic ray path is at its top turning point, the internal wave will have the greatest focusing effect. Each time the ray reaches its top turning point, the internal wave causes a maximum reinforcement. This is the case in Figure 4.3 where each time the ray reaches its top turning point the internal wave phase maximizes $\mid \delta c(z) \mid$ as indicated by the dark shading. If the internal wave is spatially synchronized with an acoustic ray path that has a top-turning depth where the internal wave's change-in-sound-speed gradient is zero (with respect to depth), vertical focusing or defocusing (depending on the phase of the internal wave) results.

Long-wavelength internal waves that are not spatially synchronized to a ray cycle length cause little change in the received time-domain amplitude and phase.

There are three ranges of Λ_x: large, mid-range, and small Only the large and mid-range cases are effective in spatial synchronization. This characterization has fuzzy boundaries, but roughly a *large* Λ_x is larger than one-fifth of L_{ray}, while a *small* Λ_x is less than 0.04 L_{ray}. Internal-wave wavelengths projected on the direction of acoustic propagation that are between these extremes are said to be "mid-range". When Λ_x is in the mid range, the
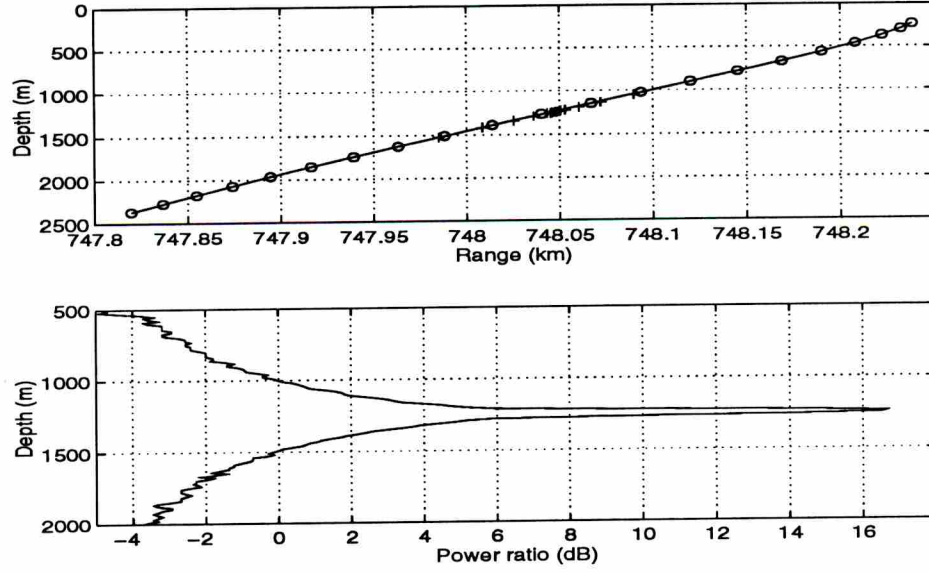
Figure 4.4: **Vertical focusing in forced 2D range-variant internal wave model. Top: Timefront for early arrival without internal wave perturbation and corresponding ray endpoints (o). Also, the ray endpoints resulting from an ocean model including a single propagating spatially synchronized internal wave are marked by (+), and these points fall nearly on the internal-wave free timefront indicating the internal wave does not induce a significant phase shift on the received acoustic signal. Bottom: The internal wave induces a 17 dB gain in power at a specific location on the front.**

amplitude focusing can be very intense (over 10 dB received power increase or decrease relative to a reception propagated through an internal-wave free ocean model).

For an example of mid-range Λ_x focusing using a 2D computational ocean model, consider rays uniformly spaced in launch angle between $\alpha_o = -12.6°$ and $-12.0°$. Figure 4.4a shows the timefront (solid line), after 504 seconds of propagation for an ocean without internal waves. This is the high-angle, early arrival that will be studied throughout the chapter. The internal waves used in the computer simulations are listed in Table 4.1. IW1 is used and set to a propagation direction angle of $\theta = 86.0°$ to meet the mid-range spatial synchronization condition, corresponding to $n = 8$ in Equation 4.5. The ray-endpoints (circles) represent no internal wave present in the ocean model and are uniformly spaced along the timefront. The inclusion of the internal wave has significantly vertically focused

75

the acoustic rays with endpoints marked by a plus sign (+), yet they lie nearly on top of the same timefront. This means the internal wave focuses the amplitude along the front but does not significantly alter the time-of-arrival; that is, the internal wave bias is insignificant for this example. Figure 4.4b shows the change in arrival power, due to the inclusion of the internal wave using the ray endpoint density method. For this model, a hydrophone at a depth of 1250 m and range near 748 km would enjoy a 17 dB gain due to the presence of the internal wave.

When internal waves are not spatially synchronized they yield little impact to the amplitude of the early acoustic reception. Figure 4.5 shows results of an analysis similar to that of Figure 4.4. IW1 is used and set to a propagation direction angle of $\theta = 75.0°$ such that the spatial synchronization condition is met ($n = 30$ in Equation 4.5) but falls into the category of a short-wave length case. The ray endpoints lie nearly on top of the unperturbed endpoints indicating that the presence of the internal wave had essentially no effect due to rapid cancelation of the sound speed perturbation along the ray path. The change in received power induced by the internal wave is insignificant as seen in the lower plot where the change in power is no more than 0.01 dB. Similar results occur for spatially non-synchronized internal waves of any projected wavelength.

4.1.3 Micromultipaths

When ray paths focus, the acoustic amplitude significantly increases. At the point that two adjacent ray paths cross, a caustic point is obtained. This is the point where the cross sectional area of the ray tube vanishes. This focusing can result from a spatially

Name	j	$k(cyc/km)$	$\omega_j(k)(cph)$	G (magnitude and phase)	$\delta c_{max}(m/s)$
IW1	4	2.046	1.31	0.2, 21°	0.147
IW2	1	1.315	2.00	0.7, −29°	0.352
IW3	1	0.229	0.92	6.0, 42°	0.215
IW4	3	2.100	1.55	0.3, 146°	0.210
IW5	5	1.729	1.11	0.1, 240°	0.050
IW6	10	1.120	0.53	0.08, 105°	0.025
IW7	21	0.415	0.12	0.05, 240°	0.008

Table 4.1: Internal waves used in computer simulations
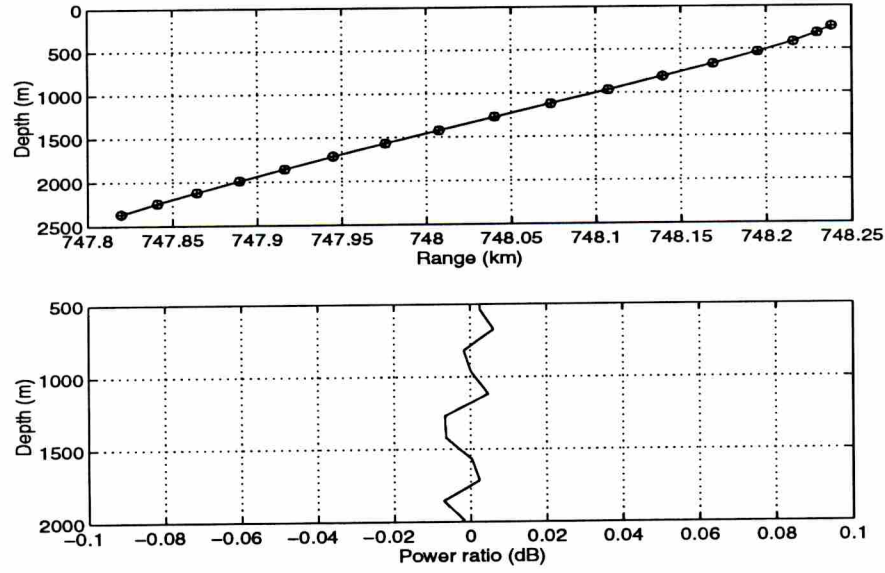
Figure 4.5: Top: Timefront for early arrival without internal wave pertur-
bation and corresponding ray endpoints (o). Also, the ray end-
points resulting from an ocean model including a single prop-
agating internal wave that is not spatially synchronized are
marked by (+), and these points fall nearly on the internal-
wave free ray endpoints indicating that internal wave does not
impact the acoustic reception. Bottom: The internal wave in-
duces insignificant change in received power along the front, less
than 0.01 dB.

synchronized internal wave. The following discussion and analysis concentrates on the
propagating acoustic wavefront after focusing.

After adjacent ray paths cross, they may diverge creating a *microfront*. After the cross-
ing, the single timefront sheet divides into a mainfront (the original timefront sheet) and a
microfront. The microfront is bordered by two caustic cusps. Figure 4.6 shows an illustra-
tion of a spawned microfront to discuss details of the post-focus wavefront. It is clear that a
hydrophone could receive three distinct wavefronts (2 mainfronts and 1 microfront) for this
example. The reception of these closely arriving multiple arrivals is termed *micromultipath*.
The mainfront and the microfront are labeled in the sketch (Figure 4.6). There are three
issues to discuss: the generation of diffracted fronts, the time-difference-of-arrival of the
micromultipath, and the difference in caustic phase contribution to the time-domain phase
of each arrival. These issues will be addressed in turn.
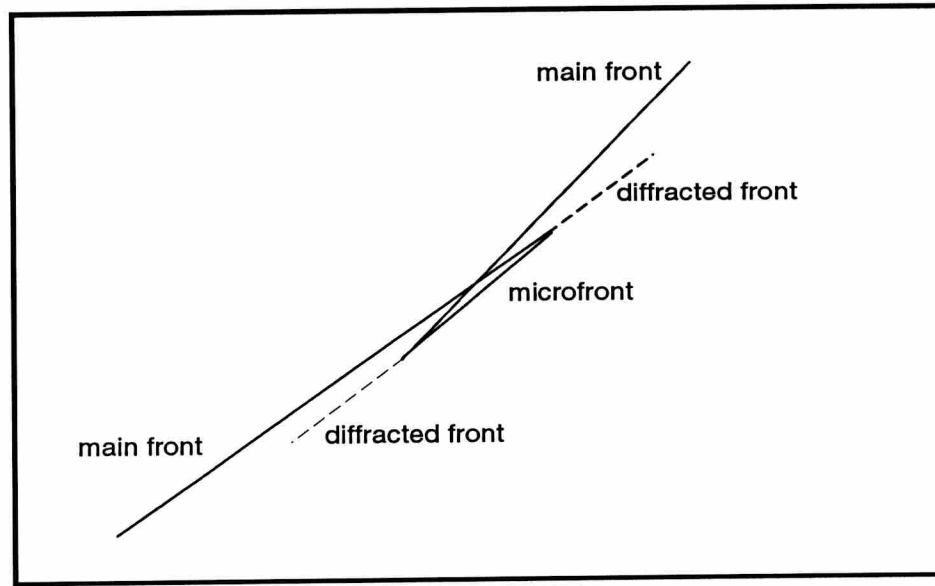
Figure 4.6: Illustration of an acoustic wavefront after focusing. A microfront is formed which is 90° lagging in phase relative to the main front. Diffracted fronts are formed extending from the caustic cusps of the microfront with phase lagging 45° relative to the main front.

As discussed and validated in Section 3.6, diffracted wavefronts extend from caustic cusps. These diffracted fronts are added as dashed lines to the sketch. The acoustic amplitude along the diffracted front decreases away from the caustic. Hydrophones located immediately exterior to the microfront will receive two distinct wavefront arrivals.

The greatest time-difference-of-arrival between the mainfront and the microfront is approximately 1.05 ms for a receiver at 1Mm receiving the vertically focussed reception described in Figure 4.4. This is 250 km of propagation after the initial focus. This time-difference of arrival corresponds to a time-domain phase difference contribution[1] of 0.09 cycles for the 75 hz signal described by Equation 1.2; thus, the micromultipath are unresolved and will appear as a single pulse with only a slight decrease in resolution, and the micromultipath time-difference-of-arrival is negligible. Since rays are traced independent of the source spectrum, the time-domain phase difference will scale linearly with acoustic frequency; so that, a 1 kHz source signal will have a time-domain phase difference of 1.05 cycles.

---

[1]The time-domain phase is composed of two components, traveltime and caustic phase.

In this case the micromultipath time-difference-of-arrival may be significant depending on the goal of the analysis. A more detailed study of micromultipath time-difference-of-arrival will be presented in Section 4.3.3.

The microfront has crossed one fewer caustics than the mainfront and for this reason the caustic phase <u>contribution</u> to the time-domain phase between the mainfront and microfront differ by 90° (0.25 cycles) independent of the acoustic frequency. The mainfront and the diffracted front differ by by 45° (0.125 cycles). For acoustic low frequencies, the caustic phase will be the predominant contribution to the difference in time-domain phase, and for high frequencies the micromultipath time-difference-of-arrival will dominate the difference in time-domain phase.

The ray endpoint density amplitude calculation method assumes a single plane wave reception. Strictly, the individual micromultipaths must be summed as vectors (magnitude and phase) to compute the aggregate amplitude and phase of the propagating front. This can be accomplished using the differential equation amplitude calculation method; however, this method requires two additional (50% more[2]) computations versus the ray endpoint density method. The approximate error expected in assuming a single plane wave reception will be analyzed using a simple model and computer simulation exercise.

Consider a mainfront-mainfront-microfront reception. Assuming the phase contribution due to the time-difference-of-arrival is negligible and the amplitudes of each arrival are equal, the micromultipath reception can be simply modeled using complex numbers by

$$1 + 1 + i = 2 + i \tag{4.6}$$

This reception has a power equal to 5 and a phase equal to 26.56°. If the caustic phase difference in the arrivals were ignored the reception would be modeled as $(1 + 1 + 1)$ and have a power of 9 and a phase equal to 0°. This represents an error of 2.55 dB in received power and 26.56° difference in received phase, where 26.56° is less than 0.075 cycles for a 75 hz signal. The 2.55 dB loss in power is termed the MicroMultipath Combining Loss or $MMCL$ and is the loss in power due to the destructive combining of the individual arrivals. If all micromultipath arrivals were precisely in phase, the $MMCL = 0$ dB. In following

---

[2] For 2D computational ocean models and 67% more computations for 3D models

studies, there is interest in power fluctuations greater than 10 and 20 dB so that an error on the order of 3 dB can be considered as negligible, and the ray endpoint density method can be used as long as the degree of accuracy discussed is attended. Please recall that the differential equation amplitude computation method identifies the individual arrivals (mainfronts and microfronts) and assigns the proper phasing; however, near caustics the amplitude calculation may be erroneously high as discussed in Chapter 3.
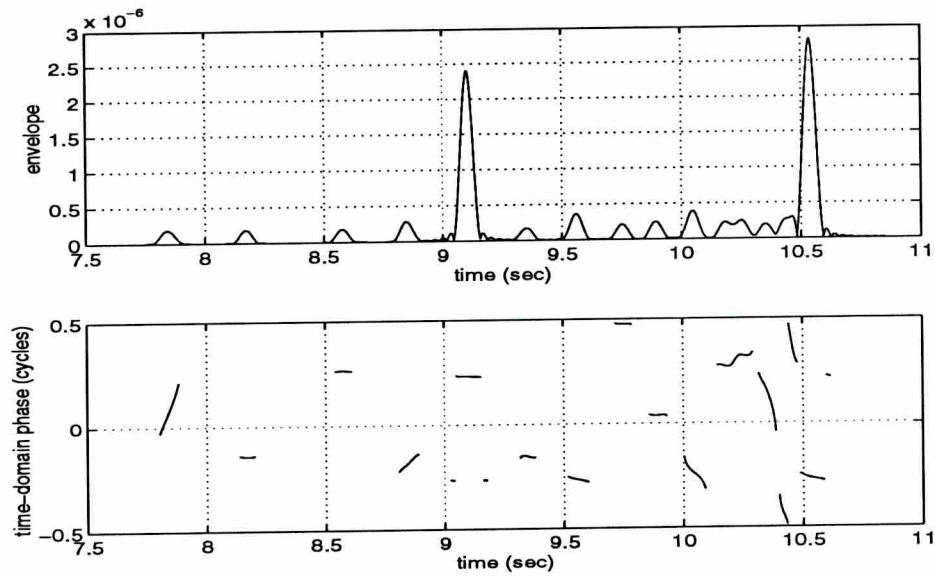
Figure 4.7: **The time-domain envelope and phase of an acoustic reception after 750 km propagation through a deep ocean computational model including a spatially synchronized internal wave.**

In Figure 4.7 the time-domain envelope and phase are shown for a reception of the early wavefront arrival at a depth of 1250 m and range of 748 km after propagation through the spatially synchronized internal wave computational ocean model discussed in the previous section. The strength of the internal wave has been doubled to enhance micromultipath generation. By viewing the time-domain envelope, the focused arrival is clearly visible after the time mark of 9 seconds. At this point, the absolute time-domain phase for this arrival is near 0.25 cycles. In Figure 4.8, the time-domain power and phase of the focused arrival (relative to an internal wave free reception) is shown for three-quarters of an hour, the period of the particular spatially synchronized internal wave included in the ocean model. The time-domain power and phase are computed using the ray endpoint density method

80
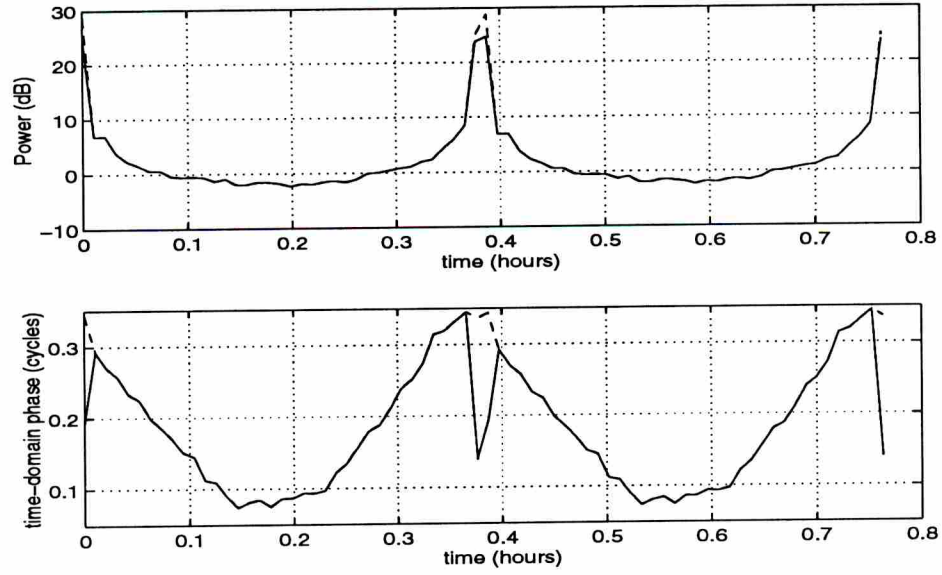
Figure 4.8: The time-domain power and phase of the received resolved arrival after 750 km propagation over one period of the single spatially synchronized internal wave included in the model.

(dashed line) and the differential equation method (solid line). The difference in power is approximately 3.5 dB at the peak, this is the only time the power calculations differ and also is the only time micromultipaths are present at the receiver. The time-domain phase differs at this time by as much as 0.18 cycles. These maximum errors in power and phase are on par with the approximate analysis previously discussed. For the case of analyzing amplitude fluctuation coincident with phase stability at a down-range receiver, the differences in the results obtained using the two amplitude calculation methods is not significant.

As the wavefront propagates several megameters the potential for continued microfront generation exists. Researchers have reported that the number of microfront arrivals increases exponentially and at some distant range the acoustic wavefront will be composed of a large number of arrivals[43]. This could result in a Rayleigh fading ocean channel; however, amplitude fluctuations would be accompanied by unstable time-domain phase.

4.2 3D spatial synchronization

In general, internal waves induce a sound-speed gradient normal to the direction of sound propagation. This will result in refraction of the ray paths out of the nominal acoustic

81
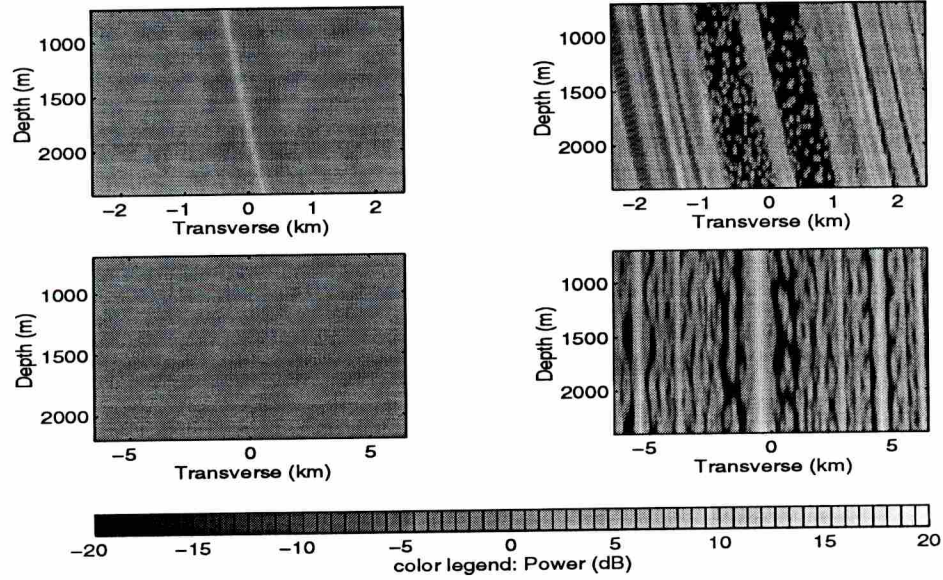
Figure 4.9: Induced power fluctuation on early arriving front. The 3D front has been projected into the YZ Plane. The legend indicates the received power ratio with and without internal waves. IW1 is used in the top figure, and IW2 is used in the bottom figures. N x 2D computations are used for the left side plots, and 3D computations are used for the right side plots. The N x 2-D model is not a reasonable approximation to the 3-D model when analyzing deterministic internal-wave induced received acoustic power fluctuation.

plane. The wavelength of the internal wave in the transverse direction is $2\pi/(k\sin\theta)$. If the ray deviates by $\pi/(k\sin\theta)$ in the transverse direction the internal-wave sound-speed perturbation has exactly the opposite polarity as the sound-speed perturbation used in the 2D computational model. For high wavenumber internal waves, $\pi/(k\sin\theta)$ can be as low as a few hundred meters. In the following sections, the internal-wave induced power fluctuation across the 3D early arriving front is studied.

4.2.1 N x 2D versus 3D computational ocean models

Figures 4.9, 4.10, and 4.11 look at rectangular portions of a sheet of a timefront to show the effect of internal waves on the received intensity. The situation and description of the plots will be described in detail for these figures.

The sound speed used is a range-invariant Munk profile, $c_{\text{Munk}}(z)$, with a single internal wave present. The traveltime is 504 seconds. Each plot is the result of propagating 150,000

rays using 300 vertical angles, α_o, between $-12.6°$ and $-12.0°$, and 500 horizontal angles, ψ_o, between $-0.5°$ and $+0.5°$. These 150,000 rays terminate on a timefront sheet at a range of about 748 km, extending approximately 2.3 km vertically at an angle of about 12.3° off vertical and propagating forward and downward.

Figure 4.9 uses gray-scale to indicate the fluctuation in received power caused by the presence of a single internal wave. Specifically it indicates the ratio of the received intensity with the internal wave relative to the received intensity without the internal wave using the ray endpoint density method. Light grays indicate increased intensity, and dark grays, reduced intensity. The midrange gray of 0 dB means the internal wave has caused no amplitude change. The gray scale is shown at the bottom of Figure 4.9.

Two different internal waves were used. Both internal waves are spatially synchronized for the 12.3° ray. IW1 caused the upper plots. IW2 caused the lower plots. The internal wave parameters and the reasons for selecting these specific internal waves will be explained while discussing the results.

Two different computational ocean models were used. Without internal waves these yield identical results. The plots to the right used full 3D computational ocean models and ray tracing. The plots to the left used 500 x 2D computational ocean models, meaning the ray leaving the source at each of the 500 horizontal angles was forced to stay at that angle by changing the transverse wavenumber to zero (called N x 2D in the literature where here N = 500).

IW1 is the same internal wave as used for Figure 4.4, where it demonstrated how an internal wave shows vertical focusing using a 2D computation. The upper left plot shows a fuller picture of vertical focusing using 500 x 2D computation. It shows the vertical focusing has a sharp depth sensitivity which shifts in the transverse direction with depth. The upper right plot shows the true focusing using 3D computation. The angling to the right with depth is parallel over the entire sheet. The central focusing seen in the 500 x 2D results are bordered by broad low-amplitude bands, and narrow high amplitude bands about 1.5 km either side of center.

IW2 is a first order $(j = 1)$ internal wave moving almost perpendicular to the acoustic propagation. The lower left N x 2D computation sees almost no internal wave effects. In

83

contrast, the lower right 3D computation shows parallel vertical banding amid a string-like structure of varying intensification and nulls. This is a phenomenon that will never be seen using a 2D or N x 2D computational ocean model, where acoustic rays are forced to remain in the nominal acoustic plane. This "transverse focusing" will be treated in the following section.

This section has demonstrated that 3D computations reveal intensification patterns that are, at best, only hinted at by the 2D and N x 2D computations. There has been no attempt at statistical computations using a stochastic ocean model, and it may well be true that some statistical intensity values based on 2D computations give insight to the values derived from 3D computations.

4.2.2 Transverse focusing

In the previous section it was demonstrated that the oscillatory shape of an internal wave across depth vertically focuses the acoustic rays. In the transverse direction, the change in sound speed, $\delta c(y)$, varies exactly sinusoidally for all internal waves as seen by Equation 2.5. Just as the cupped shape of the internal wave in the depth direction vertically focuses the acoustic rays, the sinusoidal shape of $\delta c(y)$ transversely focuses the acoustic rays. A spatially synchronized internal wave will significantly focus the sound transversely. Transverse focusing is typically a larger contributor to the redistribution of power across the front than vertical focusing.

Four examples of transverse focusing are demonstrated by including various spatially synchronized internal waves in the ocean model. The same early arrival investigated in the previous section is studied. For each example, the fluctuation in received power caused by the presence of the internal wave is displayed in Figure 4.10. A 3D computational ocean model is used for all cases.

Consider internal wave IW1. The internal wave propagation direction is set to $-77.5°$ to allow for spatial synchronization. The received power fluctuation results are shown in the top left plot of Figure 4.10. The presence of the internal wave increases the received power by more than 15 dB along a 100 m wide canted area on the timefront. Broad 400 m wide 15 dB fades are set parallel to either side of the focus area. A transverse shift of 100
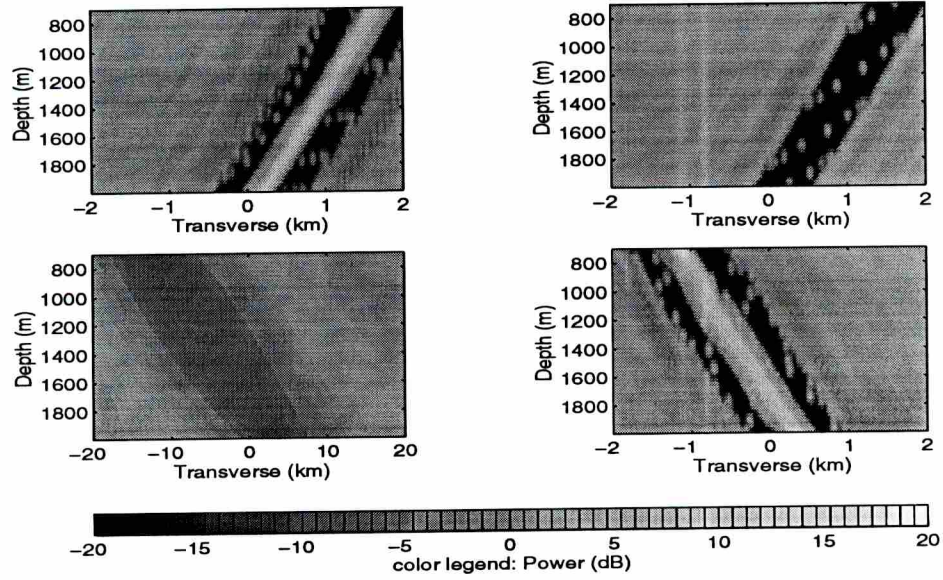
Figure 4.10: Induced power fluctuation on early arriving front. The 3D front has been projected into the YZ Plane. The legend indicates the received power ratio with and without internal waves. IW1 is used in the top two plots. The difference is the internal wave phase. IW3 is used in the bottom left plot. In the bottom right plot, IW1 is included in the ocean model as well as 6 additional internal waves that are not spatially synchronized to the arrival. For this plot, IW1 is propagating at $\theta = +77.5°$ as opposed to $\theta = -77.5°$. 3D computations are used for all plots. Each spatially synchronized internal wave significantly transversely focuses the received power on the arriving time-front.

meters in hydrophone placement could change the received power at this time instant by over 30 dB. The internal wave presents little impact to the received power for 1 km shifts away from the focus area. This is where the effective propagation angle no longer meets the spatial synchronization condition.

In Figure 4.10 the top right plot shows results from the same internal wave (IW1) used in the adjacent plot. Also the internal wave is traveling in the same direction with respect to acoustic propagation. The only change is that 23 minutes has passed equal to half of an internal-wave period (π/ω). The polarity of the internal wave induced change in sound speed is reversed, and the internal wave transversely defocuses the rays at the top-turning depth and the 15 dB increase in received power has been replaced by a 15 dB decrease in

85

received power.

Internal waves with large wavenumbers have the potential to have very short wavelengths in the transverse direction. This can cause very sharp and localized focusing. Low wavenumber internal waves can cause very broad focusing and defocusing. Consider an ocean model including IW3. The propagation direction angle is set to 85.6° to meet a spatial synchronization condition. The phase of the internal wave was set to defocus the acoustic rays. The power fluctuation caused by the internal wave across the front is shown in the bottom left plot in Figure 4.10. The plot covers 40 km transversely to show the broad defocusing. Internal waves with low wavenumbers have correspondingly low internal wave frequencies, ω. These broad focusing/defocusing internal waves can induce power gains/fades of several dB across an entire array that may last for hour-long periods. The width of the 10 dB power fade is almost 10 km wide.

Previously only a single internal wave was included in the ocean model. Spatially synchronized internal waves locally act on the 3D timefront to spatially redistribute power. When multiple internal waves are included in an ocean model, the set of internal waves generally act on the front as a composite of individual internal waves. No strong statement about linearity can be made, but the system is very well behaved in this manner. In the bottom right plot of Figure 4.10, the ocean model includes the seven internal waves listed in Table 2. Only IW1 is spatially synchronized. It is traveling at an angle $\theta = +77.5°$ relative to the nominal acoustic plane. Two points will be made from observing this plot. The acoustic rays are focused as if only IW1 is present. Also, the focusing is canted in the reflected and opposite direction as compared to the results of the top left plot in Figure 4.10 where IW1 is used with $\theta = -77.5°$.

In Figure 4.11 the top left plot shows the identical figure from the bottom right plot of Figure 4.10. In the top right plot, a $j = 4$ spatially synchronized internal wave traveling in the direction of the acoustic propagation is substituted for the spatially synchronized internal wave in the previously described multiple internal wave ocean model. This is the only case that 3D and N x 2D computational ocean models will yield similar results. The acoustic amplitude is intensified across a horizontal band.

In Figure 4.11 in the bottom left plot the two spatially synchronized internal waves
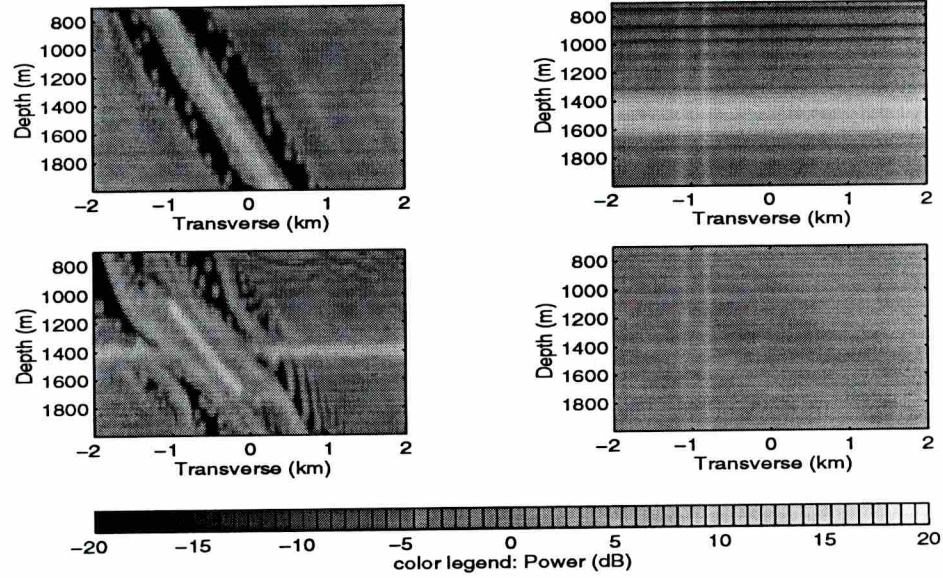
Figure 4.11: **Induced power fluctuation on early arriving front for four computational ocean models. The 3D front has been projected into the YZ Plane. The legend indicates the received power ratio with and without internal waves. In the top left plot, IW1 is included in the ocean model as well as 6 additional internal waves that are not spatially synchronized to the arrival. For this plot, IW1 is propagating at $\theta = +77.5°$. In the top right plot, a spatially synchronized internal wave traveling in the direction of acoustic propagation is included along with the identical 6 additional internal waves that are not spatially synchronized to the arrival. In the bottom left plot, the two spatially synchronized internal waves of the top plots are included along with the additional spatially non-synchronized internal waves. In the bottom right plot, only the 6 spatially non-synchronized internal waves are included in the ocean model.**

creating the top two plots are included in the ocean model along with the 6 additional spatially non-synchronized internal waves. In a gross sense, the amplitude distribution across the wavefront is a direct combination of the two intensification patterns caused by the spatially synchronized internal waves when included in the ocean model individually.

In Figure 4.11 in the bottom right plot, the two spatially synchronized internal waves are removed from the ocean model, leaving only the 6 spatially non-synchronized internal waves. The acoustic amplitude across the front is essentially unchanged after propagating through this internal wave field as indicated by the uniform gray level about 0 dB. This is

a general result realized after numerous computer simulations.

Since the amplitude focusing can be attributed to the spatially synchronized internal wave, and spatially non-synchronized internal waves create weak acoustic amplitude fluctuations, only the spatially synchronized internal waves within a full Garret-Munk internal wave spectrum need to be modeled to study the gross amplitude fluctuation of an early acoustic arrival. This means a 3D time varying computational ocean model can be used that is not exactly equivalent to the 3D time varying physical ocean model (Garret-Munk internal wave spectrum of internal waves) but may adequately represent it for certain investigative purposes.

4.2.3 Micromultipath combining loss

After propagation through an internal-wave field, the 3D timefront forms a thin sheet. Computation of the micromultipath combining loss (MMCL) shows instantaneous power losses less than 3 dB with respect to a 75 Hz signal at a 750 km range. The MMCL is a measure of the power loss resulting from internal-wave induced breaking of the wavefront into multiple arrivals (called micromultipath) which differ in phase and thus combine to some degree destructively[3]. For this research, internal-wave induced micromultipath is not a significant contributor to the power fluctuations, and the primary component of the fluctuations is a result of coherent focusing and defocusing. The $MMCL$ increases with propagation range, acoustic frequency, and internal-wave magnitudes $\mid G \mid$; thus, for other scenarios the $MMCL$ may be a dominating factor and could lead to unstable time-domain phase.

Traveltime separation of micromultipaths can blur the resolution of the propagating wavefront; however, simulation results show that maximum time separation of micromultipaths is negligible for all cases studied. In Figure 4.12 a histogram has been compiled for the maximum time separation (labeled in cycles with respect to a 75 hz acoustic signal) between micromultipaths for various receiver locations in the XY plane for the early arrival studied at a range of 750 km. Ten different internal wave models are included where up to

---

[3]For this study the phase difference is dominated by a differing number of caustics crossed by different microrays

88
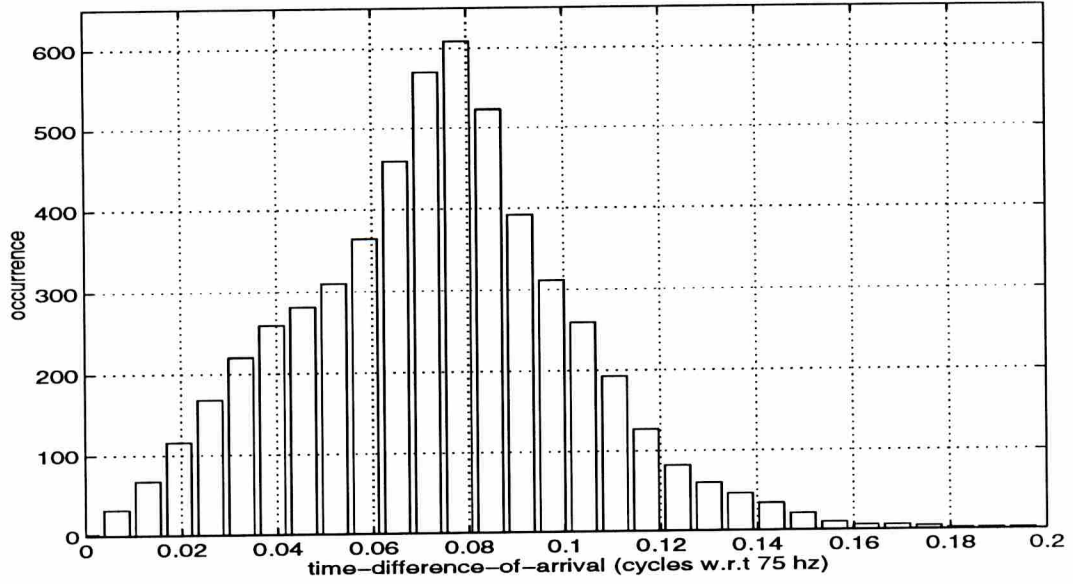
Figure 4.12: **Histogram of the maximum time-difference-of-arrival spread when micromultipath is present for ten different ocean models. This time spread is plotted in terms of cycles with respect to a 75 hz acoustic signal. The total number of occurrences is 5538 to form the histogram. The maximum time-spread does not exceed 3 ms or .225 cycles.**

20 internal waves were included in the ocean model and up to three of the internal waves were configured to be spatially synchronized with the arrival.

The main message is that for low-frequency acoustic signals, the amplitude fluctuation can be significant while the time-domain phase remains stable **and** the wavefront remains effectively a single plane wave sheet. The time-difference-of-arrival will scale linearly with acoustic frequency and higher acoustic frequency signals would not necessarily remain this stable.

4.3   Time-varying 3D computational ocean models

In this section, the time-domain phase and received power at a hydrophone(s) as a function of time is analyzed. The same early arrival, studied in the previous sections, is investigated. It will be demonstrated that the time-domain phase can remain relatively stable while the received power fluctuates widely both spatially and temporally. At a single hydrophone, the received amplitude distribution may appear to be Rayleigh distributed
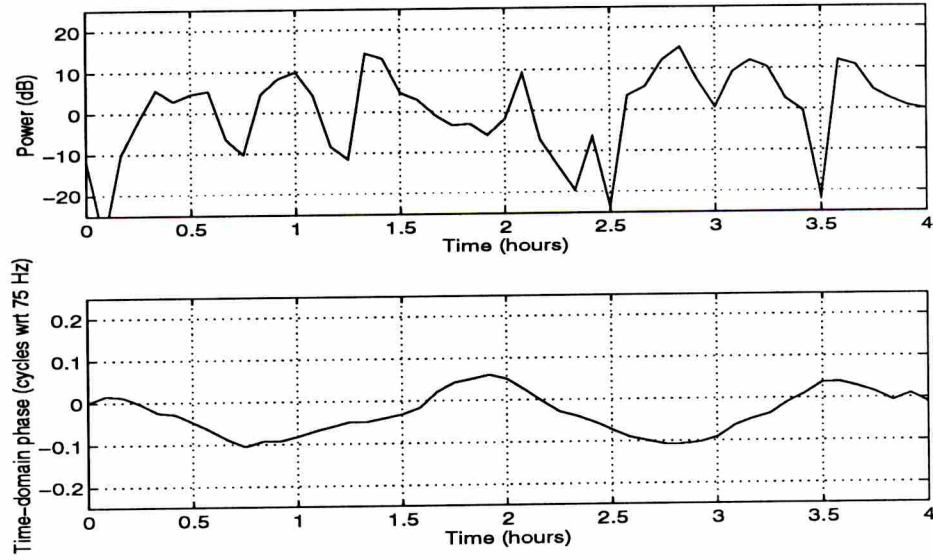
Figure 4.13: Top: Power as a function of time for early arrival at a range of 750 km, depth of 1200 m, and transverse coordinate of 0 m. Bottom: Time-domain phase for same early arrival.

while the time-domain phase is relatively stable.

The ocean model includes the seven internal waves in Table 4.1. IW1 and IW2 are spatially synchronized to the acoustic arrival propagating at angles $\theta = 77.5°$ and $89.2°$, respectively. The magnitude of the maximum change in sound speed induced by the internal-wave field is less than 0.5 m/s.

4.3.1 Rayleigh fading stable phase

The received time-domain power and phase of an arrival at the range of 750 km, depth of 1200 m and 0 m transverse shift is computed every 5 minutes over a four hour period and shown in Figure 4.13. The received power fluctuations spread over 30 dB. The time-domain phase oscillates with a peak-to-peak deviation of 0.18 cycles referenced to a 75 Hz center frequency. This would impose no limitation on coherent integration.

The intensity level[4] at a candidate receiver site is considered as proportional to the local ray endpoint density on the timefront sheet as described in Chapter 3. The intensity histogram is computed for several receiver locations distributed across the timefront over

---

[4]The intensity level is an absolute measure in contrast to a referenced measure such as power measurements in dB.

90
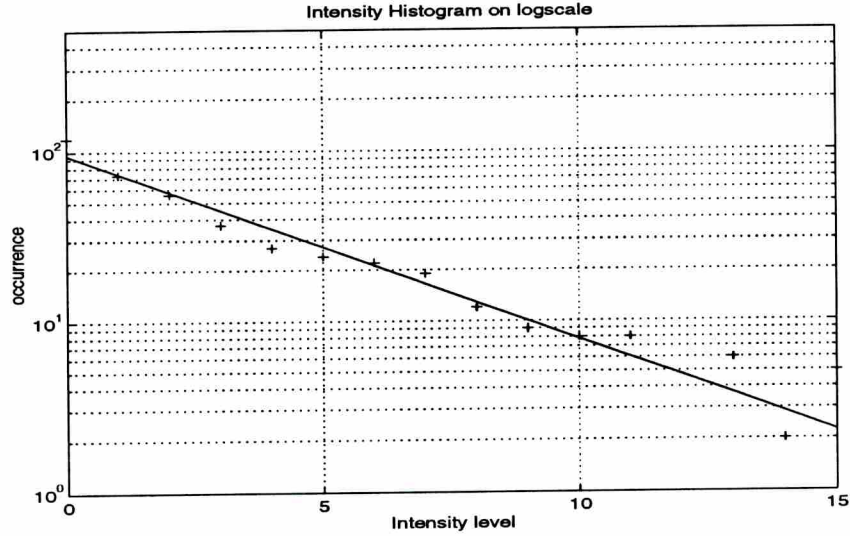
Figure 4.14: Intensity histogram of early acoustic reception after long range propagation through multiple internal wave fields. The data are plotted on log-scale to show comparison with exponential distribution (straight line), which is equivalent to a Rayleigh amplitude distribution.

the four hour period. The histograms from the sample receiver locations are averaged and the resulting histogram is shown in Figure 4.14. The intensity histogram is approximately exponential (linear on a log scale) which is consistent with Rayleigh amplitude fading. There is no underlying stochastic process forcing the amplitude distribution to be Rayleigh, it just happens to be similar. Here we show through deterministic modeling that internal waves can cause the received amplitude to mimic Rayleigh fading while maintaining stable time-domain phase.

4.3.2 Vertical and horizontal line arrays

In Figure 4.15, the received power and time-domain phase of an early arrival at three hydrophones (in the configuration consistent with a horizontal array) at a depth of 1500 meters, range of 750 km, and transverse coordinates of -300, -150, and 0 meters are plotted. The power fluctuates over 30 dB at each hydrophone. At a given time, the received power at two hydrophones with 150 meter separation can differ by over 20 dB. Clearly, for a horizontal array, we cannot expect the arrival to be an equal amplitude plane wave across
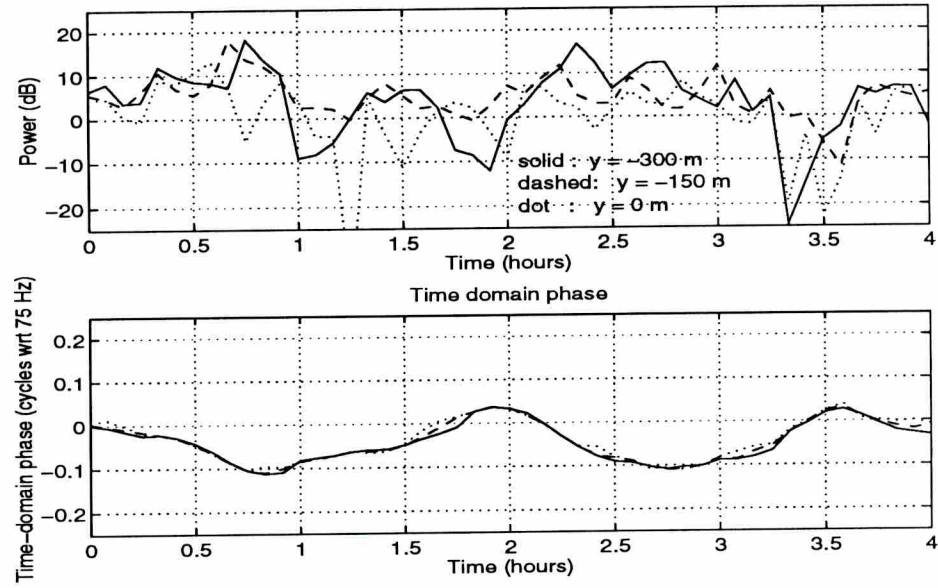
Figure 4.15: Horizontal array- Top: Power as a function of time for hydrophones at range of 0.75 Mm, depth of 1500 m, and transverse coordinates of -300 m, -150 m, and 0 m. Bottom: Time-domain phase for same three receptions.

all hydrophones. The time-domain phase at the three hydrophones is very similar, and beamforming algorithms based on plane-wave receptions would be expected to be successful.

Similar results are obtained for hydrophones aligned in a vertical orientation. In Figure 4.16 shows the received time-domain power and phase of an early arrival at three hydrophones at a range of 750 km and depth coordinates 1300, 1450, and 1600 meters. The power fluctuates well over 30 dB at each hydrophone, and at a given time, the received power at two hydrophones with 150 meter separation can differ by over 20 dB. The time-domain phase of each reception has been adjusted to remove the time-differences of arrival due to the inclination of the received front. The time-domain phase of the front is very similar. Once again, this allows the use of plane-wave beamforming techniques to determine the angle-of-arrival of each wavefront and coherently (spatially) integrate the reception along the vertical array.

The general oscillation of the time-domain phase is consistent with one of the internal wave modes that is not spatially synchronized. The primary oscillation occurs at approximately 0.5 cycles per hour which is consistent with IW6 which has an internal wave frequency of 0.53 cycles per hour.
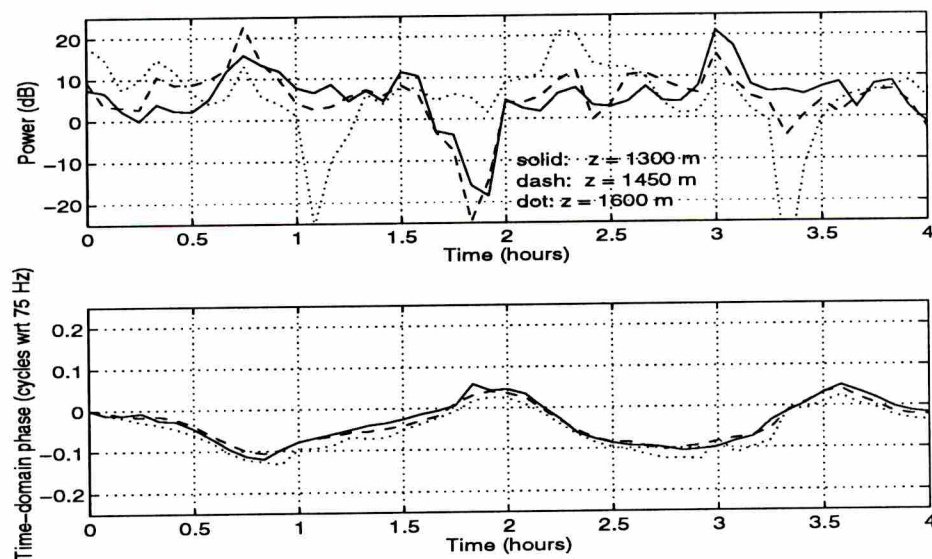
Figure 4.16: **Vertical array - Top: Power as a function of time for hydrophones at range of 0.75 Mm, depths of 1300, 1450 and 1600 meters Bottom: Time-domain phase for same three receptions. The time difference of arrival due to the inclination of the front has been removed from the phase information.**

4.4 Comparisons with experimental data

Many long range sound propagation experiments have been conducted over the last 35 years. The acoustic signal is typically received at a horizontal or vertical array. The acoustic signals at each array element (hydrophone) are combined (beamformed) to increase the received signal energy. Therefore, the signal energy is accumulated by integrating over time (matched filtering and coherent integration) and space (beamforming). Most engineers and scientists studying acoustic propagation work with the matched filtered and beamformed data. Because the University of Michigan has played a predominate role in the collection and processing of the acoustic data, researchers from this University are familiar with the character of the received time-domain amplitude and phase of the acoustic signal across the hydrophones. The most general observation is that the acoustic time-domain amplitude of a resolved arrival is significantly less stable than the time-domain phase in two senses: 1) on a hydrophone by hydrophone basis for a fixed time and 2) over time on any given hydrophone. The physical cause of these observations was previously unexplained. From

the data presented it is feasible that these previously unexplained observations can be the result of the presence of internal waves within the propagation path. Figures 4.14, 4.15, and 4.16 are model examples of this result.

The instability of time-domain phase has been largely contributed to fluctuating ocean processes[5]. However, the acoustic signals have been transmitted and/or received from moving platforms inducing acoustic phase instability. During the Heard Island Feasibility Test[5], the source ($f_c = 57hz$) was located on a moving ship and the acoustic signal was received 9.21 megameters away on a rigidly moored array of hydrophones as well as many other receiver stations located around the earth's oceans. The time-domain phase of the reception was used to monitor precise changes in traveltime of the acoustic signal[44]. The unwrapped change in time-domain phase weighted by the acoustic wavelength is equal to the distance trajectory of the ship. The precise motion of the ship was tracked using acoustic phase estimates and confirmed using GPS[6] readings taken on the ship during acoustic transmission. The two estimated courses of the ship extraordinarily agreed within a few meters[42]. A few meter error is on par with the accuracy of the GPS readings so that it is not clear if tracking the ship location using low frequency acoustics over 9 Mm away is less accurate than using GPS! **Any instability in the acoustic phase induced by fluctuating ocean processes, such as internal waves, would have corrupted the acoustic estimates of the ship trajectory. This is the ultimate illustration of the phase stability of the global ocean for low-frequency acoustic signals.**

Previously suggested ocean models do not cause early acoustic arrivals to have fluctuating amplitude coincident with stable time-domain phase. The ocean models presented in this work are the first to be based on fundamental physical principles and be in agreement with this long standing and previously unexplained observation of long range acoustic receptions.

---

[5]The Heard Island Feasibility Test was a long range acoustic propagation experiment conducted to determine if sound could be transmitted and detected over global distances with sufficient accuracy to detect global climate variability.[42]

[6]Global Positioning System (GPS) is a satellite based location system

4.5 Internal wave mode identification

Measurement of deep ocean internal wave fields is a difficult task, and only a few incomplete measurements have been made[21]. The most common method is to measure the ocean temperature at a fixed depth from a rigidly moored platform. Measured variations in temperature relate to variations in density. The displacement of an isodensty parcel of water is a measure of the internal wave (as well as every other ocean process such as tidal and eddy processes) as it propagates past the measurement point. This was described in Section 2.1.2. A time series of the density variation can be analyzed to separate the relatively long time scale tidal and eddy effects and short time scale internal wave effects.

It would be desirable to study the internal wave field using an acoustic interrogation signal. This would allow more global measurements and a more versatile monitoring system. This problem has been investigated in [52] based on fluctuations in acoustic traveltime (phase). The emphasis in this treatment is on the acoustic amplitude[7]. The observables of the acoustic reception are the acoustic time-domain amplitude and phase at any number of receiving hydrophones. It is assumed that we are monitoring the early, resolved acoustic wavefront arrivals. Examples of time series of these observables are plotted in Figures 4.15 and 4.16.

It has been long conjectured that internal waves in the Pacific Ocean basin travel in all directions based on the large roughly circular shape of this ocean's coastal boundaries. The internal waves, excited perhaps from tidal forces on coastal topography, are launched propagating toward the ocean center. Thus, in the middle of the deep ocean, internal waves are hypothesized to be propagating with no favor to direction. However, the Atlantic Ocean basin is small and narrow on global scales and internal waves generated from coastal topography are conjectured to favor east-west directivity. In this section, a method is described to acoustically measure the propagation direction of spatially synchronized internal waves based on spatially diverse amplitude measurements of a single acoustic wavefront.

[7]From an information view point, it is clear that we would want to analyze the complete reception (all arrivals and amplitude and phase), we focus on amplitude to employ previous results in this dissertation.

4.5.1 Sampling of the internal wave field

Based on the results previously presented in this chapter, spatially synchronized internal waves will significantly impact the received acoustic amplitude. Our interest is in the resolved wavefronts such that amplitude measurements sampled across a single wavefront can be estimated. Each early wavefront arrival corresponds to a ray which has traveled through the deep ocean in an oscillatory manner, refracting away from the ocean surface and ocean bottom, as can be seen in Figure 3.1. It is fair to assume the internal wave's impact on the acoustic ray is limited to the ray's top-turning points as described in Section 4.1.2. A single arrival has spatially sampled the internal wave field at a fixed period, the ray's acoustic path cycle length as described by Equation 4.4. Additionally, the ray's top-turning depth remains constant. This means that each ray's acoustic amplitude fluctuation results from a very spatially precise interrogation of the internal wave field (a set acoustic path cycle length and top-turning depth). Each resolved arrival yields a different interrogation because each resolved arrival corresponds to a ray path with a different acoustic path cycle length and top-turning depth combination. Figure 4.17 shows the cycle-length and depth combination sampled by early acoustic arriving wavefronts. The solid line and dashed line correspond to rays propagated through the sound speed profiles plotted (same dashed, solid convention) in Figure 2.1. The earliest arriving wavefront travels closest to the ocean surface (shallower top-turning depth) and has a larger acoustic path cycle length.

The actual arrivals will sample the curve of Figure 4.17 differently depending on the source and receiver depths. Longer ranges and/or multiple receiving hydrophones will more finely sample the curve resulting in increased interrogation, but the ocean cannot be investigated using an acoustic signal and received amplitude information for internal waves at depths and cycles lengths off of these curves. The curves are completely described by the sound-speed profile. The spatially synchronized internal waves that will potentially impact the received acoustic amplitude have wavenumbers and propagation directions consistent with the condition of Equation 4.5. Rays with launch angles of equal magnitude (*e.g.* $\alpha_o = +15°$ and $-15°$) will have identical acoustic path cycle lengths and top-turning depths but for any observation time will be spatially sampling the internal wave field at a different
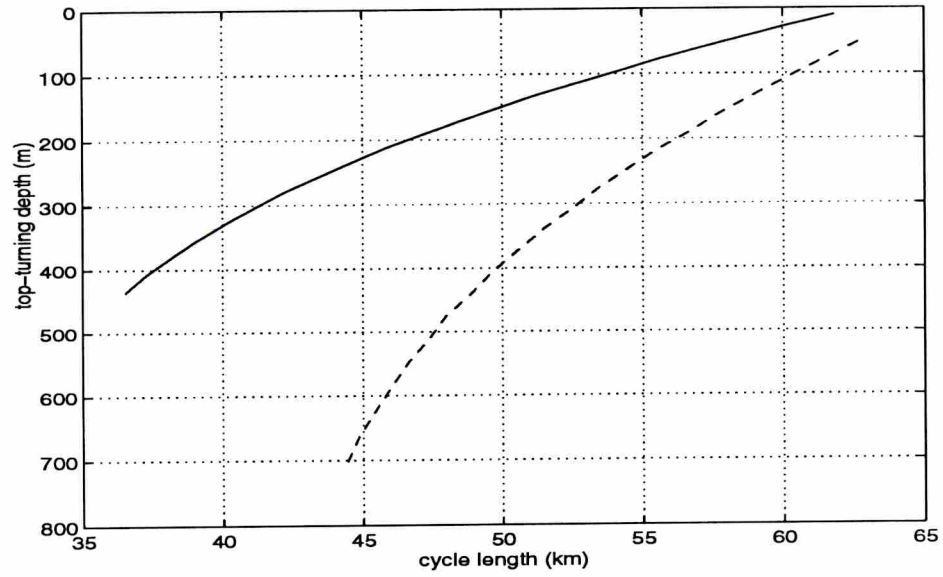
Figure 4.17: Each curve represents the acoustic path cycle length and top-turning depth combination in which the acoustic wavefront can interrogate spatially synchronized internal waves. The curves are solely a function of the sound speed profile used to describe the deep ocean waveguide. The dashed curve represents $c_{\mathrm{Munk}}(z)$, and the solid curve represents $c_{\mathrm{S89}}(z)$

spatial phase.

CHAPTER 5

Summary of contribution & future work

In this chapter, the motivation for the work is reviewed and the original contribution to the field of underwater acoustic signal processing and modeling is summarized. Also, areas of future work are outlined.

5.1 Review of motivation

Researchers have been interested in the effects of deep ocean internal waves on long range acoustic propagation for decades. The end users of long range acoustic propagation experiments are climatologists, oceanographers, and Naval forces, each having different reasons for their interest. Currently, climatologists are interested in using thermometry data collected from the ATOC (Acoustic Thermometry of Ocean Climates) project for incorporation into global ocean climate models. The U.S. Navy is interested in the effects of internal waves on both active and passive sonar systems.

To properly study the effects of long range acoustic propagation through internal wave fields an appropriate ocean model must be established. The establishment of such a model and the validation of the model is the hallmark result of this dissertation. With such an acoustic propagation model established, researchers armed with relatively inexpensive computer workstations can study the effects of internal waves within their particular ocean acoustic system of interest and develop signal processing algorithms that are robust to the presence of internal waves. This can be conducted in lieu of expensive field experiments for introductory system development.

5.2 Summary of contribution

A 3D time-varying deep ocean model suitable for simulating long range acoustic propagation has been established and validated. The model includes two dominate effects on acoustic propagation: the deep ocean waveguide and propagating internal wave fields. The model is based on fundamental physical principles.

This is the first ocean model which exhibits a fundamental observation of received acoustic signals which have propagated long ranges through the deep ocean, namely the received signal has large time-domain amplitude fluctuation coincident with stable time-domain phase. The amplitude fluctuations have been reported to be Rayleigh distributed, and it has been shown that internal waves are capable of creating a Rayleigh-like fading amplitude coincident with stable time-domain phase. For example, the received power attributed to an early arrival propagated over a 750 km range can fluctuate over 40 dB while the time-domain phase remains within a quarter of a 75-Hz cycle.

The specific mechanism of the internal wave field causing the received acoustic signal to have a Rayleigh-like amplitude fluctuation coincident with stable time-domain phase is explained in detail leading to the demonstration that spatially synchronized internal waves significantly impact the received acoustic amplitude while spatially non-synchronized internal waves do not significantly impact the received acoustic amplitude.

Ray tracing was used to simulate acoustic propagation through the ocean model and a method of simulating low frequency broadband acoustic propagation over long ranges was developed and validated against exact solutions to the wave equation. These exact solutions, however, have limited versatility and cannot be used in space and time varying ocean models. Establishing an accurate ray tracing based simulation method for low-frequency, broadband acoustic propagation is significant because it combines the computational efficiency and extension to 3D time-varying ocean models of ray tracing while still accurately modeling low-frequency broadband acoustic propagation. Two methods were independently derived to compute the acoustic amplitude after propagation through a 3D ocean model and compared. Each method is appropriate under separate conditions. Under most conditions these methods compute essentially identical results. The validation led to a study

of acoustic diffraction effects caused by the deep ocean waveguide. A method to model diffracted acoustic energy using ray based methods was presented. This method allows one to decompose the received acoustic field in terms of wavefront arrivals. This attribute is unique to this method.

This work calls for the research community to use 3D computational ocean models and 3D propagation methods. It is demonstrated that the standard 2D ocean models used currently for studying long range acoustic propagation yield erroneous results; that is, predicted received amplitudes can be in error in excess of 40 dB. A subtle contribution of this work is the demonstration that one must clearly define the physical ocean model under investigation and understand the penalties incurred by changing this ocean model to a computational ocean model for computer implementation.

The deep ocean internal wave model presented is used to produce several additional introductory results including: measures of micromultipath combining loss and coherent integration loss to establish functional range limitations on long range acoustic propagation.

5.3   Future work

The nature of the research presented was exploratory. Many "side studies" were given a preliminary investigation, and from this work a collection of open problems in underwater acoustic signal processing and modeling was spawned, accompanied by initial insight.

5.3.1   Internal wave imposed limitations on acoustic receptions

In the previous sections, it has been demonstrated that internal waves can cause the received acoustic amplitude to fluctuate coincident with relatively stable time-domain phase. For the ranges, internal wave strengths, and acoustic frequencies studied, the amplitude fluctuation is the result of acoustic ray focusing and defocusing and not the result of destructive and constructive interference of multiple arrivals. For greater ranges, stronger internal wave fields, and/or higher acoustic frequencies, many factors could cause the received acoustic wavefront to be undetectable and not provide sufficient energy for estimation of amplitude and traveltime.

It is important to understand the relations between range, internal wave field strength,

acoustic frequency, and receiver coherent integration time for the design of successful underwater acoustic propagation experiments. This issue is currently important to the U.S. Navy for performance evaluation and design of both active (high-frequency) sonar systems and passive systems. This issue is currently important to long-range low-frequency acoustic propagation experimentalists, where current models predict an internal wave imposed range curtain near 3 Mm at acoustic frequencies where acoustic propagation over 10 Mm has been demonstrated successfully.

How do internal waves impact detection and estimation of acoustic receptions after propagation through an internal wave field as a function of internal wave field parameters, ocean waveguide parameters, range, acoustic frequency, integration time, receiving array geometry, and acoustic waveform design?

To offer initial insight into this problem, the components contributing to a loss of acoustic energy are described. There are four mechanisms that cause increased acoustic attenuation as range increases after propagation through the deep ocean. These mechanisms are absorption, geometric spreading, micromultipath combining loss (MMCL) and coherent integration loss (CIL). Table 5.1 summarizes these loss mechanisms as a function of range, acoustic frequency, and internal wave field strength.

	range	frequency	internal wave strength
absorption loss	$\Uparrow$ linearly	$\Uparrow$ exponentially in dB	independent
geometric spreading loss	$\Uparrow$ linearly	independent	independent
MMCL	$\Uparrow$ linearly	$\Uparrow$ linearly	$\Uparrow$ linearly
CIL	$\Uparrow$ linearly	$\Uparrow$ linearly	$\Uparrow$ linearly

Table 5.1: Loss mechanisms; $\Uparrow$ = *increases*

We are interested in loss mechanisms imposed by the internal wave field; moreover, we are interested in **dynamic** loss mechanisms imposed by the internal wave field. Any static losses, such as absorption, geometric spreading, and possibly MMCL can be recouped via increased coherent integration time. With respect to long-range acoustic propagation, ocean properties do not change with time scales of seconds or minutes, but hours days and years.

If coherent integration loss is the only catastrophic loss mechanism, then a simple loss model is worth investigating and expanding. Coherent integration loss is due to the fluctu-

ation of the time-domain phase of the resultant wavefront during coherent integration. It is assumed that sufficient energy cannot be accumulated to track the changes in the time-domain phase and subsequently correct the phase to aid in coherent integration. Assuming the received time-domain phase linearly sweeps across a fraction of the center-frequency cycle and the acoustic amplitude is stable within this time frame. The coherent integration gain[1] can be represented by the sinc function, where the peak of the sinc represents no loss and absolute phase stability and the first null represents complete loss of acoustic energy where the phase has swept exactly through one acoustic cycle resulting in complete cancelation. Figure 5.1 shows the coherent integration loss. Two observations are that the time-domain phase can fluctuate and result in little loss, but if the time-domain phase sweeps near or over a full cycle great losses are incurred. Also, in the case of large time-domain phase sweeps, this measure can no longer be used to estimate arrival times, and one must result to methods based on peak picking the received acoustic envelope.
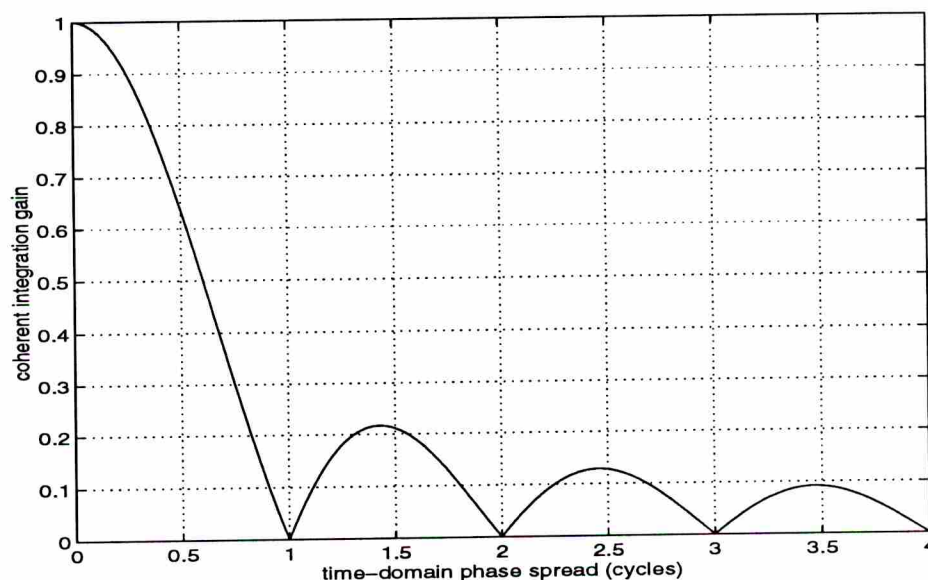
Figure 5.1: Coherent integration gain as a function of time-domain phase spread.

What causes an increase in the sweep rate of the time-domain phase? If the transmitter

---

[1]The coherent integration gain is valued between 0 and 1, where 1 relates to "no loss" and 0 relates to "complete loss" in the energy of the received and processed signal. Coherent integration loss is the reciprocal of the coherent integration gain.

and receiver are rigidly moored, one can assume this is due to the fluctuations of the internal wave field. From results in this work, the acoustic propagation can be fairly modeled using ray tracing; thus, changes in time-domain phase were directly the result of changes in traveltime scaled by the acoustic center frequency. We are assuming caustic phase changes are not an issue. Also, we have seen in preliminary studies that the time-domain phase sweep rate is linearly related to the internal wave field strength and range. Therefore, it is reasonable to suggest that the abscissa of Figure 5.1 may be **range** × **internal wave strength** ÷ **acoustic frequency**. This is the beginning of relating these quantities in a physically based manner that would aid in the design of many acoustic experiments and underwater acoustic equipment.

5.3.2 Normal-mode domain versus ray domain

One of the previously unstated motivating factors for the work presented in this dissertation is to make acoustic signal processors aware that simple stochastic models[2] do not fairly represent the ocean acoustic channel. Thus, signal processing algorithms based on these models have little hope of being "optimal" in any sense.

There is no description of the acoustic reception which exactly describes it. The two descriptions typically used are rays and modes. Rays represent the acoustic energy in terms of attenuated, delayed, and phase shifted replicas of the transmitted signal. Modes represent the the acoustic energy in terms of horizontally propagating modes decomposed in frequency and mode number.

When signal processors initiate the development of an algorithm, regardless of the goal, they enter one framework and not the other: rays or modes. For the purposes of long-range acoustic propagation through range-invariant oceans, ray and mode modeling can be seen as equivalent as unveiled in this thesis. However after propagation through an internal wave field, it is not immediately clear which decomposition of the acoustic arrival (rays or modes) is more robust. This thesis studied internal wave induced fluctuations of early acoustic arrivals and found that their time-domain amplitude fluctuates coincident with relatively stable time-domain phase. These early wavefront arrivals correspond to the higher-order

---

[2]Such as describing the channel as a Rayleigh slow fading channel.

normal modes. There is no guarantee, and a matter of fact it is not expected, that the terminal ray arrivals maintain stable time-domain phase after propagation through internal waves. However, the normal mode arrivals may be a more stable decomposition of the reception. It has gone without saying that in most signal processing algorithms, amplitude variations are typically tolerable, while phase variations are typically not tolerable.

An open research question is "Are acoustic normal modes or ray arrivals more robust to internal wave effects with respect to the success of signal processing algorithms based each method."

5.3.3 Internal wave propagation direction

As discussed in Chapter 4, internal wave modes that are spatially synchronized to the acoustic arrival have the potential to strongly influence the received acoustic amplitude. Other internal wave modes have been found to insignificantly impact the received amplitude.

By modeling long-range sound propagation through a single internal wave, we have discovered that spatially synchronized internal waves cause canted areas of power gains and fades spatially across the propagating acoustic front. Since an internal wave is synchronized with respect to a specific arrival's acoustic cycle length, different arrivals will interrogate the ocean with different cycle lengths. Studying all resolvable arrivals may yield the internal waves' direction of propagation in the ocean. To begin in this direction, we observe that the cant of the transverse focusing area is solely a function of the internal-wave propagation direction angle, θ. For cases when a spatially synchronized internal wave is traveling near normal to the direction of acoustic propagation the focusing pattern is nearly vertical. This is seen in the lower right plot of Figure 4.9. Other plots in Figures 4.9, 4.10, and 4.11 show evidence that the cant angle of the focus area is related to the internal wave propagation direction.

Since the canting angle will most likely need to be measured from a 2D array of hydrophones in the YZ, Δx is not a measurable quantity. Relating Δx to a measurable quantity Δz, where $\Delta z / \Delta y$ is the slope of the focused acoustic energy canting angle in the projected YZ plane is highly dependent on the sound speed profile. However, the relation between ΔX and Δz is monotone and this method can be used to roughly asses the

direction of spatially synchronized internal wave propagation. When the internal wave is propagating nearly normal to the nominal acoustic direction, the focusing or defocusing is nearly vertical in the YZ plane as example in the bottom right plot of Figure 4.9. When the internal wave is propagating in approximately the same direction as the acoustic signal the focusing is the vertical direction as example in top right plot of Figure 4.11. It is believed that these methods could be used in the Atlantic to determine if internal waves have a preferred direction of propagation by transmitting sound parallel or orthogonal to a coastal boundary.

The community has only recently moved to vertical arrays, but it appears inevitable receiving arrays will be composed of 2D or 3D grids of hydrophones. A detailed study of the cant angle relation to specific spatially synchronized internal wave parameters maybe reasonably timed with future multi-dimensional array experiments.

5.3.4   Stochastic computational ocean model

The research presented in this dissertation studied the deterministic impact of internal wave modes. For many reasons, it would be of interest to model the internal wave field as a random field. By generating realizations of the random field and simulating acoustic propagation through the realized field using the methods described in this dissertation, Monte-Carlo simulations could be run to gather sample statistics and statistically describe acoustic propagation through internal waves.

One way to compose a stochastic realization of the internal wave field is to generate the 4D (x, y, z, t) internal wave induced change in sound speed using a 4D innovation sequence and a 4D filter whose parameters describe the physical parameters of the internal wave field. This method was implemented on a modern computer workstation. Three-dimensional propagation of an early arriving acoustic ray over a 500 km path and two-hour time period was simulated for various internal wave strengths. This simple simulation took 8 days of dedicated computer time. The result, although grandly inconclusive, was to achieve acoustic amplitude fluctuation the internal wave field strength had to be increased to the point that acoustic time-domain phase instability was incurred. A more thorough investigation of modeling random internal wave fields is an open problem and would receive great interest

from the current research community.

5.3.5   Range-variant model benchmarking

In Section 3.7 is was illustrated that the leading propagation methods yield significantly different simulated received acoustic signals after propagation through internal-wave fields. In Chapter 4, it was demonstrated that it is necessary that 3D computational ocean models be used to accurately simulate acoustic propagation through internal wave fields. In this work, we established agreement in ray and normal mode propagation methods for 2D long-range deep ocean (range-invariant) ocean models. It is important to establish such a benchmarking report for 3D range-variant computational ocean models. Just as for the 2D range-variant case presented in this dissertation, the strengths and weaknesses of the different propagation methods will be uncovered and possible modifications to existing propagation methods will be developed and/or new propagation methods will be derived, addressing the specific short comings of existing methods.

APPENDICES

APPENDIX A

Normal mode propagation method

The purpose of this appendix is to discuss the validity of the normal mode solution of the wave equation for 2D long-range, range-invariant, deep-ocean sound speed profiles (Equation 3.1). The *validity* is discussed by classifying the normal mode functions and discussing their contribution to long range acoustic receptions. The classification procedure leads to a ray interpretation of bound modes, which the author believes is enlightening without claiming that it is strictly novel.

The normal mode solution is referred to as a "ground truth" solution because it solves the wave equation exactly for 2D range invariant models, under the assumptions that the acoustic signal is a separable function in range and depth, and the source is a point source[16][38]. Two additional assumptions are required for standard implementation, namely the Hankel function power series is approximated by a complex exponential function, and only a finite number of the uncountably infinite number of normal modes are used. Since the goal is to maintain a ground truth solution without representation of all modes, it is of interest to classify the modes to help determine which modes are most significant for simulating long-range deep-ocean acoustic propagation.

A.1 Mode classification

Two classes[1] of normal modes are *evanescent* modes and *bound* modes. Evanescent modes have complex wavenumbers; therefore, these modes are attenuated as a function of range at a rate greater than cylindrical spreading. Bound modes are attenuated solely by

---

[1] The word *classes* is used to mean groups that are mutually exclusive and as an aggregate complete.

cylindrical spreading. These modes have (positive) real wavenumbers.

Another two classes of normal modes are *continuous* modes and *discrete* modes. There is an uncountably infinite number of modes whose wavenumbers are described on a continuous path through complex wavenumber space[2]. These are the continuous modes. It is assumed that all continuous modes have complex wavenumbers and are completely members of the evanescent modal class. There is a countably infinite number of discrete modes. These modes have wavenumbers which are both purely real and complex.

The bound modes have real discrete wavenumbers. The bound modes can be categorized into two classes: *reflected* modes and *refracted* modes. These terms are taken from ray theory. Reflected modes correspond to modes which interact with the ocean boundaries (surface and/or bottom) and hence correspond to rays which would reflect off the boundary. Refracted modes correspond to rays which are totally refracted by the deep ocean waveguide. Figure A.1 summarizes the normal mode classifications.
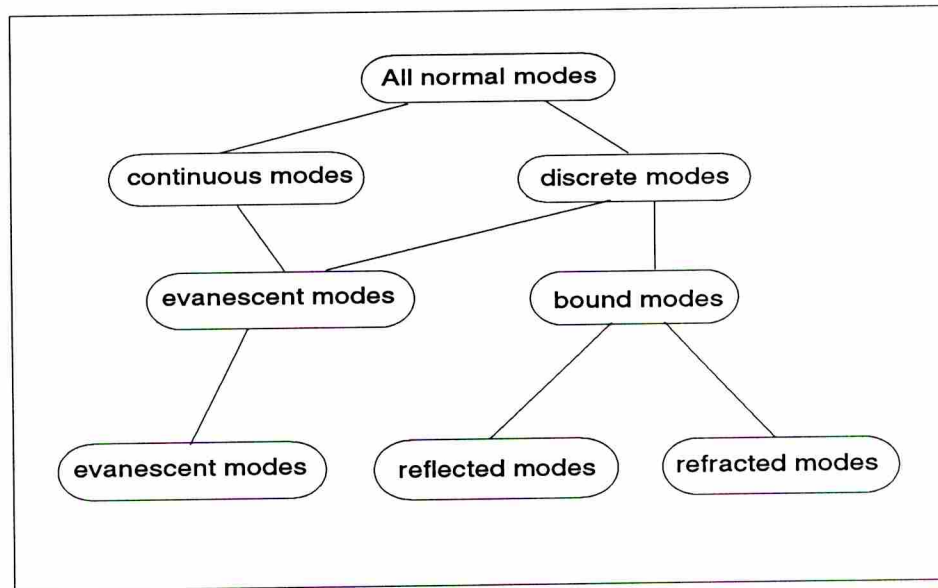
Figure A.1: Normal mode classification. Each layer of classes in the figure forms the complete grouping of modes (*e.g.* evanescent, reflected, and refracted modes represent all modes)

To implement a "ground truth" solution using Equation 3.1, some manageable number of normal modes must be used; thus, only a subset of the modes can be used. It is reasonable

---

[2]for any single acoustic frequency

to discard the evanescent modes based on their decay with range[3]. With only bound modes remaining, it is reasonable to discard the reflected modes citing boundary absorption and scattering[4]. This leaves the refracted modes. It is common to use the refracted modes in Equation 3.1 and declare this a ground truth solution. It is commonly believed that this solution is very accurate beyond a few acoustic wavelengths from the transmitter, since this is where the exponential approximation to the Hankel function is very accurate. However, one is ignoring a potentially larger assumption, the neglect of all evanescent and reflected modes.

The normal mode and ray tracing constructed waveform comparison in Section 3.5.1 (see Figures 3.9 - 3.13) gives some credibility to ignoring the evanescent modes. In this case, only 65 refracted mode were used, and comparisons between ray and mode computations were excellent, only with small error. One may conjecture the error in the comparison is due to the neglect of the evanescent modes. It has not been ruled out that there are significant errors in ray tracing that are not unveiled by a comparison with a bound normal mode solution because these errors are represented by evanescent normal modes, a part of the *actual* ground truth solution. This seems unlikely to the author, but should not go without stating.

The remainder of this appendix considers only bound modes in terms of rays and explores the classification of reflected and refracted modes.

A.2 Reflected & refracted modes and rays

Consider a range-invariant sound-speed profile $c_{S89}(z)$ defined in Chapter 2. In this case, the surface was modeled as pressure release interface, and the (rigid) bottom depth was 5110 m. The totally refracted rays were surface limited.

The group slowness curves for the first 200 modes (every fifth mode) were plotted in Figure A.2. The group slowness of mode m of acoustic frequency f is denoted $s_g(f|m)$ and is the reciprocal of the group velocity. The curves were coded to represent the modal slowness

---

[3]However, evanescent modes with wavenumbers having a small imaginary component will survive long ranges and may significantly contribute to the acoustic reception.

[4]Heard Island Feasibility Test and MIMI (Michigan Miami) experiments in the straits of Florida are examples of experiments where the acoustic energy *survived* long-distances of repeated surface reflections.
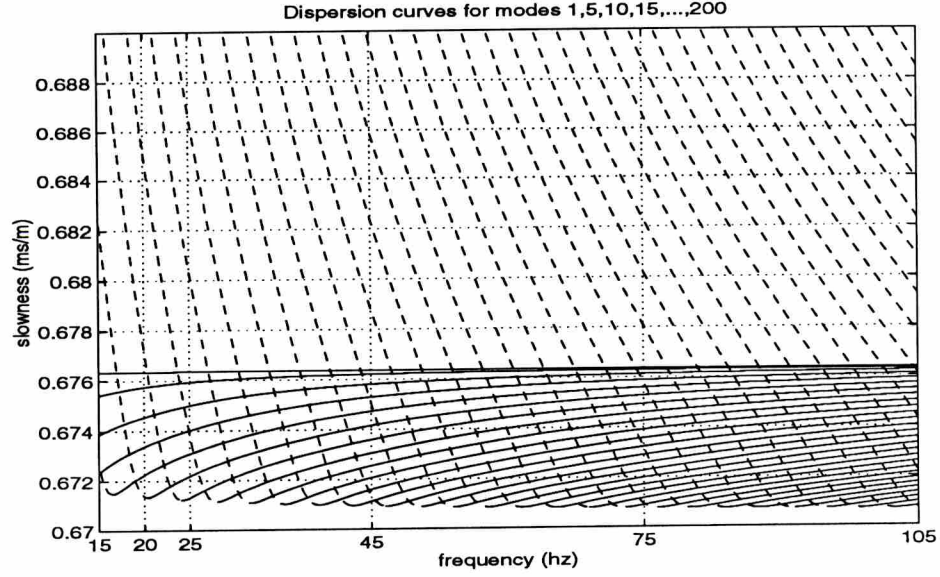
Figure A.2: Normal mode group slowness curves

above (solid) and below (dashed) *cutoff*. For this situation where the first derivative $(\frac{ds_g(f|m)}{df})$ is monotone increasing, "below cutoff" means a negative derivative, "cutoff" a zero derivative, "above cutoff" a positive derivative. **Nothing is "cut off"**. It simply is the boundary of a phenomenological regime. The modes above cutoff are referred to as refracted modes and the modes below cutoff are referred to as reflected modes. The description of Figure A.3 demonstrates the rationale for this mode-ray relation.

Figure A.3 (top) shows the envelope of a 75 hz Q=2.5 transmission at a range of 1 Mm calculated using all 200 normal modes. The absolute time on all plots was arbitrarily chosen. The source and receiver were on the sound channel axis. The surface reflected arrivals are well resolved and visible after the crescendo. The early arrivals are shown in Figure A.3 (middle), but they are not in the standard triplet sets of small-large-small expected for the axial source-receiver configuration. Figure A.3 (bottom) shows the envelope of the same reception except that the refracted modes are included to construct the solid-line envelope and the reflected modes construct the dashed-line envelope (in correspondence with Figure A.2). The reflected mode waveform corresponds to rays that have reflected off the ocean surface and have longer traveltimes than the earliest totally refracted arrival. The refracted mode arrivals correspond to the channeled totally refracted ray energy. The reflected arrivals overlap in time with the totally-refracted arrivals, interfering with the well

111
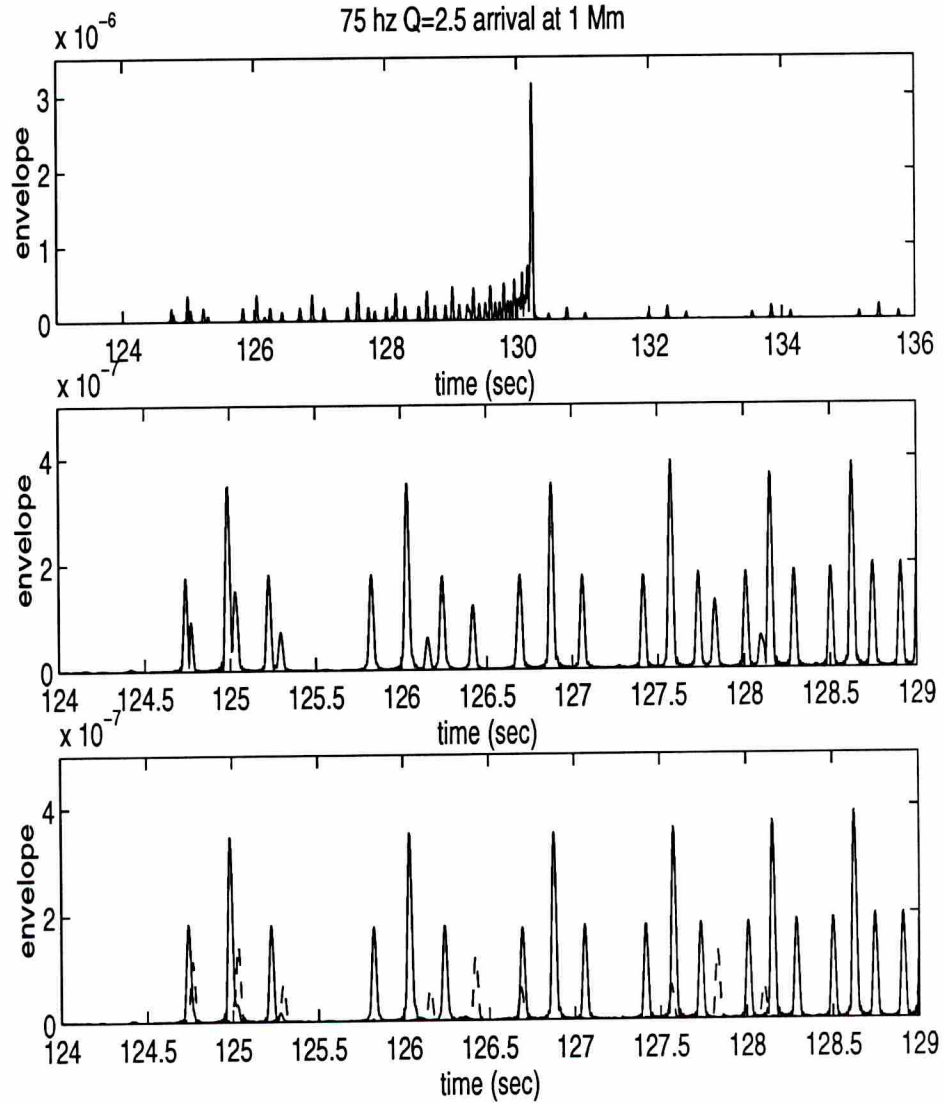
Figure A.3: Envelopes of acoustic reception including reflected and refracted rays (composed using normal modes). Top: complete arrival, Middle: early arrivals, Bottom: reflected modes/rays (dashed) and refracted modes/rays (solid).

resolved totally-refracted rays. Not shown, but true, is that the reflected arrivals interfere with the crescendo (axial arrivals) and persist after the crescendo as shown in Figure A.3 (top). Lower bandwidth sources have wider time-domain pulses and the interfering reflected wavefronts are more damaging to the refracted resolved arrival.

APPENDIX B

Ray tracing propagation method

The purpose of this appendix is derive the 3D ray tracing equations in the notation and form used in this dissertation, as well as detail the extension of the differential equation amplitude calculation method from 2D computations to 3D computations. The ray tracing equations are derived in Section D.1, following [51] and implementation of the equations follows the philosophy described in [53]. In Section D.2, the extension of the 2D differential equation amplitude calculation method to three dimensions is presented.

B.1   Derivation of ray tracing equations

The derivation of the ray tracing equations from the wave equation is presented starting with the homogeneous wave equation in three-dimensional rectangular coordinates.

$$\nabla^2 p = \frac{1}{c^2} \frac{\partial^2 p}{\partial t^2} \tag{B.1}$$

where $\nabla = \frac{d}{dx} + \frac{d}{dy} + \frac{d}{dz}$. The acoustic pressure, p, and sound speed field, c, are functions of space and time.

The acoustic pressure is assumed to be of the form

$$p = A e^{i\Omega(t-T)} \tag{B.2}$$

where A represents the amplitude across space and $\Omega(t - T)$ represents the phase. The acoustic amplitude A is solely a function of space. T is a scalar field, zero at the origin and increasing in all directions. T is solely a function of space. Contours of constant T represent the position of the waveform after a fixed traveltime. This is precisely the

concept of timefronts. This means we are implying a sufficiently broadband and high acoustic frequencies for ray tracing.

The form of the assumed solution (Equation B.2) states that the acoustic amplitude and phase are separable. Substituting the assumed solution into the left-hand side of Equation B.1 yields

$$\nabla^2 p = \nabla^2 A - 2i\Omega\nabla A\nabla T - \Omega^2\nabla T \cdot \nabla T A - iA\Omega^2\nabla^2 T \qquad (B.3)$$

Substituting the assumed solution into the right-hand side of Equation B.1 yields

$$\frac{1}{c^2}\frac{\partial^2 p}{\partial t^2} = -\frac{\Omega^2}{c^2}A \qquad (B.4)$$

In both Equations B.3 and B.4 the phase term, $e^{i\Omega(t-T)}$ has been suppressed. Combining the right and left hand sides of the above equations and considering only real terms yield

$$\nabla^2 A - \Omega^2\nabla T \cdot \nabla T A + \frac{\Omega^2}{c^2}A = 0 \qquad (B.5)$$

For "large" acoustic angular frequencies, only the last two terms of Equation B.5 will be significant. Recall, we have already assumed the existence of timefronts, so we have met this condition, but to obtain an interpretation of how large is "large" we compare the first and third term from Equation B.5, and ask under what conditions

$$|\nabla^2 A| \ll \frac{\Omega^2}{c^2}A \qquad (B.6)$$

Dividing both sides of Equation B.6 by the positive term $A\Omega^2$ and defining the acoustic wavelength, $\lambda \equiv 2\pi c/\Omega$, yields

$$|\frac{\nabla^2 A}{A}| \ll \frac{4\pi^2}{\lambda^2} \qquad (B.7)$$

Equation B.7 holds for cases when the rate of change of the acoustic amplitude does not change significantly with respect to an acoustic wave length. We continue under the assumption Equation B.7 holds; thus, Equation B.5 contains only two significant terms. This gives the relation called the eikonel equation.

$$\nabla T \cdot \nabla T = \frac{1}{c^2} \qquad (B.8)$$

Since rays travel perpendicular to the acoustic wavefront, ∇T is a vector in the direction of ray propagation. We see the rate of change along a ray is equal to the sound speed as

represented by

$$| \nabla T | = \pm \frac{1}{c} \tag{B.9}$$

where the "$\pm$" refers to rays traveling in each direction along the ray path. Equivalently we can state Equation B.9 in terms of the rate of change along the ray path

$$\frac{dr}{dT} = c \tag{B.10}$$

where r is the ray coordinate. Integrating Equation B.10 between arbitrary points along the ray yields

$$T = \int_{r_o}^{r_1} \frac{1}{c} dr \tag{B.11}$$

At this point, we will temporarily use the symbol s to represent the slowness field equal to the reciprocal of the sound speed field, c. Equation B.11 is rewritten in terms of the slowness field

$$T = \int_{r_o}^{r_1} s \ dr \tag{B.12}$$

Next, we take the gradient of each side of Equation B.12

$$\nabla T = \int_{r_o}^{r_1} \nabla s \ dr \tag{B.13}$$

Since, $\nabla T \equiv \frac{dT}{dr} \hat{r}$, we have

$$\frac{dT}{dr} \hat{r} = \int_{r_o}^{r_1} \nabla s \ dr \tag{B.14}$$

Differentiating along the ray path with respect to distance yields

$$\frac{d}{dr} [\frac{dT}{dr} \frac{dh}{dr}] = \nabla s \tag{B.15}$$

where h is a position vector from some reference point to the ray end point. Since, $\hat{r} \equiv \frac{dh}{dr}$

$$\frac{d}{dr} [s \frac{dh}{dr}] = \nabla s \tag{B.16}$$

Using the relations, $\frac{d}{dr} \equiv \frac{d}{dt} \frac{dt}{dr} \equiv s \frac{d}{dt}$ we can state

$$\frac{d}{dt} [s^2 \frac{dh}{dt}] = \frac{1}{s} \nabla s \tag{B.17}$$

Returning to use of the sound speed field, we have

$$\frac{d}{dt} (\frac{1}{c^2} \frac{dh}{dt}) = -\frac{1}{c} \nabla c \tag{B.18}$$

Rewriting Equation B.18 in its expanded form yields

$$\frac{d}{dt}[\frac{1}{c^2}(\hat{x}\frac{\partial x}{\partial t} + \hat{y}\frac{\partial y}{\partial t} + \hat{z}\frac{\partial z}{\partial t})] = -\frac{1}{c}[(\hat{x}\frac{\partial c}{\partial x} + \hat{y}\frac{\partial c}{\partial y} + \hat{z}\frac{\partial c}{\partial z})] \qquad (B.19)$$

Based on our use of an orthogonal coordinate system, the equations can be integrated separately. For example, consider the equation along the x coordinate.

$$\frac{d}{dt}[\frac{1}{c^2}\frac{dx}{dt}] = -\frac{1}{c}\frac{\partial c}{\partial x} \qquad (B.20)$$

We define the bracketed term by an auxiliary parameter

$$A = \frac{1}{c^2}\frac{dx}{dt} \qquad (B.21)$$

This leads to an update equation for the range ray coordinate for a small step in time.

$$\frac{dx}{dt} = c^2 A \qquad (B.22)$$

The auxiliary parameter is updated by

$$\frac{dA}{dt} = -\frac{1}{c}\frac{\partial c}{\partial x} \qquad (B.23)$$

Similarly we have the equations,

$$\frac{dz}{dt} = c^2 B \qquad (B.24)$$

$$\frac{dB}{dt} = -\frac{1}{c}\frac{\partial c}{\partial z} \qquad (B.25)$$

$$\frac{dy}{dt} = c^2 D \qquad (B.26)$$

$$\frac{dD}{dt} = -\frac{1}{c}\frac{\partial c}{\partial y} \qquad (B.27)$$

Where the initial conditions are the source location, (x_o, y_o, z_o), the transmission time t_o, and initial auxiliary parameters defined in Equations B.28 - B.30.

$$A_o = \frac{\cos \alpha_o \cos \psi_o}{c_s} \qquad (B.28)$$

$$B_o = \frac{\sin \alpha_o}{c_s} \qquad (B.29)$$

$$D_o = \frac{\cos \alpha_o \sin \psi_o}{c_s} \qquad (B.30)$$

117

The above suite of equations can be transformed into having range as an independent variable by the triangle relation

$$\frac{dx}{ds} = \cos\theta\cos\psi \qquad (B.31)$$

This leads to

$$\frac{dx}{dt} = c\cos\theta\cos\psi = Ac^2 \qquad (B.32)$$

which is a restatement of Equation B.22.

The standard ray tracing equations with an independent variable of range are defined in Equations B.33 - B.38.

$$\frac{dt}{dx} = \frac{1}{c^2 A} \qquad (B.33)$$

$$\frac{dz}{dx} = \frac{B}{A} \qquad (B.34)$$

$$\frac{dy}{dx} = \frac{D}{A} \qquad (B.35)$$

$$\frac{dA}{dx} = -\frac{1}{c}\frac{\partial c}{\partial x}\frac{dt}{dx} \qquad (B.36)$$

$$\frac{dB}{dx} = -\frac{1}{c}\frac{\partial c}{\partial z}\frac{dt}{dx} \qquad (B.37)$$

$$\frac{dD}{dx} = -\frac{1}{c}\frac{\partial c}{\partial y}\frac{dt}{dx} \qquad (B.38)$$

The ray tracing equations are numerically integrated using a fourth-order Runge-Kutta algorithm. For example, when using time as an independent variable, the equations are integrated to yield an update to the current ray position and amplitude.

For implementation, one ray is traced at a time. The step size of the independent variable was decreased until the final solutions converged. The computer code was written in FORTRAN as is included in Appendix C.

B.2 Derivation of differential equation amplitude calculation method

The derivation of the differential equation amplitude calculation method in two dimensions is contained in [54]. The wave equation is converted into a ray centered coordinate system (r, w) defined in Equations 3.16 and 3.17. After a significant amount of mathematical manipulation, the following relation is obtained

$$c\frac{\partial^2 q}{\partial r^2} - \frac{\partial c}{\partial r}\frac{\partial q}{\partial r} + \frac{\partial^2 c}{\partial w^2}q = 0 \qquad (B.39)$$

The acoustic amplitude along a ray is proportional to $1/\sqrt{q}$, and q is interpreted as the height of the ray tube. For implementation it is desirable to represent Equation B.39 as a system of two first-order linear differential equations.

$$\frac{\partial q}{\partial r} = cs \tag{B.40}$$

$$\frac{\partial s}{\partial r} = -\frac{1}{c^2}\frac{\partial^2 c}{\partial w^2}q \tag{B.41}$$

Converting these equations to have range as the independent variable yields,

$$\frac{dq}{dx} = \frac{s}{A} \tag{B.42}$$

$$\frac{ds}{dx} = \frac{-q}{Ac^3}\frac{\partial^2 c}{\partial w^2} \tag{B.43}$$

which are precisely the Equations 3.20 and 3.21. Here s is an auxiliary parameter and not the slowness field. For a Cartesian coordinate implementation we define the curvature along the wavefront as

$$\frac{\partial^2 c}{\partial w^2} = c^2\left(\frac{\partial^2 c}{\partial x^2}B^2 + 2\frac{\partial^2 c}{\partial x \partial z}AB + \frac{\partial^2 c}{\partial z^2}A^2\right) \tag{B.44}$$

It is the curvature of the sound speed field along the wavefront coordinate w that controls the update to the value of the q parameter.

For 3D computations, the orthogonal component (width) of the ray tube can be derived in a directly analogous manner to obtain

$$\frac{dv}{dx} = \frac{u}{A} \tag{B.45}$$

$$\frac{du}{dx} = \frac{-v}{Ac^3}\frac{\partial^2 c}{\partial y^2} \tag{B.46}$$

The acoustic amplitude is proportional to $1/\sqrt{qv}$, and u is an auxiliary parameter. We have assumed that the ray remains in the nominal acoustic plane, or equivalently $\psi = 0°$. The errors resulting from this assumption have been investigated and are insignificant for the results contained in this dissertation. Exact expressions are easily obtained, but their employment is at the expense of increased computation time.

The exact expressions to track the height and width of the ray tube in 3D are given. The derivation simply conducts a change in 3D coordinates between the Cartesian coordinates (x, y, z) and the *adjusted* Cartesian coordinates $(\bar{x}, \bar{y}, z)$. The adjusted coordinates

change with angle ψ along the ray path; so that, $x = \bar{x}\cos\psi$ and $y = \bar{y}\sin\psi$. The proper computations under this new coordinate system are

$$\frac{dq}{d\bar{x}} = \frac{s}{A} \tag{B.47}$$

$$\frac{ds}{d\bar{x}} = \frac{-q}{Ac}\left(\frac{\partial^2 c}{\partial \bar{x}^2}B^2 + 2\frac{\partial^2 c}{\partial \bar{x}\partial z}AB + \frac{\partial^2 c}{\partial z^2}A^2\right) \tag{B.48}$$

$$\frac{dv}{d\bar{x}} = \frac{u}{A} \tag{B.49}$$

$$\frac{du}{d\bar{x}} = \frac{-v}{Ac^3}\frac{\partial^2 c}{\partial \bar{y}^2} \tag{B.50}$$

For implementation, the second-order derivatives in $(\bar{x}, \bar{y}, z)$ must be expressed in terms of (x, y, z). Another change of coordinates is applied using the chain rule to obtain

$$\frac{\partial^2 c}{\partial \bar{x}} = \frac{\partial^2 c}{\partial x^2}\left(\frac{\partial x}{\partial \bar{x}}\right)^2 + 2\left(\frac{\partial x}{\partial \bar{x}}\right)\left(\frac{\partial y}{\partial \bar{x}}\right)\frac{\partial^2 c}{\partial x\partial y} + \frac{\partial^2 c}{\partial y^2}\left(\frac{\partial y}{\partial \bar{x}}\right)^2 \tag{B.51}$$

where $\frac{\partial y}{\partial \bar{x}} = \sin\psi$ and $\frac{\partial x}{\partial \bar{x}} = \cos\psi$.

$$\frac{\partial^2 c}{\partial \bar{y}} = \frac{\partial^2 c}{\partial y^2}\left(\frac{\partial y}{\partial \bar{y}}\right)^2 + 2\left(\frac{\partial y}{\partial \bar{y}}\right)\left(\frac{\partial x}{\partial \bar{y}}\right)\frac{\partial^2 c}{\partial y\partial x} + \frac{\partial^2 c}{\partial x^2}\left(\frac{\partial x}{\partial \bar{y}}\right)^2 \tag{B.52}$$

where $\frac{\partial x}{\partial \bar{y}} = \sin\psi$ and $\frac{\partial y}{\partial \bar{y}} = \cos\psi$.

APPENDIX C

Computer code

This appendix contains the computer code written to simulate and analyze acoustic propagation through deep-ocean internal waves. The appendix is divided into three sections to cover **ray, normal-mode, and PE** propagation methods. The computer code was written in either FORTRAN or MATLAB.

C.1 Ray code

This section contains the general 3D ray tracing code written in FORTRAN. Also, this section contains 2D range-invariant ray tracing code written in FORTRAN and output process written in MATLAB.

C.1.1 3D ray propagation code

```
DOUBLE PRECISION x(20),X0(10),E(10),D(10),RAD,TH1,DTH
DOUBLE PRECISION W(0:5000),C,delc,k,omg,kx,ky
NI = number of variables to integrate
NI = 6
T = time
T = 0
DX = range steps
DX = 50.0
pi=3.14159265358979
RAD = pi / 180
```

```
AMP = 0.2
```

omg = internal wave angular frequency

```
omg=2*pi*(1.31/3600.0)
```

k = internal wave wavenumber

```
k = 2.046213*2.0*pi/1000.0
```

ph = internal wave phase in radians

```
ph = -1.4762
```

theta = internal wave propagation direction wrt acoustic signal

```
theta = 88.9951*pi/180.0

kx = k*cos(theta)

ky = k*sin(theta)
```

Munk profile parameters

```
B = 520.

CO = 1480.0

EPS = .006

AX = 1200.0

x(11)=AX

x(12)=CO

x(13)=EPS
```

sd = source depth

```
sd=1200.
```

Bounds for launch angles and step size, 3D

```
th1a=-12.65

TH2a=-11.85

dtha=0.1

th1f=-0.01

TH2f=0.01

dthf=TH2f*2/4.
```

TT = range of propagation

```
TT=748050.0
```

```fortran
NTOT = NINT(TT / DX)

NRAYS = NINT((TH2a - th1a) / dtha)

NRAYF = NINT((TH2f - th1f) / dthf)

TH1 = th1a * RAD

DTH = dtha * RAD

THF = th1f * RAD

DTF = dthf * RAD

Open data containing internal wave mode

open (UNIT=18,FILE='iw14.dat',STATUS='old')

DO I=0,5000

READ(18,*)W(I)

ENDDO

close(16)

FE = (sd*1.0 - AX) / B

EF = EXP(-FE)

C=CO*(1+EPS*(EF+FE-1))

data1 = traveltime; data2 = depth; data3 = transverse

open (UNIT=11,FILE='data1.dat',STATUS='old')

open (UNIT=12,FILE='data2.dat',STATUS='old')

open (UNIT=13,FILE='data3.dat',STATUS='old')

10 format(f24.10)

Loop integration for each ray

do 90 nrr= 0, NRAYF

do 100 nr = 0, NRAYS

thet = TH1 + nr * DTH

phi = THF + nrr * DTF

c setup the initial conditions for a new ray x(2) = sd

x(1) = 0.0

x(5) = 0.0

delc = AMP*W(NINT(sd))*COS(ph)
```

```
CW = C*(1.0+delc)

x(3) = SIN(thet) / CW

x(4) = COS(thet)*COS(phi) / CW

x(6) = COS(thet)*SIN(phi) / CW

do 50 NST = 1 ,NTOT

call rungek(E,D,x,XO,NI,DX,T,W,AMP,B,omg,kx,ky,ph)

endif

50 continue

x(1) = traveltime; x(2) = depth; x(5) = transverse

write(11,10)x(1)

write(12,10)x(2)

write(13,10)x(5)

100 continue

90 continue

close(11)

close(12)

close(13)

end

C@@@@@@@@@@@@@@@@@@@@@@@@@@@@@@@@@@@@@@@@@@@@@@@@@@@@@@@@@@@@@@@@@@@@@@@@@@

Runge-Kutta integration routine

subroutine rungek(E,D,x,XO,NI,DX,T,W,AMP,B,omg,kx,ky,ph)

DOUBLE PRECISION D(10),x(20),XO(10),E(10)

DOUBLE PRECISION W(0:5000),kx,ky,omg

do 1000 I = 1, NI

XO(I) = x(I)

1000 continue

call sysspec(x,D,W,T,AMP,B,omg,kx,ky,ph)

do 2000 I = 1, NI

E(I) = D(I) * DX

x(I) = XO(I) + .5 * E(I)
```

```fortran
2000 continue

T = T + .5 * DX

call sysspec(x,D,W,T,AMP,B,omg,kx,ky,ph)

do 3000 I = 1, NI

E(I) = E(I) + 2 * D(I) * DX

x(I) = X0(I) + .5 * D(I) * DX

3000 continue

call sysspec(x,D,W,T,AMP,B,omg,kx,ky,ph)

do 4000 I = 1, NI

E(I) = E(I) + 2 * D(I) * DX

x(I) = X0(I) + D(I) * DX

4000 continue

T = T + .5 * DX

call sysspec(x,D,W,T,AMP,B,omg,kx,ky,ph)

do 5000 I = 1, NI

x(I) = X0(I) + (E(I) + D(I) * DX) / 6.0

5000 continue

RETURN

end

C@@@@@@@@@@@@@@@@@@@@@@@@@@@@@@@@@@@@@@@@@@@@@@@@@@@@@@@@@@@@@@@@@@@@

Routine to compute derivative information

subroutine sysspec(x,D,W,T,AMP,B,omg,kx,ky,ph)

DOUBLE PRECISION D(10),x(20),CC(5),C,W(0:5000),WW,AX,CO,EPS

DOUBLE PRECISION CW,C2,CI,INTW,kx,ky,omg

DOUBLE PRECISION DCZ,DCX,DCY

AX=x(11)

CO=x(12)

EPS=x(13)

itag=2

do ii=0,4
```

```fortran
xx=x(2)+1.0*(ii-itag)
WW=W(INT(xx))+(xx-INT(xx))*(W(INT(xx+1))-W(INT(xx)))
INTW=AMP*WW*COS(ky*x(5)+kx*T+omg*x(1)+ph)
FE=(xx-AX) / B
EF=EXP(-FE)
C=CO*(1+EPS*(EF+FE-1))
CC(ii+1)=C*(1.0 + INTW)
enddo
DCZ = (CC(1) - (8*CC(2)) + (8*CC(4)) - CC(5))/12.0
CW = CC(3)
WW=W(INT(x(2)))+(x(2)-INT(x(2)))*(W(INT(x(2)+1))-W(INT(x(2))))
do ii = 0,4
xx=T+(ii-2)
INTW = AMP*WW*COS(ky*x(5)+kx*xx+omg*x(1)+ph)
CC(ii+1) = CW*(1.0 + INTW)
enddo
DCX = (CC(1) - (8.*CC(2)) + (8.*CC(4)) - CC(5))/12.0
do ii=0,4
xx=x(2)+1.0*(ii-itag)
WW=W(INT(xx))+(xx-INT(xx))*(W(INT(xx+1))-W(INT(xx)))
INTW=AMP*WW*COS(ky*x(5)+kx*xxx+omg*x(1)+ph)
FE=(xx-AX) / B
EF=EXP(-FE)
C=CO*(1+EPS*(EF+FE-1))
CC(ii+1)=C*(1.0 + INTW)
enddo
do ii = 0,4
xx=x(5)+(ii-2)
INTW = AMP*WW*COS(kx*T+ky*xx+omg*x(1)+ph)
CC(ii+1) = CW*(1.0 + INTW)
```

```
enddo
DCY = (CC(1) - (8.*CC(2)) + (8.*CC(4)) - CC(5))/12.0
C2 = CW * CW
CI = 1 / CW
D(1) = 1.0/(x(4) * C2)
D(2) = x(3)/x(4)
D(3) = -CI * DCZ * D(1)
D(4) = -CI*DCX * D(1)
D(5) = x(6)*C2*D(1)
D(6) = -CI*DCY*D(1)
RETURN
end
```

C.1.2   2D range invariant propagation code

This FORTRAN code is essentially a subset of the full 3D code. All variables use the same convention as with the previous FORTRAN program which was excessively commented. It computes the amplitude using the differential equation method. A MATLAB post-processor code follows to construct the envelope and phase of the acoustic reception.

```
DOUBLE PRECISION x(10),XO(10),E(10),D(10),DTH,TH1,thet,C,EF,FE
REAL ocean
NI = 5
T = 0
DX = 30.
C Munk profile parameters B = 520.
EPS = 0.006
AX= 1200.0
CO = 1480.0
C sd = source depth sd=1200.
```

```
th1a=-15.
TH2a= 15.
dtha=0.10
C TT = propagation range TT = 185000.0
NTOT = NINT(TT / DX)
NRAYS = NINT((TH2a - th1a) / dtha)
RAD = 1.  / 57.29577951
TH1 = th1a * RAD
DTH = dtha * RAD
do 100 nr = 0, NRAYS
thet = TH1 + nr * DTH
x(2) = sd
x(1) = 0
FE = (x(2) - AX) / B
EF = EXP(-FE)
C=C0*(1+EPS*(EF+FE-1))
C x(3) is tangent of ray inclination angle
x(3) = TAN(thet)
C x(4) is the q paramenter in dynamic ray tracing / Gaussian Beams
x(4) = 0
c x(5) is the p parameter in dynamic ray tracing / Gaussian Beams
x(5) = 1 / C
c x(6) is the Snell's Law constant
x(6) = COS(thet) / C
C data1.dat stores the time co-ordinate for each ray after TT meters
C of propagation
C data2.dat stores the depth co-ordinate ....
C data3.dat stores the number of caustics crossed
C data4.dat stores the amplitude .....
open (UNIT=1,FILE='data1.dat',STATUS='old')
```

```fortran
open (UNIT=2,FILE='data2.dat',STATUS='old')
open (UNIT=3,FILE='data3.dat',STATUS='old')
open (UNIT=4,FILE='data4.dat',STATUS='old')
ocean=0.0
toc=0.0
do 50 NST = 1 ,NTOT
xold=x(3)
call rungek(E,D,x,DX,X0,NI,C0,B,CEB,AX,EPS)
if(toc.gt.0)then
if(x(3)*xold.le.0.0)then
ocean=ocean+1
toc=-5.0
endif
endif
toc=toc+1
xold=x(3)
50 continue
c plotting for time fronts
write(1,10)x(1)
write(2,10)-x(2)
write(3,10)x(4)
write(4,10)ocean
10 format(f16.8)
100 continue
close(1)
close(2)
close(3)
close(4)
end
C Runge-Kutta integration routine subroutine rungek(E,D,x,DX,X0,NI,C0,B,CEB,AX,EPS)
```

```fortran
      DOUBLE PRECISION D(10),x(10),XO(10),E(10)
      do 1000 I = 1, NI
      XO(I) = x(I)
1000  continue
      call sysspec(x,D,AX,B,EPS,CEB,CO)
      do 2000 I = 1, NI
      E(I) = D(I) * DX
      x(I) = XO(I) + .5 * E(I)
2000  continue
      call sysspec(x,D,AX,B,EPS,CEB,CO)
      do 3000 I = 1, NI
      E(I) = E(I) + 2 * D(I) * DX
      x(I) = XO(I) + .5 * D(I) * DX
3000  continue
      call sysspec(x,D,AX,B,EPS,CEB,CO)
      do 4000 I = 1, NI
      E(I) = E(I) + 2 * D(I) * DX
      x(I) = XO(I) + D(I) * DX
4000  continue
      call sysspec(x,D,AX,B,EPS,CEB,CO)
      do 5000 I = 1, NI
      x(I) = XO(I) + (E(I) + D(I) * DX) / 6.0
5000  continue
      RETURN
      end
C Computation of derivatives subroutine sysspec(x,D,AX,B,EPS,CEB,CO)
      DOUBLE PRECISION D(10),x(10),FE,EF,CI,C2,C,DCY
c Profile parameters
      FE = (x(2) - AX) / B
      EF = EXP(-FE)
```

```
CEB = CO * EPS / B

C=CO*(1+EPS*(EF+FE-1))

DCY = CEB*(1-EF)

DCYY = (CEB*EF/B)

C2 = C * C

CI = 1 / C

D(1) = 1./(x(6) * C2)

D(2) = x(3)

D(3) = -CI * DCY * D(1)/x(6)

D(4) = x(5) / x(6)

D(5) = -DCYY * x(4) * x(6)/C

RETURN end
```

C.1.3   Output processor code

This is the MATLAB code which forms the time-domain envelope and phase of the reception from the ray tracing data generated using the previous FORTRAN code.

```
clear all
x=data1;
z=-data2;
R=3000000.;
data3=data3+10.0*log10(R);
amplitude=10.^(-data3/20);
ocean=data4;
N=4096;
f=([0:N-1]-N/2)*240/4096;
arg=f/15.0;
S=sinc(arg);
bandlimit=(sign(15-abs(f))+1)/2;
S=S.*bandlimit;
j=sqrt(-1);
depth = 800.0
flip=-1.0;
if x(1) < depth
flip=1.0;
end
for i=1:length(x)-1
if flip*(z(i) - depth) > 0.0
if flip*(z(i+1) - depth) < 0.0
flip=-1.0*flip;
c=c+1;
tw(c)=x(i) + ((depth - z(i))/(z(i+1)-z(i)))*(x(i+1)-x(i));
ophase(c)=ocean(i);
```

```
amp(c)=amplitude(i)+ ((depth - z(i))/(z(i+1)-z(i)))* ...

(amplitude(i+1)-amplitude(i));

end

end

end

sig=zeros(size([1:N]));

t=([0:N-1]/240.0);

Sexp=0;

for i=1:length(tw)

Sexp=Sexp + amp(i)*S.*exp(-j*2*pi*(75+f)*tw(i))*exp(j*pi*ophase(i)/2);

end

sig=(ifft(fftshift(Sexp)));

plot(t,abs(sig))
```

C.2 Normal mode code

This is MATLAB code used to construct normal mode acoustic arrivals from the Scripps modemaker code.

```
R=3000000.0;
N=4096;
numdeep=512;
delf=freq(2)-freq(1);
f=([0:N-1]-N/2)*240/N;
arg=(f/15);
S=sinc(arg);
bandlimit=(sign(15-abs(f))+1)/2;
S=S.*bandlimit;
f=f+75.0;
isource=81;
irec=81;
P=zeros(size(S));
c=0;
for i=1:length(S)
if bandlimit(i) > .1
```

o, oo

```
=min(abs(freq-f(i)));
a=f(i)-freq(oo);
if a < 0
b=f(i)-freq(oo-1);
uu=oo-1;
else
b=freq(oo+1)-f(i);
uu=oo+1;
```

```
end
UU1=reshape(U(oo,:),maxmode,numdeep);
UU2=reshape(U(uu,:),maxmode,numdeep);
UU=UU2 + (UU1-UU2)*(b/delf);
USource=UU(:,isource);
Kn1=K(oo,:)';
Kn2=K(uu,:)';
Kn=Kn2 + (Kn1-Kn2)*(b/delf);
Urec=UU(:,irec);
temp1=USource.*(ones(size(Kn))./sqrt(Kn)).*exp(-j*Kn*R);
temp2=((2*pi)^(0.5))*exp(j*pi/4)/sqrt(R);
temp=temp2*temp1;
P(i)=S(i)*sum(temp.*Urec);
end
end
p=fftshift(ifft(fftshift(P),length(P)));
t=[0:length(f)-1]/240.0;
plot(t,fftshift(abs(p)),'g--')
```

C.3 PE code

This program uses PE to simulate acoustic propagation. The program is written in FORTRAN. The standard split step FFT (sin transform) is used with a Gaussian starting field. This program is for single frequency / range invariant but can easily be adjusted to include range variant perturbations and broadband sources, as well as coded for use an the IBM SP2. The algorithm is based on 4 references: 1) Computational Acoustics[16] (Chapter 6); 2) Numerical Recipes[22] (Chapter 12); 3) The technical paper[29]; 4) Email conversations with Paul Book[50].

```
integer Nz,f
```

```fortran
COMPLEX Kfac(1024), SSPfac(1024), Phi(1024), i, P
real range,depth,k0,Zb,Zs,dist,delr,freq,c0,c(1024),iwph
real eps,ax,B,eta,ssp,temp,atten(1024),delf,flow,iwk,iwomg
real W(0:5000) dist = 748050.0
c source depth
Zs = 1200.0
delr = 50.0
Zb=5115.0
Nz=1024
deld = Zb/(Nz-1.0)
c0 = 1480.0
eps = 0.006
ax = 1200.0
B = 1040.0
i = cmplx(0,1)
pi = 3.141592653589793d0
c internal wave set up
AMP = 0.23
RAD=pi/180.0
iwomg=2*pi*(1.31/3600.0)*0.0
iwk = 2.046213*2.0*pi/1000.0
iwph = 0.42014522198833-pi
theta = 86.02607907245563*pi/180.0
iwk = iwk*cos(theta)
open (UNIT=4,FILE='iw14.dat',STATUS='old')
DO Iiw=0,5000
READ(4,*)W(Iiw)
ENDDO
close(4)
open (UNIT=1,FILE='peout.dat',STATUS='old')
```

```fortran
Nf = 513

delf=0.05859375000000

flow=60.0

fc=75.0

do f=1,Nf

open (UNIT=3,FILE='pestat.dat',STATUS='old')

write(3,*)f,Nf

c write(6,*)f,Nf

close(3)

freq=(f-1.0)*delf+flow

if(freq.eq.fc) then

S =1.0

else

S = sin(pi*(freq-fc)/15.0)/(pi*(freq-fc)/15.0)

c write(6,*)S

endif

k0 = 2*pi*freq/c0

do k = 1,Nz

depth = (k-1)*deld

eta = 2*(ax - depth)/B

c(k) = c0*(1.0 + eps*(exp(eta) - eta -1 ))

ssp=ssp + AMP*W((k-1)*5+1)*COS(iwph)

temp=exp(-((depth-Zb)/(0.04*Zb))**2.0)

atten(k)=exp(-0.05*delr*temp)

Kfac(k) = exp((-i*delr/(2*k0))*((pi/Zb)*(k-1.0))**2.0)

SSPfac(k) = atten(k)*exp((i*k0/2)*((c0/ssp)**2.0 - 1)*delr)

Phi(k) = (k0**0.5)*exp(-((k0**2.0))*((depth-Zs)**2.0) /2.0)

enddo

do m = 1,NINT(dist/delr)

range = m*delr
```

```fortran
do k = 1,Nz
ssp=c(k) + AMP*W((k-1)*5+1)*COS((iwk-iwomg/c0)*range+iwph)
SSPfac(k)=atten(k)*exp((i*k0/2)*((c0/ssp)**2.0 - 1)*delr)
Phi(k) = (2./Nz)*Phi(k)*SSPfac(k)
enddo
call work(Phi,Nz,Kfac)
enddo
do k = 1,Nz
P=S*Phi(k)*exp(i*k0*range - pi/4)*sqrt(2*pi/range)
write(1,10) real(P),imag(P)
enddo
enddo
10 format(f24.20,XXX,f24.20)
close(1)
end
SUBROUTINE work(y,n,fac)
INTEGER n
REAL temp1(n),temp2(n),temp
COMPLEX y(n),i,fac(n)
i = cmplx(0,1)
do k = 1,n
temp1(k) = real(y(k))
temp2(k) = imag(y(k))
enddo
call sinft(temp1,n)
call sinft(temp2,n)
do k = 1,n
temp = temp1(k)
temp1(k) = real(fac(k)*(temp1(k) + i*temp2(k)))
temp2(k) = imag(fac(k)*(temp + i*temp2(k)))
```

```fortran
      enddo

      call sinft(temp1,n)

      call sinft(temp2,n)

      do k = 1,n

      y(k) = temp1(k) + i*temp2(k)

      enddo

      return

      end
```

BIBLIOGRAPHY

BIBLIOGRAPHY

[1] W. Munk, "The Sound of Oceans Warming," The Sciences, Sept/Oct 1993 21-26

[2] T.G. Birdsall K. Metzger "M-Sequence Signal Tutorial" Communications and Signal Processing Laboratory, EECS Department, University of Michigan, April 1988.

[3] S. Wang, M.L. Grabb, T.G. Birdsall, "Design of Periodic Signals Using FM Sweeps and Amplitude Modulation for Ocean Acoustic Traveltime Measurements," *IEEE J. of Oceanic Eng.* Vol 19, No 4., October 1994.

[4] T.G. Birdsall and K. Metzger, personal communication

[5] S. M. Flatté, Editor *Sound Propagation through a fluctuating ocean*, Cambridge University Press, 1979.

[6] C. Garrett W.H. Munk, "Space-Time scales of internal waves: A progress report", J. Geophysical Research, page 291 Jan 20 1975

[7] S.M. Flatté, "Wave propagation through random media: Contributions from ocean acoustics" Proc IEEE 71, 1267-1294 (1983)

[8] T.F. Duda *et al* "Measured wave-front fluctuations in 1000-km pulse propagation in the Pacific Ocean", *Journal of the Acoustical Society of America* p939-955, 1992

[9] S.M. Flatté, S.A. Reynolds, R. Dashen, "Path-integral treatment of intensity behavior for rays in a sound channel", *Journal of the Acoustic Society of America*, page 967-972, 82, 1987

[10] S.M. Flatté R.B. Stoughton "Predictions of internal-wave effects on ocean acoustic coherence, travel-time variance, and intensity moments for very long-range propagation", *Journal of the Acoustic Society of America*, page 1414-1424, 84, 1988

[11] S. M. Flatté, "Random-Media Effects in Ocean Acoustics: An Introduction", Invited talk at the International Meeting for Wave Propagation in Random Media, Seattle, WA, August 3-7, 1992

[12] J.A. Colosi, S.M. Flatté, C. Bracher "Internal-wave effects on 1000-km oceanic acoustic pulse propagation: Simulation and comparison with experiment", *Journal of the Acoustical Society of America*, vol 96, pp 452-468, 1994

[13] H. A. DeFarrari, "Effects of horizontally varying internal wavefields on multipath interference for propagation through the deep ocean", *Journal of the Acoustical Society of America*, vol 56, pp 40-46

[14] P. Techau unpublished report

[15] G.E.J. Bold, T.G. Birdsall, K. M. Metzger "Long-range arrival structure using time-front analysis", *112th Acoustical Society of America meeting*, section FF, page S.63, Fall 1986

[16] F.B. Jensen *et al*, *Computational Acoustics*, AIP Press (1994)

[17] H.P. Bucker "Use of calculated sound fields and matched field detection to locate sound sources in shallow water," J. Acoust. Soc. Am. 66, 480-483, 1979.

[18] J. Preisig, "A minmax approach to adaptive matched field processing in an uncertain propagation environment," *IEEE Transactions on Signal Processing* 42:1305-16 Jun '94

[19] J.L. Krolik, "Matched-field minimum variance beamforming in a random ocean channel," *Journal of the Acoustical Society of America* v92, p1408-1419, 1992

[20] W. H. Munk, "Sound channel in an exponentially stratified ocean, with application to SOFAR ", *Journal of the Acoustical Society of America* vol 55 pp 220-226

[21] O.M. Phillips, *Dynamics of the Upper Ocean*, Cambridge Press, 1977

[22] Press et al "Numerical Recipes in FORTRAN," Cambridge University Press 1992.

[23] Ortega, James M., "An introduction to numerical methods for differential equations," Boston : Pitman Pub., c1981.

[24] A.R. Robinson, D. Lee (Editors), "Oceanography and Acoustics, prediction and propagation models" AIP Series in Modern Acoustics and Signal Processing, AIP Press 1994.

[25] Hobaek, H., Muir, T G., Tindle, C T., "Downslope propagation of normal modes in a shallow water wedge.", *Journal of the Acoustical Society of America*, **81**, Feb 1987, pp 275-286.

[26] S. Shang, personal communication, 130th meeting of the Acoustical Society of America, St Louis, Mo.

[27] M.D. Collins, S.A. Chin-Bing, "A three-dimensional parabolic equation model that includes the effects of rough boundaries", *Journal of the Acoustical Society of America*, **87**, 3, Mar 1990, pp 1104-1109.

[28] D. Peregrym, "An Investigation of Shallow Water Mode Coupling Effects During Single Mode Transmissions," Woods Hole Oceanographic Society, Masters Thesis, 1994

[29] R.H. Hardin and F.D. Tappert, "Applications of the split-step Fourier method to the numerical solution of nonlinear and variable coefficient wave equations," SIAM Rev. 15, 423 (1973).

[30] F.D. Tappert personal communication

[31] Michael B. Porter and Homer Bucker, "Gaussian Beam Tracing for Computing Ocean Acoustic Fields", *Journal of the Acoustical Society of America*, **82**, 4, October 1987, pp 1349-1359.

[32] M.G. Brown, "A Maslov-Chapman wavefield representation for wide-angle one-way propagation" *Geophys. J. Int.* (1994) **116**, 513-526

[33] D. W. White and M.A. Pedersen, "Evaluation of shadow-zone fields by uniform asymptotics and complex rays" *J. Acoustical Soc. of America* **69** 1029-1059 (1981)

[34] I Tolstoy "Phase changes and pulse Deformation in Acoustics", *Journal of the Acoustical Society of America* p675-683, 1968

[35] J.F. Lynch, A.E. Newhall, C.S. Chiu, and J.H. Miller, *Oceanography and Acoustics Prediction and Propagation Models*, Edited by A.R. Robinson and D. Lee, AIP Press, 1994.

[36] A. Draganov and J. Spiesberger "Diffraction and pulse delay in a structured ocean", preprint June 1994, *submitted to J. Acoustical Soc. of America*

[37] C.T. Tindle *et al*, "Measurements of the frequency dependence of normal modes" *J. Acoustical Soc. of America* **64** 1178-1185 (1978)

[38] C.T. Tindle, P.A. Casey, G.E.J. Bold, S.M. Tan, "Normal Mode Extraction for ATOC Signals" *ATOC Occasional Notes*, No 26

[39] M.D. Collins and W.A. Kuperman. "Focalization: environmental focusing and source localization." *J. Acoustical Soc. of America* **90** 1410-22 (1991)

[40] Voltz, P. and Lu, I-Tai, "A time-domain backpropagating ray technique for source localization." *J. Acoustical Soc. of America* **95** 805-12 (1994)

[41] A. Tolstoy, "Matched Field Processing for Underwater Acoustics," World Scientific, 1993.

[42] T.G. Birdsall, K Metzger, M.A. Dzieciuch, " Signals, signal processing, and general results", *Journal of the Acoustical Society of America* 96 (4), p2343-2352, 1994

[43] F.D. Tappert and X. Tang, "Ray chaos and eigenrays" submitted to *Journal of the Acoustical Society of America*

[44] T.G. Birdsall, K Metzger, M.A. Dzieciuch, J. Spiesberger, "Integrated autocorrelation phase at one period lag", *Journal of the Acoustical Society of America* 96 (4), p2353-2356, 1994

[45] "Handbook of Mathematical Functions with Formulas, Graphs, and Mathematical Tables," U.S. Dept. of Commerce, Edited by M Abramowitz and I.A. Stegun, Nov 1970.

[46] J.G. Proakis, "Digital Communications" 1989 McGraw Hill.

[47] J.W. Goodman "Statistical Optics" 1985 John Wiley and Sons.

[48] M..A. Dzieciuch unpublished computer algorithm to solve normal mode functions using matrix methods.

[49] P. Casey personal communication

[50] P. Book personal communication

[51] G.E.J. Bold "Ray tracing demonstration program RAYA.BAS", Class Notes, Physics Department, University of Auckland, New Zealand.

[52] B.D. Cornuelle and B.M. Howe, "High spatial resolution in vertical slice ocean acoustic tomography" *J. Geophys.Res., 92* 11680-92

[53] G.E.J. Bold and T.G. Birdsall, "A top-down philosophy for accurate numerical ray tracing", *Journal of the Acoustical Society of America* p656-660, 1986

[54] M.M. Popov and Ivan Pšenčík, "Computation of Ray Amplitudes in Inhomogeneous Media with Curved Interfaces", *Studia Geoph. et Geod.* **22**, 1978, pp 248-258